

ISSN 1816-112X

Science Citation Index Expanded,
Materials Science Citation Index
and ISI Alerting

EDITORS-IN-CHIEF

Asian Pacific, African and organizing Editor

S.L. Chan
*The Hong Kong Polyt. Univ.,
Hong Kong*

American Editor

W.F. Chen
Univ. of Hawaii at Manoa, USA

European Editor

R. Zandonini
Trento Univ., Italy

INTERNATIONAL EDITORIAL BOARD

F.G. Albermani
Central Queensland Univ., Australia

I. Burgess
Univ. of Sheffield, UK

F.S.K. Bijlaard
Delft Univ. of Technology, The Netherlands

R. Bjorhovde
The Bjorhovde Group, USA

M.A. Bradford
The Univ. of New South Wales, Australia

D. Camotim
Technical Univ. of Lisbon, Portugal

C.M. Chan
Hong Kong Univ. of Science & Technology, Hong Kong

T.H.T. Chan
Queensland Univ. of Technology, Australia

T.M. Chan
The Hong Kong Polyt. Univ., Hong Kong

S.P. Chiew
Singapore Institute of Technology, Singapore

W.K. Chow
The Hong Kong Polyt. Univ., Hong Kong

G.G. Deierlein
Stanford Univ., California, USA

L. Dezi
Univ. of Ancona, Italy

D. Dubina
The Politehnica Univ. of Timisoara, Romania

L. Gardner
Imperial College of Science, Technology and Medicine, UK

R. Greiner
Technical Univ. of Graz, Austria

Y. Goto
Nagoya Institute of Technology

L.H. Han
Tsinghua Univ. China

S. Herion
University of Karlsruhe, Germany

G.W.M. Ho
Ove Arup & Partners Hong Kong Ltd., Hong Kong

B.A. Izzuddin
*Imperial College of Science, Technology and
Medicine, UK*

J.P. Jaspart
Univ. of Liege, Belgium

S. A. Jayachandran
IIT Madras, Chennai, India

S.E. Kim
Sejong Univ., South Korea

S. Kitipornchai
The Univ., of Queensland, Australia

D. Lam
Univ. of Bradford, UK

G.Q. Li
Tongji Univ., China

J.Y.R. Liew
National Univ. of Singapore, Singapore

Y.P. Liu
The Hong Kong Polyt. Univ., Hong Kong

S.W. Liu
NIDA EUROPE Ltd., UK

E.M. Lui
Syracuse Univ., USA

Y.L. Mo
Univ. of Houston, USA

J.P. Muzeau
CUST, Clermont Ferrand, France

D.A. Nethercot
*Imperial College of Science, Technology and
Medicine, UK*

Y.Q. Ni
The Hong Kong Polyt. Univ., Hong Kong

D.J. Oehlers
The Univ. of Adelaide, Australia

J.L. Peng
Yunlin Uni. of Science & Technology, Taiwan

K. Rasmussen
The Univ. of Sydney, Australia

J.M. Rotter
The Univ. of Edinburgh, UK

C. Scawthorn
Scawthorn Porter Associates, USA

P. Schaumann
Univ. of Hannover, Germany

Y.J. Shi
Tsinghua Univ., China

G.P. Shu
Southeast Univ. China

L. Simões da Silva
*Department of Civil Engineering, University of
Coimbra, Portugal*

J.G. Teng
The Hong Kong Polyt. Univ., Hong Kong

G.S. Tong
Zhejiang Univ., China

K.C. Tsai
National Taiwan Univ., Taiwan

C.M. Uang
Univ. of California, USA

B. Uy
The University of New South Wales, Australia

M. Veljkovic
Univ. of Lulea, Sweden

F. Wald
Czech Technical Univ. in Prague, Czech

Y.C. Wang
The Univ. of Manchester, UK

Y.L. Xu
The Hong Kong Polyt. Univ., Hong Kong

D. White
Georgia Institute of Technology, USA

E. Yamaguchi
Kyushu Institute of Technology, Japan

Y.B. Yang
National Taiwan Univ., Taiwan

Y.Y. Yang
China Academy of Building Research, Beijing, China

B. Young
The Univ. of Hong Kong, Hong Kong

X.L. Zhao
Monash Univ., Australia

X.H. Zhou
Chongqing University, China

Z.H. Zhou
Alpha Consultant Ltd., Hong Kong

R.D. Ziemian
Bucknell University, USA

Cover: The 139mx73m clear span Spectacle Roof designed by Second-order Direct Analysis without assumption of effective length

e-copy of IJASC is free to download at "www.ascjournal.com" in internet and mobile apps.

General Information

Advanced Steel Construction, an international journal

Aims and scope

The International Journal of Advanced Steel Construction provides a platform for the publication and rapid dissemination of original and up-to-date research and technological developments in steel construction, design and analysis. Scope of research papers published in this journal includes but is not limited to theoretical and experimental research on elements, assemblages, systems, material, design philosophy and codification, standards, fabrication, projects of innovative nature and computer techniques. The journal is specifically tailored to channel the exchange of technological know-how between researchers and practitioners. Contributions from all aspects related to the recent developments of advanced steel construction are welcome.

Instructions to authors

Submission of the manuscript.

Authors may submit on-line at www.hkisc.org
Asian Pacific, African and organizing editor : Professor S.L. Chan, Email: ceslchan@polyu.edu.hk
American editor : Professor W.F. Chen, Email: waifah@hawaii.edu
European editor : Professor R. Zandonini, Email: riccardo_zandonini@ing.unitn.it

All manuscripts submitted to the journal are recommended to accompany with a list of four potential reviewers suggested by the author(s). This list should include the complete name, address, telephone and fax numbers, email address, and at least five keywords that identify the expertise of each reviewer. This scheme will improve the process of review.

Style of manuscript

General. Author(s) should provide full postal and email addresses and fax number for correspondence. The manuscript including abstract, keywords, references, figures and tables should be in English with pages numbered and typed with double line spacing on single side of A4 or letter-sized paper. The front page of the article should contain:

- a) a short title (reflecting the content of the paper);
- b) all the name(s) and postal and email addresses of author(s) specifying the author to whom correspondence and proofs should be sent;
- c) an abstract of 100-200 words; and
- d) 5 to 8 keywords.

The paper must contain an introduction and a conclusion. The length of paper should not exceed 25 journal pages (approximately 15,000 words equivalents).

Tables and figures. Tables and figures including photographs should be typed, numbered consecutively in Arabic numerals and with short titles. They should be referred in the text as Figure 1, Table 2, etc. Originally drawn figures and photographs should be provided in a form suitable for photographic reproduction and reduction in the journal.

Mathematical expressions and units. The Systeme Internationale (SI) should be followed whenever possible. The numbers identifying the displayed mathematical expression should be referred to in the text as Eq. 1, Eq. 2.

References. References to published literature should be referred in the text, in the order of citation with Arabic numerals, by the last name(s) of the author(s) (e.g. Zandonini and Zanon [3]) or if more than three authors (e.g. Zandonini et al. [4]). References should be in English with occasional allowance of 1-2 exceptional references in local languages and reflect the current state-of-technology. Journal titles should be abbreviated in the style of the Word List of Scientific Periodicals. References should be cited in the following style [1, 2, 3].

Journal: [1] Chen, W.F. and Kishi, N., "Semi-rigid Steel Beam-to-column Connections, Data Base and Modelling", Journal of Structural Engineering, ASCE, 1989, Vol. 115, No. 1, pp. 105-119.

Book: [2] Chan, S.L. and Chui, P.P.T., "Non-linear Static and Cyclic Analysis of Semi-rigid Steel Frames", Elsevier Science, 2000.

Proceedings: [3] Zandonini, R. and Zanon, P., "Experimental Analysis of Steel Beams with Semi-rigid Joints", Proceedings of International Conference on Advances in Steel Structures, Hong Kong, 1996, Vol. 1, pp. 356-364.

Proofs. Proof will be sent to the corresponding author to correct any typesetting errors. Alternations to the original manuscript at this stage will not be accepted. Proofs should be returned within 48 hours of receipt on-line.

Copyright. Submission of an article to "Advanced Steel Construction" implies that it presents the original and unpublished work, and not under consideration for publication nor published elsewhere. On acceptance of a manuscript submitted, the copyright thereof is transferred to the publisher by the Transfer of Copyright Agreement and upon the acceptance of publication for the papers, the corresponding author must sign the form for Transfer of Copyright.

Permission. Quoting from this journal is granted provided that the customary acknowledgement is given to the source.

Page charge and Reprints. There will be no page charges if the length of paper is within the limit of 25 journal pages. A total of 30 free offprints will be supplied free of charge to the corresponding author. Purchasing orders for additional offprints can be made on order forms which will be sent to the authors. These instructions can be obtained at the Hong Kong Institute of Steel Construction, Journal website: <http://www.hkisc.org>

The International Journal of Advanced Steel Construction is published quarterly by learnt society, The Hong Kong Institute of Steel Construction, c/o Department of Civil & Environmental Engineering, The Hong Kong Polytechnic University, Hung Hom, Kowloon, Hong Kong.

Disclaimer. No responsibility is assumed for any injury and / or damage to persons or property as a matter of products liability, negligence or otherwise, or from any use or operation of any methods, products, instructions or ideas contained in the material herein.

Subscription inquiries and change of address. Address all subscription inquiries and correspondence to Member Records, IJASC. Notify an address change as soon as possible. All communications should include both old and new addresses with zip codes and be accompanied by a mailing label from a recent issue. Allow six weeks for all changes to become effective.

The Hong Kong Institute of Steel Construction

HKISC

c/o Department of Civil and Environmental Engineering,

The Hong Kong Polytechnic University,

Hunghom, Kowloon, Hong Kong, China.

Tel: 852- 2766 6047 Fax: 852- 2334 6389

Email: ceslchan@polyu.edu.hk Website: <http://www.hkisc.org/>

ISSN 1816-112X

Science Citation Index Expanded, Materials Science Citation Index and ISI Alerting

Copyright © 2017 by:

The Hong Kong Institute of Steel Construction.



ISSN 1816-112X

Science Citation Index Expanded,
Materials Science Citation Index and
ISI Alerting

EDITORS-IN-CHIEF

Asian Pacific, African and organizing Editor

S.L. Chan

*The Hong Kong Polyt. Univ.,
Hong Kong*

Email: ceslchan@polyu.edu.hk

American Editor

W.F. Chen

Univ. of Hawaii at Manoa, USA

Email: waifah@hawaii.edu

European Editor

R. Zandonini

Trento Univ., Italy

Email: riccardo.zandonini@ing.unitn.it

Advanced Steel Construction

an international journal

VOLUME 13 NUMBER 2

JUNE 2017

Technical Papers

- | | |
|-----------------------------------------------------------------------------------------------------------------------------------------------------------------------------|-----|
| Experimental Study on the Fundamental Mechanical Features of Cable-Supported Ribbed Beam Composite Slab Structure
<i>Wentao Qiao, Qi An, Mingshan Zhao and Dong Wang</i> | 96 |
| Nonlinear Stability Analysis of a Radially Retractable Suspen-Dome
<i>Jianguo Cai, Yangqing Liu, Jian Feng and Yongming Tu</i> | 117 |
| Integrated Fire-Structure Simulation of a Localized Fire Test on a Ceiling Steel Beam
<i>Guo-Qiang Li and Chao Zhang</i> | 132 |
| Structural Performance of Boltless Beam End Connectors
<i>S.N.R. Shah, N.H. Ramli Sulong, R. Khan and M.Z. Jumaat</i> | 144 |
| Thermal Modelling of Load Bearing Cold-Formed Steel Frame Walls under Realistic Design Fire Conditions
<i>A.D. Ariyanayagam, P. Keerthan and M. Mahendran</i> | 160 |

EXPERIMENTAL STUDY ON THE FUNDAMENTAL MECHANICAL FEATURES OF CABLE-SUPPORTED RIBBED BEAM COMPOSITE SLAB STRUCTURE

Wentao Qiao^{1,*}, Qi An², Mingshan Zhao³ and Dong Wang⁴

¹Associate Professor, School of Civil Engineering, Shi Jiazhuang Tiedao University, China

²PhD. Student, School of Civil Engineering, Tianjin University, China

³Research Fellow, School of Civil and Environmental Engineering, Nanyang Technological University, Singapore

⁴PhD. Student, Department of Civil and Environmental Engineering, UAH, Huntsville, United States

*(Corresponding author: E-mail: tottyer@126.com)

Received: 15 October 2015; Revised: 14 April 2016; Accepted: 30 April 2016

ABSTRACT: In this study, experiments were carried out to investigate the fundamental mechanical features of the cable-supported ribbed beam composite slab structure (CBS). A 1:5 scaled physical model was designed, fabricated and tested. The feasibility and rationality of the CBS fabrication and construction are discussed and justified. The theoretical analysis used to predict the deflection and member forces is verified. It is shown that the CBS is equipped with high stiffness and behaves linearly in terms of force-displacement relationship and all the cable forces, structural deformation, stress of the ribbed beam and strut stresses are symmetrically distributed. Through comparison analysis, the mechanical features of each span are found to be similar and each span can be considered as a relatively independent mechanical unit. When the CBS is loaded, the stresses in the ribbed beam increase gradually from the two ends towards the center, where the maximum stress and deformation locates eventually, while the distribution of cable forces and strut stresses is the other way around. Further monitoring also shows that the temperature effect on the CBS is not significant since the interior constraint forces are self-balanced by the self-adjustable support.

Keywords: Cable-supported ribbed beam composite slab, mechanical features, pre-stress, fabrication, experimental research

DOI: 10.18057/IJASC.2017.13.2.1

1. INTRODUCTION

The merits of cable-supported spatial structure systems [1] come from the combination of rigid structures such as shell, grid structure and flexible structures such as cable network structures [2, 3]. Because of the action of the pre-stressed cables, such systems are highly efficient in load-deformation performance and usually self-balanced. The cable-supported spatial structure systems including beam (truss) string structure [4-7], suspend-dome structure [8, 9], and cable-supported barrel vault structure [10-13], have been widely used in the public buildings around the world. The cable-supported ribbed beam composite slab structure (CBS) is one of such structures that effectively utilize different building materials. The concept of the CBS was put forward by Chen and Qiao [14] for the first time. They investigated the basic static and dynamic features by using numerical simulation method. Later, Qiao et al. [15] presented the construction method of the CBS and fabricated a bamboo model to study the basic static and dynamic characteristics. This structure consists of the upper concrete slab, middle struts and lower cables. The struts behave as flexible supports between the upper concrete slab and lower cables, transferring loads between these two. Due to mechanical benefits by this configuration, CBS can easily span long distance when used as floor or roof systems.

In this study, experiments were carried out to investigate the fundamental mechanical features of the cable-supported ribbed beam composite slab structure (CBS). A 1:5 scaled physical model was designed, fabricated and tested. The feasibility and rationality of the CBS fabrication, the precision

of the theoretical analysis method and the mechanical behavior of the CBS are discussed. The rest of this paper is organized as follows: Section 2 describes the basic fabrication and construction processes of the CBS. Section 3 discusses the basic mechanical features of CBS theoretically, including self-balanced system and pre-stress design method. Section 4 determines the 1:5 scaled experimental model, loading scheme and data collecting method. In order to figure out the actual mechanical features of the CBS in detail, the monitored data including deformation, cable force, strut stress and ribbed beam stress are also analyzed in section 5.

2. FABRICATION

2.1 Connection Design

From top to bottom, the CBS consists of the upper reinforced concrete slab, ribbed beam, the middle steel strut, and the lower cable, as shown in Figure 1. All the members are prefabricated and assembled on site. Pin-pin joints are used for most of the connections, and a special joint is designed for the connection between the strut and the beam, as shown in Figure 2. This configuration grants the whole connection the ability to rotate in multiple directions: the upper pin joint can rotate about the longitudinal direction of the cable, while the lower pin joint is used to adjust the angle of strut so that it can be fit into the support easily. Obviously, this configuration enables efficient and effective load transfer between cables and upper deck. At the both ends of the cable, another pin joint is used to fix the cable into the anchorage, as shown in Figure 3.

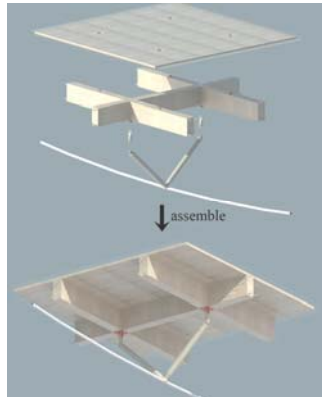


Figure 1. Fabrication of Unit



Figure 2. Strut Junction

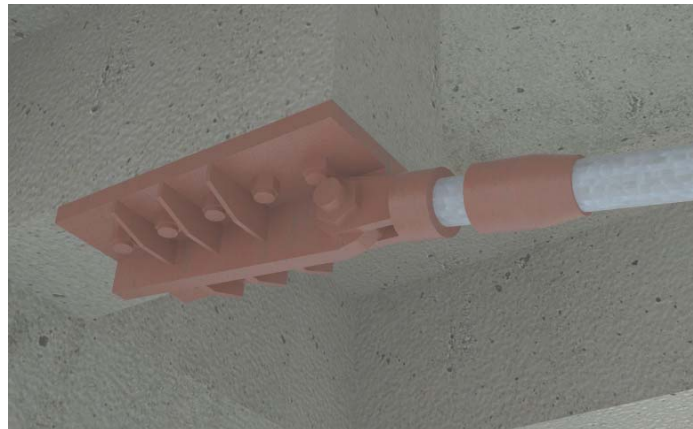


Figure 3. Anchorage of Cable End

2.2 Construction

Since the slabs, beams, struts, cables and joints are prefabricated and then assembled on spot, strengthening of the connections is necessary. In this case, casting concrete is performed to strengthen the connection among the prefabricated slabs or beams. The other detailed and worthy attention is that one end of the CBS is fixed and the other end is allowed to slide freely in the horizontal direction. By the merits of this configuration, the horizontal cable force can be released, while the vertical cable force can act on the upper slab system through struts efficiently. Besides, in order to smoothly transfer the major shear forces between the beams and slabs, the four angle-steel elements on ribbed beams are inserted into the four holes in the slab (Figure 1). Meanwhile, this type of connection can enhance the integrity of the upper slab system.

The major construction processes of CBS are illustrated as follows:

Step 1. The ribbed beam elements. Before assembling the beam elements, temporary and removable scaffold will be built to support the construction of the current span. When the construction of the current span is completed, the scaffolds are moved to the next span. The steel bar cages are set up among prefab beam elements, which are marked with red circles shown in Figure 4.

Step 2. Casting concrete and installing the cable supported systems. The configuration of the pre-stressing system is shown in Figure 4. After the pre-stresses in the cables are successfully applied and properly adjusted, the upper beams and the lower cable-supported system will form a complete self-balancing structure system.

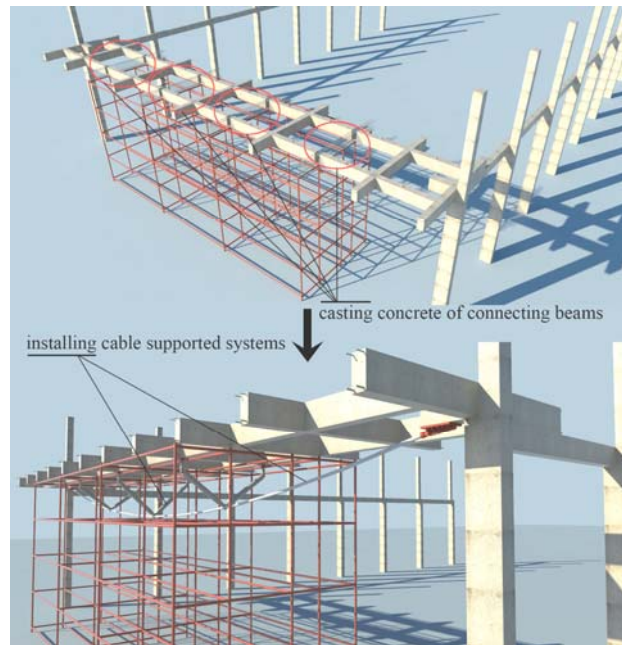


Figure 4. Step1 and 2 Constructions

Step 3. Paving the slabs and inserting the angle-steel elements. After casting concrete into the holes and the belts among the slabs, one complete span CBS construction is completed. The same process is repeated on the second span until all the spans are constructed.

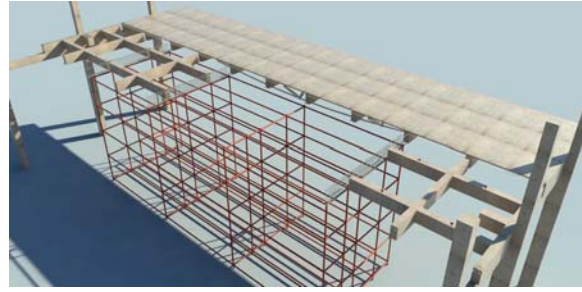


Figure 5. Step 3 Construction

Step 4. System integration and scaffold removal. The construction is finished and the CBS can fully function now. Figure 6 shows a final rendering of the CBS with large interior space.

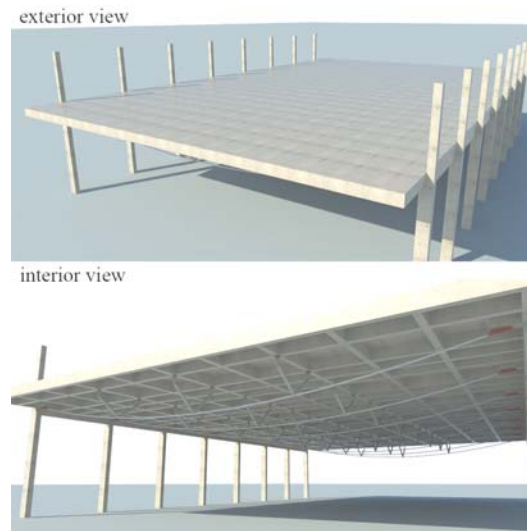


Figure 6. Final Step Rendering

3. MECHANICAL FEATURES

3.1 Self-balanced System

With the cable being fully pre-stressed, the CBS becomes a self-balanced structural system. Figure 7 shows the force flow diagram of the CBS. Due to the tensile force in the cable, struts and the ribbed beams and slabs are under compression. The struts function as flexible supports, and provide supporting forces to the ribbed beams and slabs. As a result, the action of bending moment on the ribbed beams and slabs is reduced significantly.

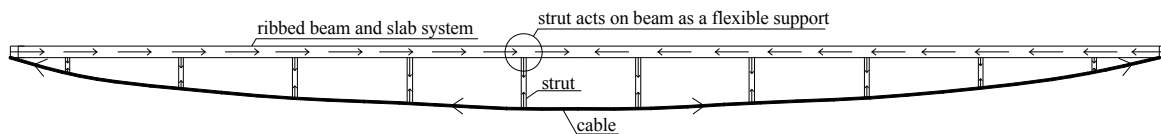


Figure 7. Force Flow Diagram of the CBS

3.2 Pre-stress Design

It can be obviously seen from Figure 7 that the pre-stress of the cable is the key to maintain the self-balance, stiffness and the load-bearing capacity of the CBS. Obviously, it is of great importance to figure out the pre-stress value precisely. The guidance adopted in the design of pre-stress system is shown as follows (limiting the deformation): First, the pre-stress can make the CBS (without paving slabs, namely, in the state of construction step 2.) deform upwards. The maximum deformation should be limited to less than $span/600$ [14]. Secondly, after pre-stressing the cable and paving slabs, namely, in the state of construction step 3, the upward deformation will be decreased. The rational pre-stress should keep the upward deformation no less than zero. If the pre-stress determined according to the two rules above cannot meet the demands of the load-capacity and rigidity, the following reasons may exit: the rigidity of the upper ribbed beam and slab system is too small, the sag-span ratio of the CBS is irrational, or the structure has other problems.

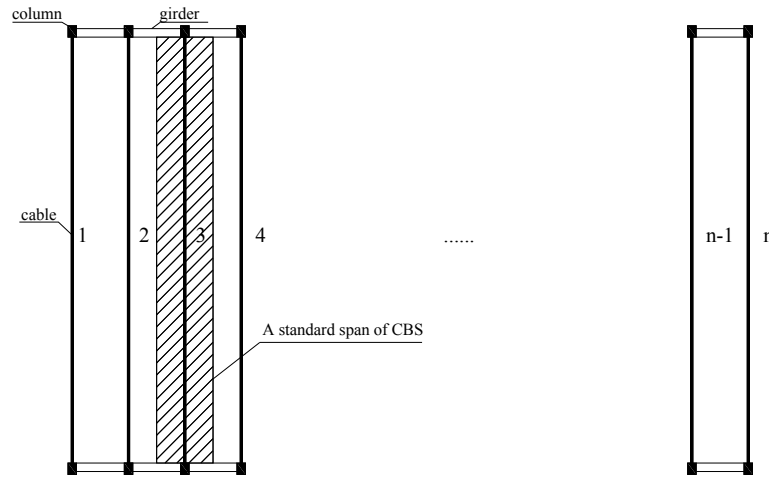


Figure 8. Cable Disposition

As shown in Figure 8, a standard span of CBS is taken to illustrate the detailed pre-stress design process. In the beginning, the only load is from the weight of the CBS in the construction step 2. The cable pre-stress is set to zero, i.e. $T_p = 0$. As the deformation control point of the CBS, the mid-span point vertical displacement is recorded as d' . Note that all of the deformation discussed in this paper is based on the zero state, (drawn in dash line and shown in Figures.11 and 12), in which the displacement above this zero state is positive, while below is negative.). The concept is similar to the cable force, i.e., F' . In the first tensioning, the cable pre-stress is set to F' , namely, $T_p = F'$. The mid-span point vertical displacement and cable force can be determined again, marked as d and F , respectively. D is the preset value of the maximum upward displacement of the mid-span point. If $d \neq D$, $T_p = F' + F' \times (D-d) / (D-d')$ will be applied to the cable, and the structure will be recalculated. This process will be repeated until $d = D$, and then we can get the cable pre-stress design value $T = F$. It is commonly accepted that for the analysis of pre-stressed structures, the nonlinear analysis method should be adopted in order to simulate actual mechanical behaviors of the structure system precisely [16]. In this paper, the general FEM software Midas/gen is used to consider the geometric nonlinearity of the CBS. The iteration calculation workflow is shown in Figure 9.

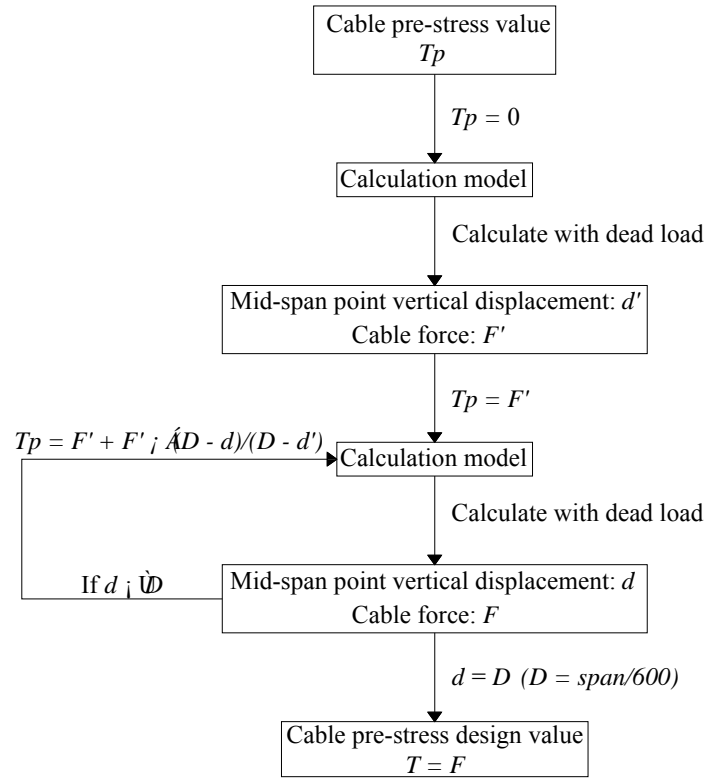


Figure 9. Pre-stress Finding Iteration Workflow

In the process of calculating the cable pre-stress of CBS, sometimes it is not easy to converge to the completely precise preset value D , as shown in Figure 10. It is clearly seen that the mid-span point vertical displacement d is getting close to the objective D from the n th iteration step. With some delay, d also gets close to the D and keeps fluctuating. Therefore, a preset value close to $D = \text{span}/600$ can get reasonably close to the optimum. As shown in Figure 10, if a tiny error $\pm t$ is set (dash line in Figure 10), the non-convergent iteration curve will be able to converge at step $n+1$.

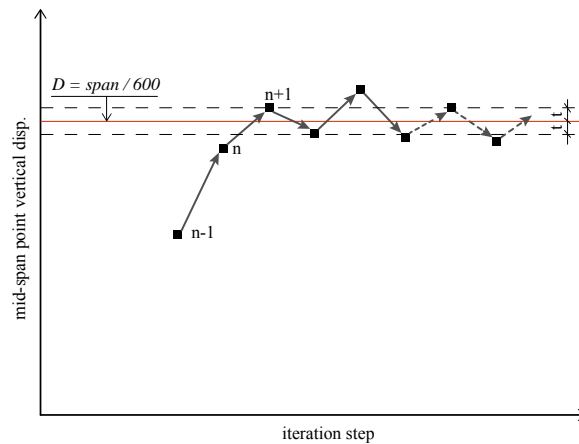


Figure 10. Convergence analysis

3.3 Prototype Analysis

The gymnasium roof of Hebei Normal University in China is chosen as the calculation prototype. For this gymnasium, there are 13 standard spans and each span is 42.25m long. The standard span

is composed of 10 standard units (shown in Figure 1). The key dimension of the model is shown in Figure 11. Note that the strut is V type as shown in cross section 2-2, the circular steel tube with section of 159mm×10mm (external diameter×thickness) is adopted, and the cable is the steel strand with section of 80mm in diameter.

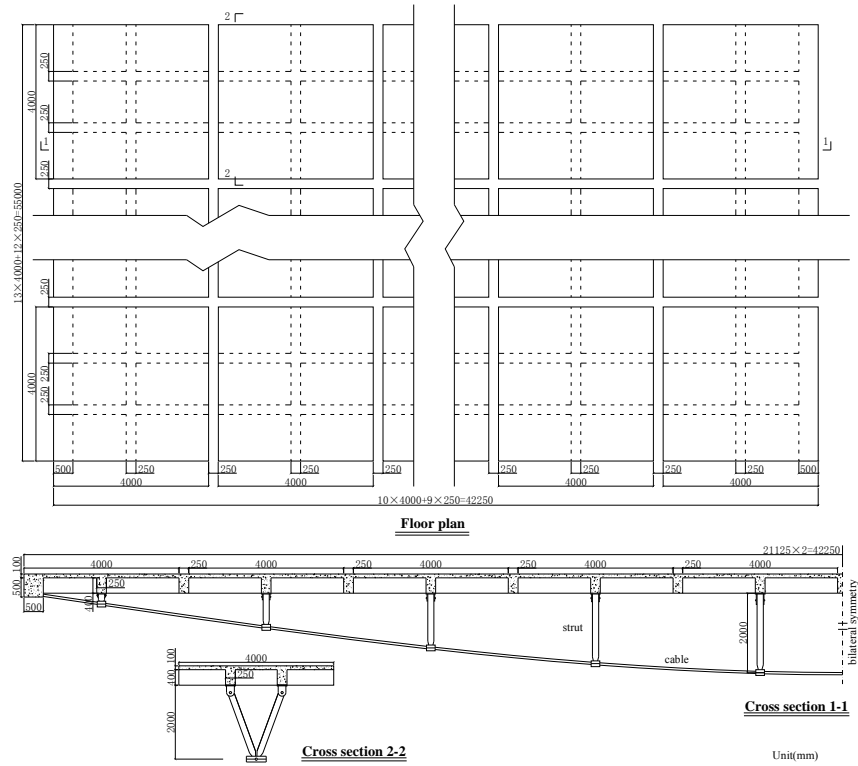


Figure 11. Model's Key Size Drawing

According to the convergence acceleration method shown in Figure 10, a threshold value involved with the error t is assigned in the analysis procedure. In this example calculating, 0.05 is taken as the threshold value, which means $\pm 5\%$ ($t = 5\% \times D$) error is allowed. The iterative process is shown in Figure 12.

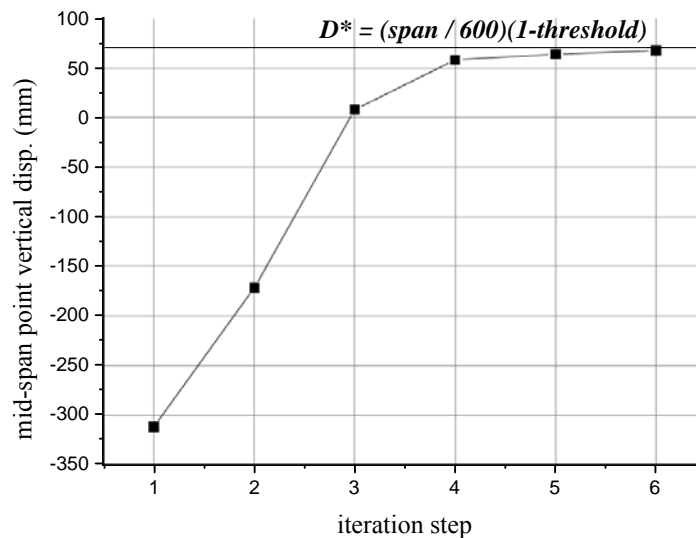


Figure 12. Iteration Process

It is obviously shown in Figure 12 that the iteration converges at the 6th step, and the mid-span point vertical displacement value is 67.6mm. Compared with the target value $D = span/600$, the error of the mid-span vertical displacement is only about 4%. Actually at the 5th iteration step the corresponding displacement value is 63.8mm, and the error is 9.4%, which is also acceptable as the pre-stress design value.

In order to verify the rationality of the pre-stress design value, with this pre-stress applied to the cable, the deformation of the structure in the state of construction step 3 (described in section 2) is calculated. Apparently, the rational pre-stress may be a range of values, and the smaller one is preferred. At the 5th iteration value, the corresponding pre-stress design value is 1900kN. The deformation of the structure is illustrated in Figure 19. In construction step 3, the prefabricated concrete slabs will be paved on top of the ribbed beams. Because of the extra dead load of the slabs, the CBS in the construction step 2 equilibrium states will deform downwards, and the final deformation of the CBS is shown in Figure 20. The vertical displacement of the mid-span point is positive 15.4 mm which is still above the zero state, and can meet the demand of reasonable pre-stress design value described in section 3.2. Moreover, the internal force of the cable also increases because of the dead load of the concrete slabs. The calculated value is 2533 kN, which is 633 kN bigger than the tension 1900 kN in construction step 2.

4. EXPERIMENTAL SCHEME

4.1 Physical Model

Based on the prototype introduced in section 3.3, a 1:5 scaled model is fabricated. The scale factors are worked out according to the similarity constant and similarity ratio relationship in static loading experiment of engineering structure [17].

For geometric dimensions shown in Figure 11, the ratio of scaled model to the full scale model is 1:5. For the cable tension and structural displacement, the ratio of scaled model to the full scale model is 1:25 and 1:5. The scaled physical model and its construction processes are shown in Figure 13. (3 standard spans are fabricated and tested)

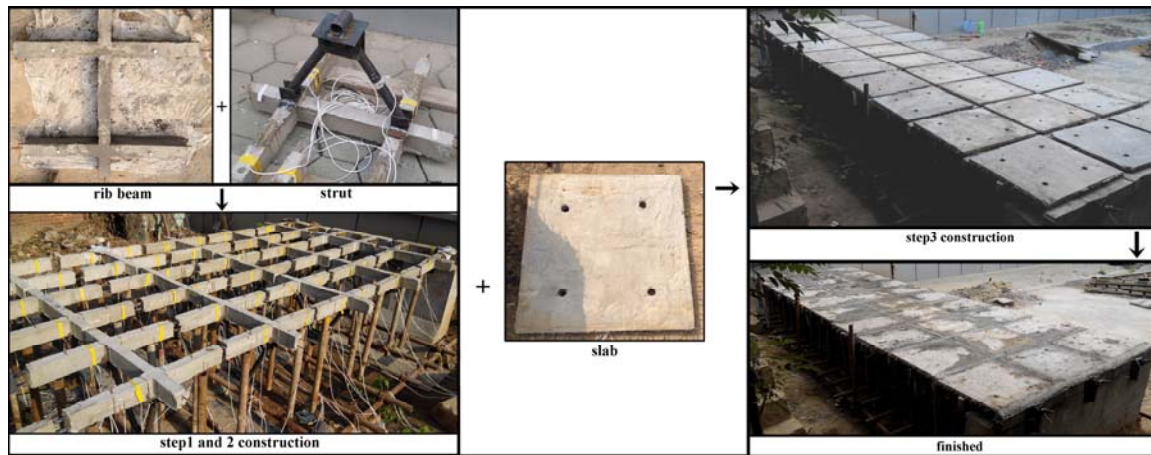


Figure 13. Scaled Physical Model

4.2 Loading Scheme

Considering the site conditions of the experimental model, the surface loads on the slabs are applied using stacking sand bags while the pre-stress in the cable is applied through tightening the screws at the two ends of the cable.

The cable pre-stress values were figured out in section 3.3. According to the similarity constant and similarity ratio relationship in static loading experiment of engineering structure, the pre-stresses in cables are set to be 1/25 of the loads in the cables of the prototype. In order to distribute the loads stably and evenly in the cables, the pre-stressing process is divided into four stages. The tension control values of each stage are shown in Table 1.

Table 1 Applied Tension for Each Stage

Stage	Ratio (%)	Tension (kN)	
		Prototype	1:5 Scaled model
1	65%	1200	48
2	80%	1500	60
3	90%	1700	68
4	100%	1900	76

The calculation of the surface loads employs the fundamental load combination method [18], i.e. $1.2 \times \text{dead load} + 1.4 \times \text{live load}$. To apply the loads on the slabs, about 50kg of sand bags are needed for each slab. In order to make sure that the loads are distributed evenly, the loading process of the surface loads is divided into 5 steps. The detailed loading program is shown in Table 2. The actual load distribution is shown in Figure 14.

Table 2 Load Step Increment

Step	Ratio (%)	Load (kg)	Increment (kg)
1	20%	10	10
2	40%	20	10
3	60%	30	10
4	80%	40	10
5	100%	50	--



Figure 14. Load Distribution

4.3 Data Measurement

The YE2539 high speed static strain indicator, two strain collection extension boxes and one computer are employed as the strain measurement system, as shown in Figure 15. The strain measurement locations on the ribbed beams are shown in Figure 16. The three standard spans are marked span I, span II and III, respectively. In each span, the strain measurement locations of the ribbed beams are numbered from left to right. The measurement points on the upside ribbed beams are marked U, and the corresponding downside ones are marked D. This structure is symmetric at both sides according to the mid-span point for a measurement point, whose symmetric point is marked with '. For example, the I-U1 means the first measurement point of the upside ribbed beam of the first span and the symmetric point of this span is marked as I-U1'. The marking numbers are shown in Figure 16. The strain measurement points on the struts are numbered similarly: The left limb of the V-shaped strut is marked as I-SL1, and the right limb is marked as I-SR1; the corresponding symmetric points are I-SL1' and I-SR1', respectively, as shown in Figure 17.

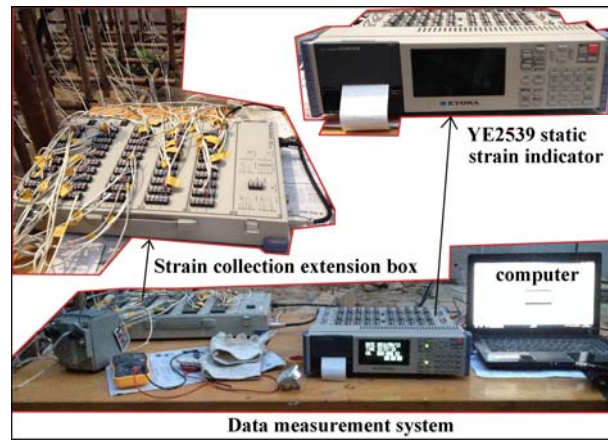


Figure 15. Strain Measurement System

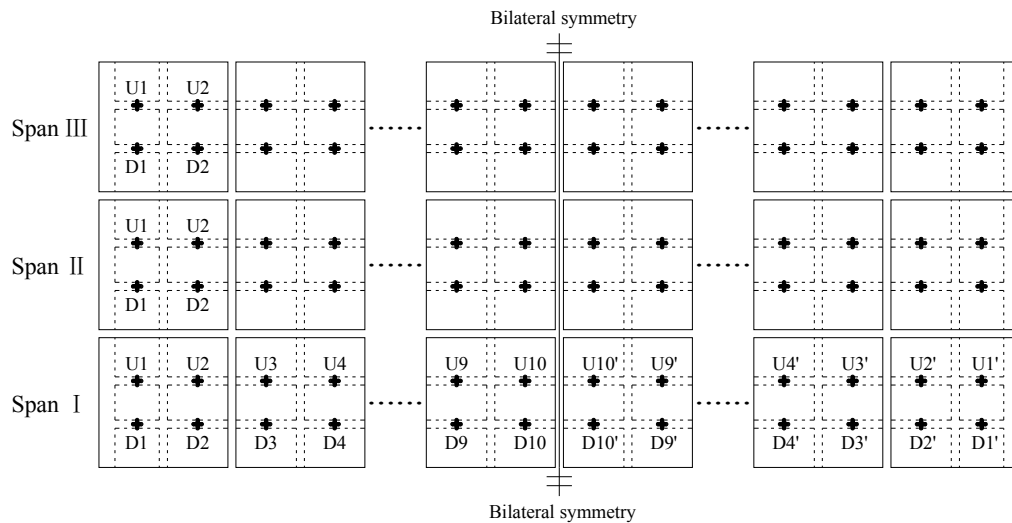
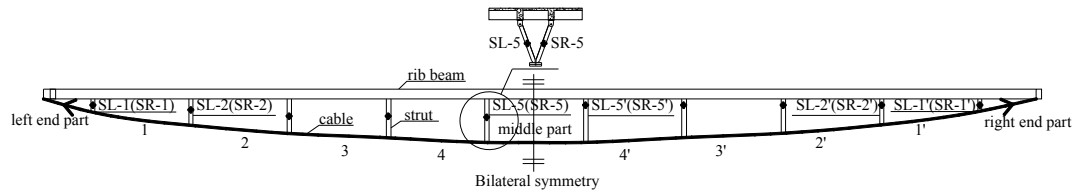


Figure 16. Strain Measurement Points of Ribbed Beams



Moreover, the cable forces are monitored by a INV3080B-BCF cable force tester, as shown in the bottom right of Figure 18. The measurement points on cable forces are shown in Figure 17. The structural displacements for each standard span are measured by dial indicators. Four indicators are distributed at two 1/4 span points, mid-span point, and sliding hinge support, respectively, as shown in the left and top right of Figure 18.

5. TEST RESULTS ANALYSIS

5.1 Construction Stage Analysis

Table 3 lists the measured cable forces and characteristic displacements of the experimental model at step 2 and 3, Note that $\text{error} = 100\% \times (\text{practical value} - \text{theoretical value}) / \text{theoretical value}$.

Table 3. Vertical Disp. Comparison

Item	Step 2			Step 3		
	Theoretical value.	Practical value	Error (%)	Theoretical value.	Practical value	Error (%)
Cable force (kN)	76	81.17	6.8	101.32	111.05	9.6
Mid-span vertical disp. (mm)	12.76	13.26	3.9	3.08	2.68	-13.1
Left 1/4 span Vertical disp. (mm)	13.52	13.8	2.1	4.24	3.90	-8
Right 1/4 span Vertical disp. (mm)	13.52	13.97	3.3	4.24	3.81	-10.2
Horizontal disp. (mm)	1.52	1.58	3.9	0.82	0.77	-6.1

It can be seen from table 3 that when the cables are tensioned in step 2, the deformation of the structure agrees well with the theoretical values and the errors are all less than 4.0%. Although the practical cable force is larger than the theoretical value, the error is only 6.8%. In construction step 3, the maximum error of the cable force is 9.6%, and the displacement is -13.1%, which are also in the acceptable range. Therefore, it can be concluded that the theoretical analysis method introduced in section 3.2 is reasonable.

5.2 Cable Force Analysis

At fully loaded status, the cable forces of each span are shown in Figure 21.

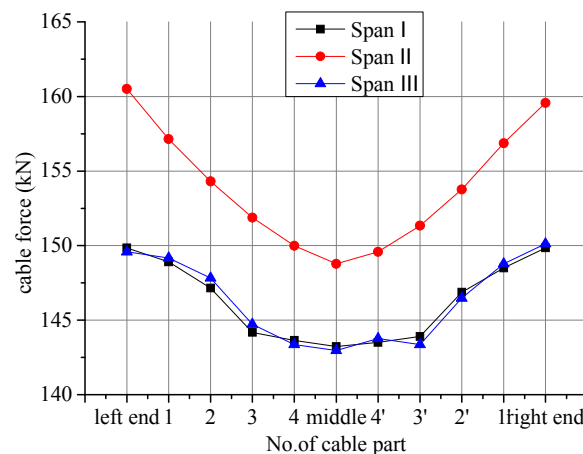


Figure 21. Cable Force under Full Load

Three key features can be read from Figure 21. Firstly, the cable forces in all the spans distribute symmetrically about the middle axis in accordance with the geometrical symmetry of the structure. The forces are higher at both ends and gradually decrease from the end to the middle. The differences between the maximum and the minimum are all within 10%, indicating that the forces

are generally uniform in the cables. Secondly, the force distribution in the transverse direction is also symmetrical about the neutral axis. The forces in the cable of Span II are higher than those of Span I and III, which is reasonable since Span II is in the middle and has to carry more loads. Still, the differences are very small. It can be seen from Figure 21 that the maximum difference is only 6.6%.

The variation of the maximum cable force during the loading is also monitored, as shown in Figure 22. From Figure 22, it can be seen clearly that the cable force increases with the externally applied load. Although a couple of points deviate from the dash line, the variation is quite slight. Accordingly, the increasing of cable force can still be treated as linear.

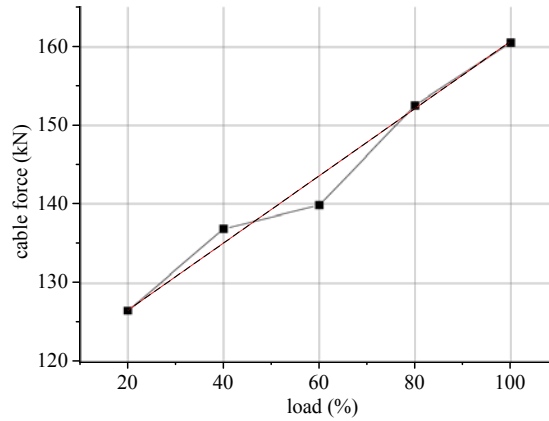


Figure 22. Changing Curve of Max. Cable Force

5.3 Displacement

Figure 23 shows the vertical displacement of the critical points of each span at the full load condition.

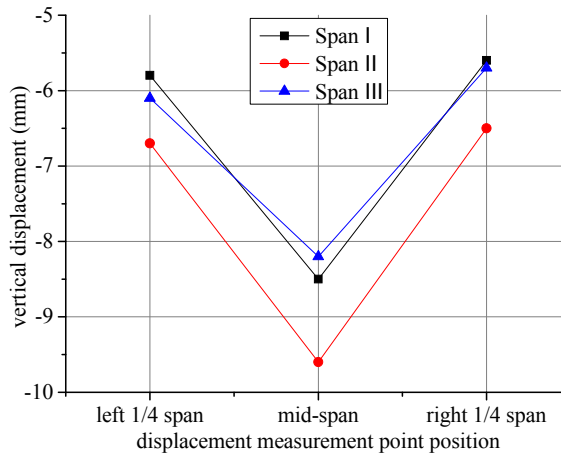


Figure 23. Vertical Displacement under Full Load

It can be seen clearly from Figure 23 that the vertical displacements are generally symmetric about the mid span neutral axis. The characteristic displacements of Span I and III are almost the same at the same locations. The biggest difference is only 0.3mm, as shown in Figure 23. The displacements of Span II are slightly larger than those of Span I and III because it is the center span. However, the biggest difference is still less than 1.5mm.

The load-displacement curve of the center point of the Span II is plotted as shown in Figure 24. This curve presents the evolution of the maximum vertical displacement of the whole structure during loading. From Figure 24 it can be seen that the vertical displacement increases as the load augments. Although some points deviate from the dash line, the overall trend is still very close to the dash line. Generally, the vertical displacement changes linearly.

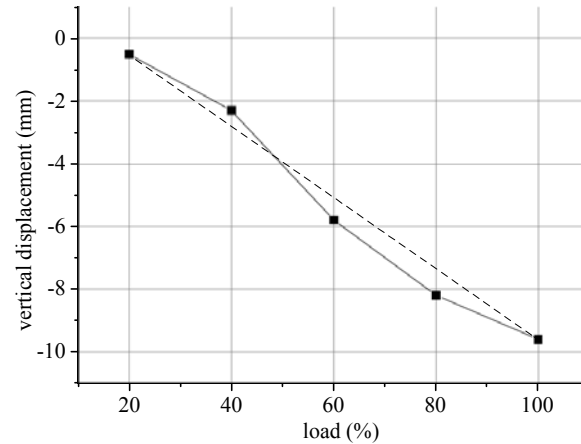


Figure 24. Changing Curve of Max. Displacement

5.4 Stress of Ribbed Beam Analysis

Throughout the loading, the strains of ribbed beams are monitored. The strain data are then converted into stresses according to the Hooke's law. The stresses at the full load condition are shown in Figures 25-27. As described in section 4.3, shown in Figure 15, I-U means span I, upside ribbed beam, while I-D means span I, downside ribbed beam, and so on, for II-U, D and III-U, D.

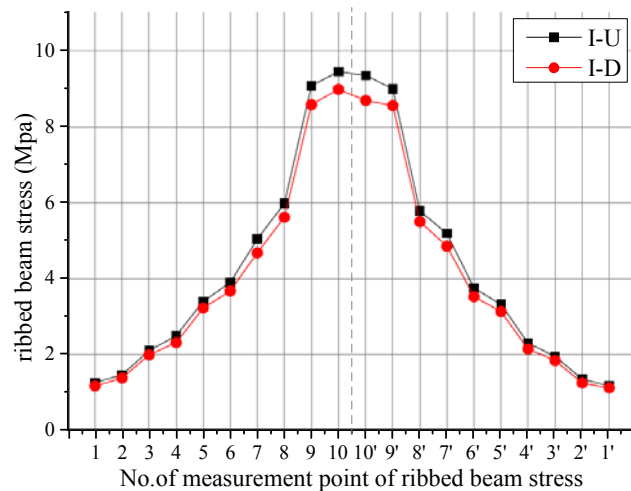


Figure 25. Ribbed Beam Stress of Span I under Full Load

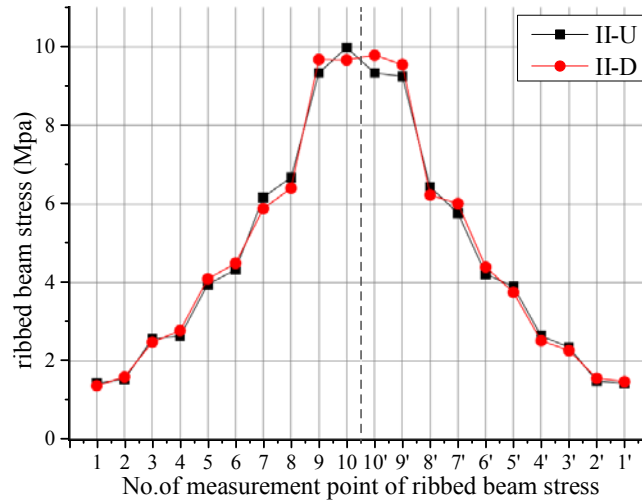


Figure 26. Ribbed Beam Stress of Span II under Full Load

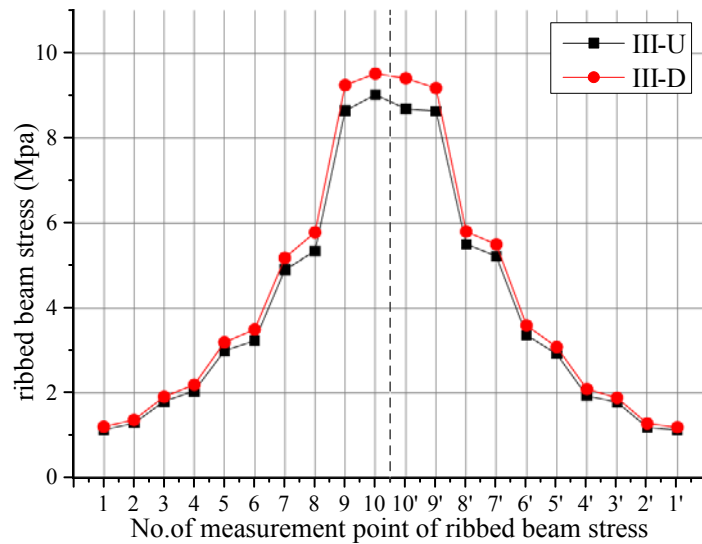


Figure 27. Ribbed Beam Stress of Span III under Full Load

Two important features can be read from Figures 25-27. Firstly, in each span, both the upside and downside ribbed beam stresses distribute symmetrically about the middle line (the dash line). The stresses increase gradually from the two ends to the middle and form a plateau in the middle. Secondly, for each span, the upside and downside ribbed beam stresses almost keep the same level and distribution rule. The maximum difference for each span is usually located at the middle part and the maximum difference in the whole model is only 7.6%.

In each span, all the monitoring points of ribbed beams are investigated and the results are drawn in Figure 28. We can find out that three curves representing the ribbed beam stress distribution almost keep the same level and rule, the maximum difference is about 7.1%.

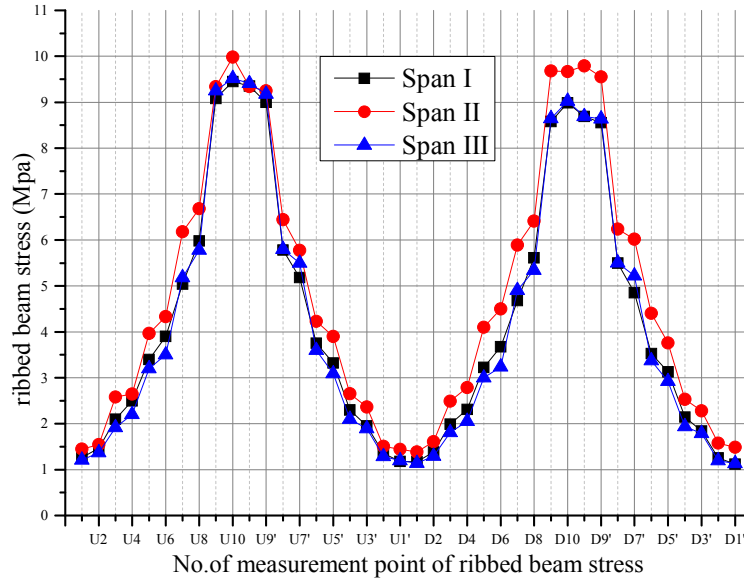


Figure 28. Ribbed Beam Stresses of All the Three Spans under Full Load

The maximum stress location is at measurement point II-U10, which is taken to analyze the variation feature of the ribbed beam stress during the loading process. The relevant data are collected and shown in Figure 29. The stress increases as the load augments, although several points deviate from the dash line, they are all close to the dash line. In general, the ribbed beam stress changes linearly.

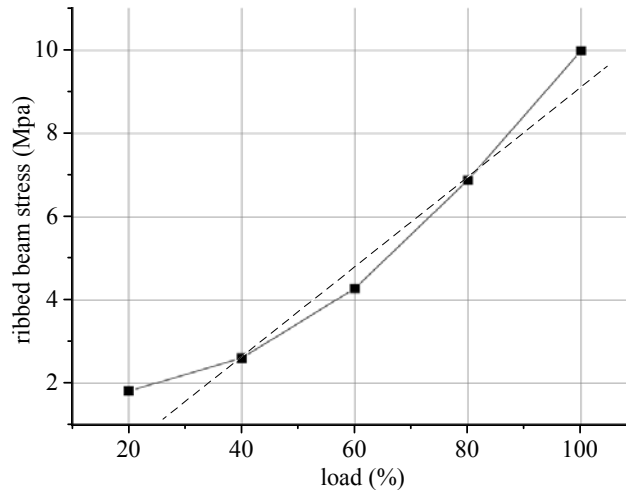


Figure 29. Changing Curve of Max. Stress of Ribbed Beam

5.5 Stress of Strut Analysis

Similar to the ribbed beam stress analysis, the strains of the struts are monitored and converted to stresses as well, as shown in Figures 30-32. As described in section 4.3, shown in Figure 17, I-SL means span I, left limb strain monitoring point of V type strut; I-SR means span I, the right limb strain monitoring point, and so on for II-SL, SR and III-SL, SR. Note that all the stresses in the struts are compressive stress, as marked negative in the figures.

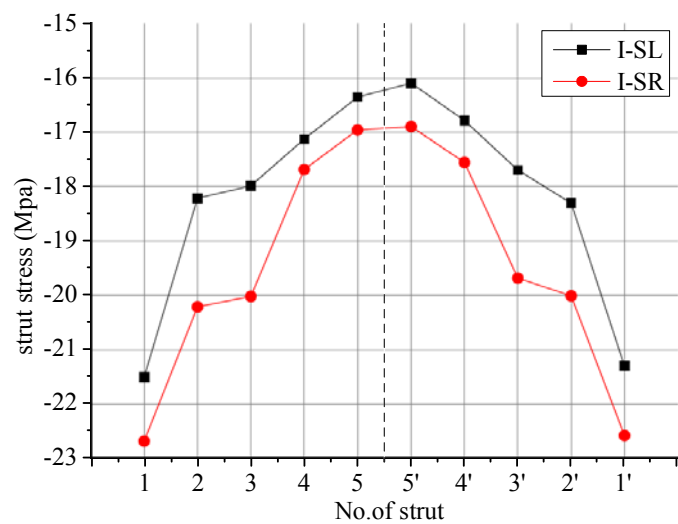


Figure 30. Strut Stress of Span I under Full Load

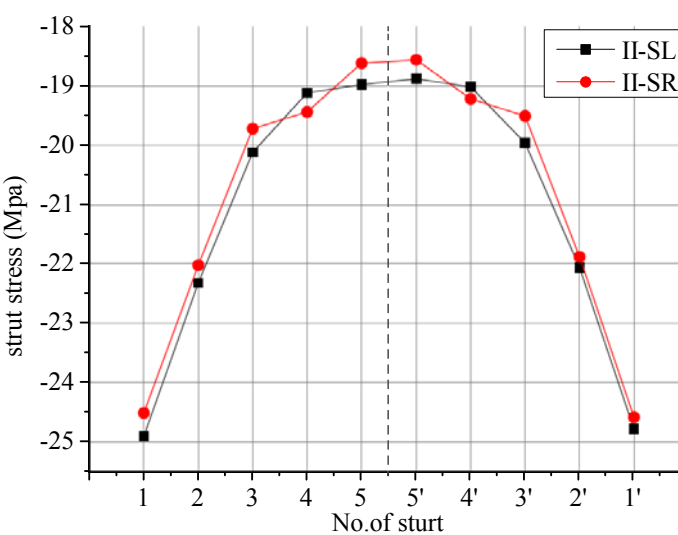


Figure 31. Strut Stress of Span II under Full Load

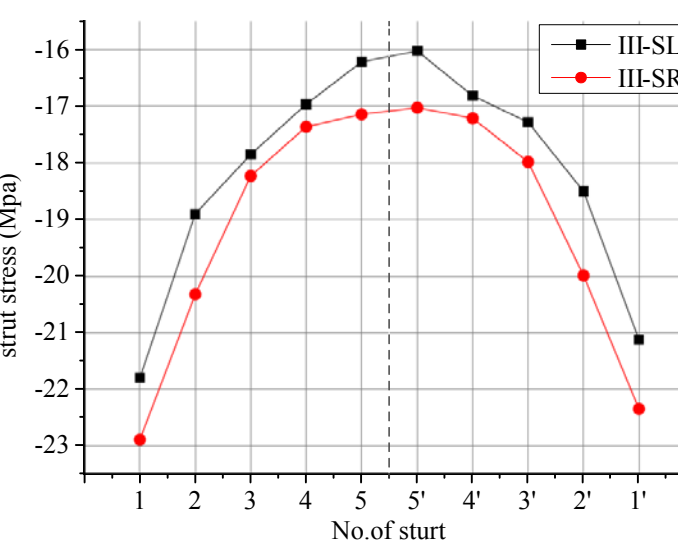


Figure 32. Strut Stress of Span III under Full Load

It can be obviously seen from Figures 30-32 that in each span, both the stress in left and right limbs of the V type strut distribute symmetrically about the center line (the dash line) and decrease gradually from the two ends to the center. In span II, the stress in left and right limbs of the V type strut keep almost the same level and distribution pattern. The same situations happen to the span I and III. The difference of stress between left and right limbs in Span I and III are larger than that in span II, i.e. about 5.9%. However, this value is still very small compared at the global level.

In each span, all the measurement points of struts are investigated and the results are shown in Figure 33. It can be seen that three curves representing the strut stress distribution almost keep the same rule, especially for span I and III. For span II, because of the different boundary condition, the strut stress is larger than the corresponding value in span I and III, and the maximum difference is about 17%.

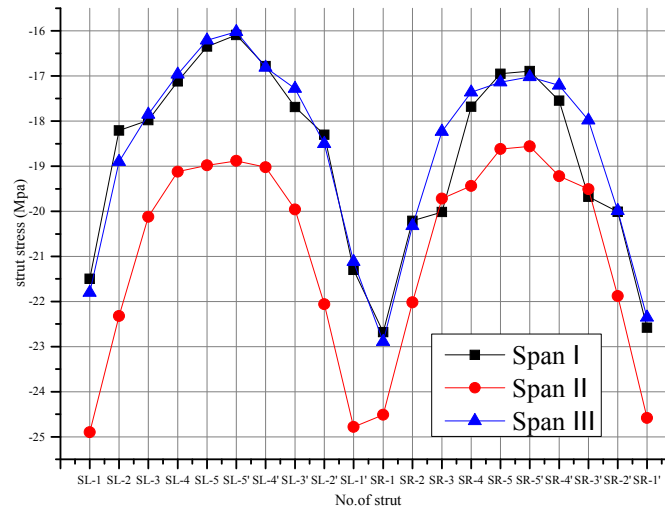


Figure 33. Distribution of All Strut Stresses under Full Load

The maximum stress location is at measurement point II-SL-1. The relevant data are collected and shown in Figure 34. The strut stress increases as the load augments. Some points deviate from the dash line, but they are all close to the dash line. Consequently, the strut stress changes linearly basically.

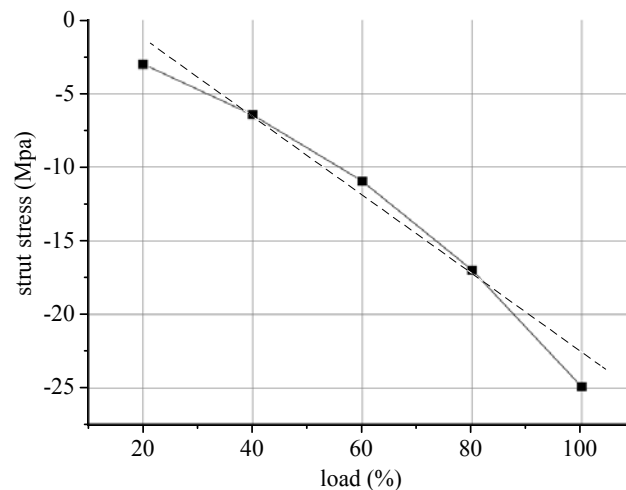


Figure 34. Changing Curve of Max. Strut Stress

5.6 Effect of Temperature

The action of temperature on CBS structure was studied in this experiment as well. It was spring season and the temperature was about 15°C when the model's construction was finished, namely, the closure temperature of this test model is 15°C . In order to investigate the temperature action, the test model was kept through one whole year, the highest temperature is about 40°C in the summer, and the lowest temperature is about -15°C in the winter. Consequently, based on the closure temperature, the temperature difference varies from -30°C to 25°C .

In the experiment, the temperature of all the three spans was measured by thermometer, and the cable forces were selected to illustrate the action of temperature on the structure. The cable was divided into nine segments in each span, the number of which is shown in Figure 17. the cable force of each segment was measured by the same way used in section 4.3, and the data were collected and analyzed respectively at -15°C , -5°C , 5°C , 15°C , 20°C , 30°C , 40°C . The results were shown in Figs. 35-37. It can be seen that the changing rule of the cable force of each segment in all the three spans are similar, compared with the mechanical status at the closure temperature, namely 15°C . When the temperature goes up, the cable forces almost keep increasing, but keep reducing with the temperature going down. The maximum positive changing rate (when the temperature difference is 25°C) is about 12.9%, and the maximum negative changing rate (when the temperature difference is -30°C) is about -8.7%. In consequence, the action of the temperature on the CBS is not significant. The self-adjustable supports can release the internal constraint forces induced by the temperature effectively.

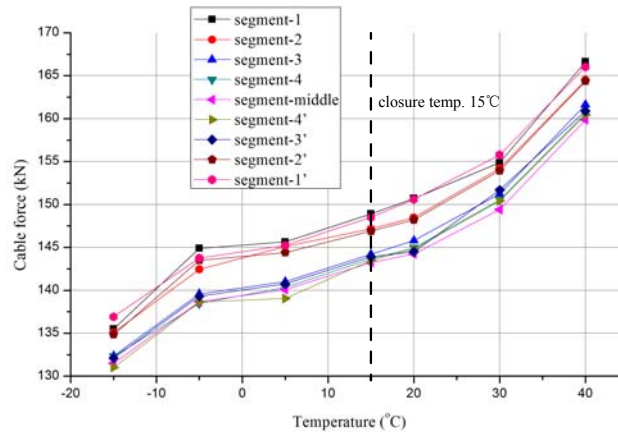


Figure 35. The Changing of SPAN I Cable Forces at Different Temperature

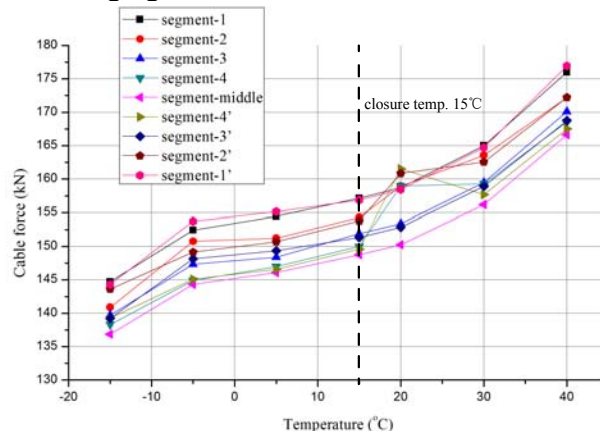


Figure 36. The Changing of SPAN II Cable Forces at Different Temperature

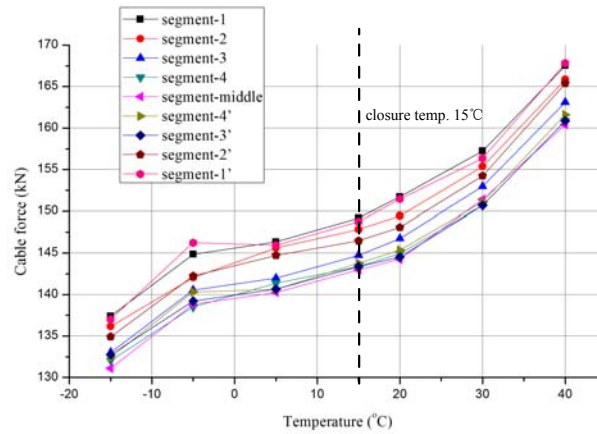


Figure 37. The Changing of SPAN III Cable Forces at Different Temperature

6. CONCLUSIONS

In this paper, the fundamental mechanical characteristics were investigated through experimental study. Test results showed the feasibility and constructability of the CBS, and verified the predicted behavior by the theoretical analysis. The key conclusions are listed as follows.

- (1) During the loading process, all of the cable forces, vertical displacement, stresses of ribbed beam and strut stresses approximately augment linearly with the increasing load. It indicates that although most of cable-supported structures are flexible and behave nonlinearly, if properly designed, it can achieve a high global rigidity and behave approximately linearly.
- (2) CBS is usually designed symmetrically, in order to make all of the cable forces, structural deformation, stresses of ribbed beam and strut stresses distribute symmetrically. For each span of CBS, the maximum vertical displacement is located in the mid-span area. The cable forces decrease gradually from the two ends to the middle, the minimum is located in the middle part. Similarly, the minimum strut stress is located in the middle. While the stresses of ribbed beam increase gradually from the two ends to the middle, the maximum is located in the middle.
- (3) For each V type strut, the stress of left and right limbs are almost the same, the maximum difference is only 5.9%.
- (4) The cable forces in different spans keep the same distribution rule. For span I and III, even the values are very close. Although the corresponding cable forces in span II are larger because of the different boundary condition, the difference is still small on the whole. The same situations also happen in vertical displacement, stresses of ribbed beam and strut stresses. It indicates each span of CBS has the same mechanical features approximately, can be considered as an independent mechanical unit and represent the whole structure, which are in accordance with the theoretical calculation hypothesis.
- (5) The temperature difference ranging from -30°C to 25°C was investigated. For the CBS, when the temperature goes up, the cable forces almost keep increasing, but keep reducing with the temperature going down. When the temperature difference is 25°C , the maximum positive changing rate of the cable force is about 12.9%. When the temperature difference is -30°C , the maximum negative changing rate of the cable force is about 8.7%. The overall action of temperature on the CBS is not significant, since the self-adjustable supports release the internal constraint forces induced by the temperature effectively.

ACKNOWLEDGEMENTS

This work is sponsored by the National Natural Science Foundation of China (No.51208317), and Hebei Province Natural Science Fund (No.E2016210052). Special acknowledgement is also given to China Scholar Council for supporting this research in MIT, and to Prof. Nader Tehrani for his invitation and generous helps to me.

REFERENCES

- [1] Qiao, W.T., "Study of Cable-supported Structure System", PhD Dissertation. Tianjin: Tianjin University, 2010. [in Chinese]
- [2] Xue, S.D., Gao, Z.Y. and Li, X.Y., "Research Status and Prospects of Cable Domes", *Applied Mechanics and Materials*, 2011, Vols. 94-96, pp. 1424-32.
- [3] Zhan, W.D. and Dong, S.L., "Advances in Cable Domes", *Journal of Zhejiang University*, 2004, Vol. 38, No. 10, pp. 1298-1307.
- [4] Masao, S. and Kurasiro, T., "A Study on Structural Behaviors of Beam String Structure", *Summaries of Technical Papers of Annual Meeting Architectural Institute of Japan*, Tokyo, Japan, 1985, Vol. B1, pp. 280-284.
- [5] Masao, S., "A Study on Structural Planning of Radial Type Beam String Structures", *Summaries of Technical Papers of Annual Meeting Architectural Institute of Japan*, Tokyo, Japan, 1988, Vol. B1, pp. 1365-1366.
- [6] Masao, S. and Ohtake, T., "A Study on Beam String Structure with Flat Circular Arch", *Summaries of Technical Papers of Annual Meeting Architectural Institute of Japan*, Tokyo, Japan, 1988, Vol. B1, pp. 1369-1374.
- [7] Masao, S. and Okasa, A., "The Role of String in Hybrid String Structure", *Engineering Structures* 1999, Vol. 21, No. 8, pp. 756-69.
- [8] Kawaguchi, M., Abe, M. and Hatato, T., et al., "On a Structure System "Suspen-dome"", *Proc. of IASS Symposium*, Istanbul, 1993, pp. 523-530.
- [9] Kawaguchi, M., Abe, M. and Tatemichi, I., "Design, Tests and Realization of "Suspen-dome" System", *Journal of the IASS*, 1999, Vol. 40, No. 131, pp. 179-192.
- [10] Chen, Z.H. and Qiao, W.T., "A New-style Cable Supported Structure System-Cable Supported Barrel Vault Structure System", *Proc. of APCS2009*, Nogoya, 2009, pp. 69-79.
- [11] Chen, Z.H., Qiao, W.T. and Yan, X.Y., "Cable Supported Barrel Vault Structure System and Research on Mechanics Characteristics", *International Journal of Advanced Steel Construction*, 2010, Vol. 6, No. 3, pp. 867-878.
- [12] Qiao, W.T. and Chen, Z.H., "Scale model test research on cable supported barrel vault structure", *Advanced Materials Research*, 2011, Vols. 163-167, pp. 465-470.
- [13] Qiao, W.T., Chen, Z.H. and Zhao, M.S., "Test study on basic static characteristics of cable supported barrel vault structure", *International Journal of Advanced Steel Construction*, 2012, Vol. 8, No. 2, pp. 199-211.
- [14] Chen, Z.H. and Qiao, W.T., "Analysis on Cable Supported Concrete Roof Structure and its Basic Characteristics", *Building Structure*, 2010, Vol. 40, No. 11, pp. 22-25. [in Chinese]
- [15] Qiao, W.T., Li, Y. and Deng, Y.Z., "Research on Mechanical features of Cable-supported Ribbed Beam Composite Slab Structure", *Proc. of the 14th Conference on Modern Structural Engineering*, Tianjin, China, 2014, pp. 328-332. [in Chinese]
- [16] Liu, Y.P. and Chan, S.L., "Second-order Analysis for Design of Glass-supporting and Pre-tensioned Trusses", *International Journal of Structural Stability and Dynamics*, 2009, Vol. 9, No. 3, pp. 489-510.
- [17] Li, Z.X., "Theory and Technique of Engineering Structure Experiments", TianJin: Tianjin University Press, 2004. [in Chinese]
- [18] "GB5009-2012: Load Code for the Design of Building Structures", Beijing: China Building Industry Press, 2012. [in Chinese]

NONLINEAR STABILITY ANALYSIS OF A RADIALLY RETRACTABLE SUSPEN-DOME

Jianguo Cai*, Yangqing Liu, Jian Feng and Yongming Tu

*Key Laboratory of C & PC Structures of Ministry of Education, National Prestress Engineering Research Center,
Southeast University, Nanjing 210096, China*

**(Corresponding author: E-mail: caijg_ren@hotmail.com; j.cai@seu.edu.cn)*

Received: 23 December 2015; Revised: 3 March 2016; Accepted: 26 May 2016

ABSTRACT: A radially retractable roof structure based on the concept of the suspen-dome is proposed in this paper. The radially foldable bar structure are strengthened by the lower cable-strut system. Then the buckling capacity of a radially retractable suspen-dome was investigated. The geometrically non-linear elastic buckling and elasto-plastic buckling analyses of the hybrid structure were carried out. Then the effects of different structural parameters, such as the rise-span ratio, beam section, area and pre-stress of lower cable-strut systems, on the failure load were investigated. The influence of imperfections on the elasto-plastic buckling loads was also discussed. The results show that the critical buckling load is reduced by taking account of material non-linearity. Furthermore, increasing the rise-to-span ratio or the cross-section area of steel beams notably improves the stability performance of the structure. However, the area and pre-stress of cable-strut systems pose small effect on the structural stability. It can also be found that the suspen-dome is highly imperfection sensitive and the reduction of the failure load due to imperfections is considerable.

Keywords: Retractable roof, suspen-dome, stability, elasto-plastic, failure load

DOI: 10.18057/IJASC.2017.13.2.2

1. INTRODUCTION

Retractable roof structures, which enable the users of recreational facilities to enjoy open air as long as allowed by the weather, are playing an important role in the development of multi-functional sports and culture facilities. With one or more degrees of freedom, deployable/foldable structures can expand to form a large opening space, which make them ideal for use as retractable roofs [1]. However, for a retractable roof, which is unlike a demountable, mobile, transportable or temporary structure, there is a permanent structure in a fixed location [2]. Within the boundaries given by this permanent structure, the retractable roof is capable of undergoing a geometric transformation between two distinct configurations, usually referred to as the open and closed configurations. In the past two decades, many concepts of deployable structures have been proposed for retractable roof structures [3]. Among these concepts, there is a new type of retractable structures which use angulated scissor-like elements, which is proposed by Hoberman [4-6], as basic structural elements. The unit, which consists of a pair of identical angulated rods connected by a revolute joint, subtends a constant angle as their rods rotate while maintain the end pivots on parallel lines [7]. Therefore, it can create a closed-loop mechanism, which is called Hoberman's Linkage. Then this concept was extended by You and Pellegrino [8] who gave birth to a more general family of such structures called the foldable bar structures. On the other hand, they stated that the Hoberman's linkage can be extended by the addition of a pair of bars, connected to one another and to the base linkage by scissor hinges. The resulting structure will be deployable, like the original Hoberman's linkage, provided that the members added to it are not collinear. Repeating the same argument it can be shown that any number of pairs of bars connected by hinges to the base structure will leave its mobility unchanged. That is to say, a foldable structure, as shown in Figure 1, can be made from multi-angulated rods similar to the angulated scissor-like elements introduced in Hoberman's linkage.

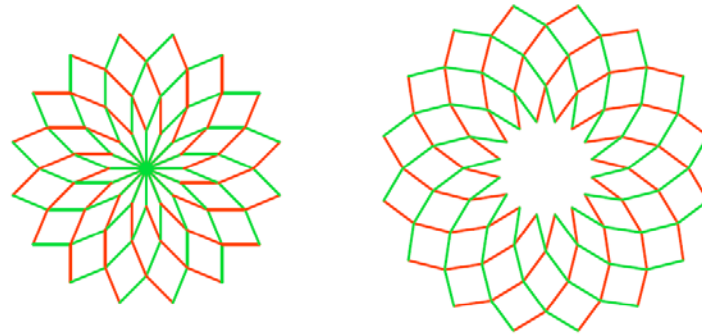


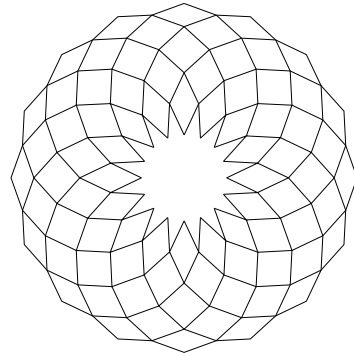
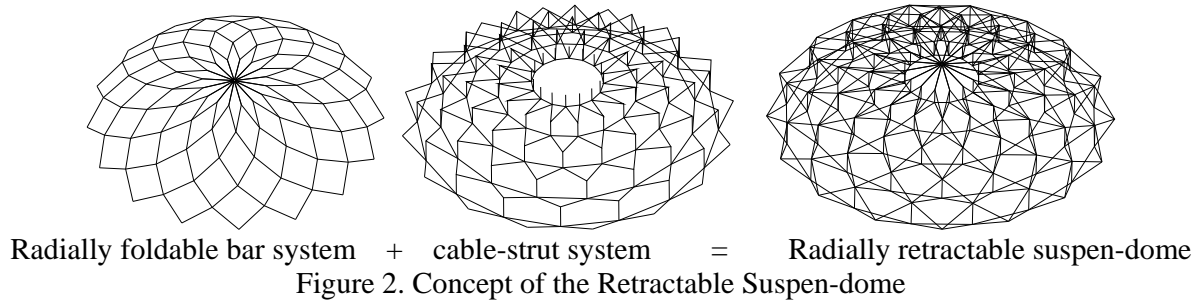
Figure 1. Foldable Bar Structures

However, if this foldable bar structures is used as a retractable roof structure, Teall [9] found that the deformation of the structure, even for a three layer foldable bar structure with a span of 2 m, was quite large under self-weight. This leads to the problem of too small stiffness of the structure to resist the external loads. Mao and Luo [1] and Cai et al. [10] also pointed out that the foldable bar structures are not suitable for the retractable roof structure. They also give some comments and suggestions on how to increase the structural stiffness. However, the stability of the single-layer lattice dome is relatively low when the required span is long [11]. To solve this program, many attempts have been made at increasing flexural stiffness by the use of multiple steel-truss layers. The double-layer dome is advantageous since it has relatively high stability. There is still room for improvement; however, because large weights of the dome cause considerable tension in the outer ring girders. To achieve high stability of single-layer dome and at the same time reduce the burden on boundary structures, the suspen-dome system was developed by Kawaguchi et al [12, 13]. The suspen-dome system has been widely used. Moreover, static and dynamic analysis and tests of the suspen-dome have been carried out by many researchers [14-22].

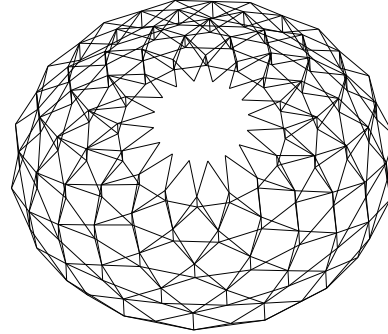
To advance the practical application of the foldable bar structure in long-span retractable roofs, the concept of suspen-dome is introduced into the foldable bar system. Then a retractable suspen-dome is obtained. This paper shows how to perform a geometrical and material nonlinear finite element analysis by using ANSYS to investigate the stability of the suspen-dome in the closed position. Additionally, the effect of factors such as the geometrical and structural parameters and the asymmetrical distribution of loads will also be taken into consideration in this paper. The imperfection sensitivity including the pattern and scale will be investigated.

2. STRUCTURAL SYSTEM

This paper replaces the upper single-layer lattice shell of the suspen-dome by the radially foldable bar system, forming the radially retractable roof structure as shown in Figure 2. It can be found that the suspen-dome has two parts, one is the upper radially foldable bar system and the other is the lower cable-strut system. During the deployment process, the structure unfolds gradually with the radial movement of the boundary joints of the upper foldable bar structures, which is shown in Figure 3. Meanwhile radial cables of the lower cable-strut structure are slack while the length of hoop cables increases continually. Then during the close of the system, hoop cables can be regarded as active cables and radial cables as passive cables. When the structure is totally closed, the lower cable-strut system will have prestresses if we keep tensioning active cables, which is similar to the prestress construction of the general suspen-dome. It can be found that during both the open and close process, the lower cable-strut system is in slackness and only the upper single-layer lattice shell resists external loads. Only the totally closing of the structure will leads to the upper single-layer lattice shell work together with the lower cable-strut system to form a suspen-dome structure.



(a) Radially foldable bar system



(b) Radially retractable suspen-dome

Figure 3. Radially Retractable System during the Motion

3. STABILITY BEHAVIOR OF THE RADIALLY RETRACTABLE SUSPEN-DOME

3.1 Finite Element Model

An example of the retractable suspen-dome shown in Figure 4 will be studied in this paper. In this model, every multi-angulated beam has six segments. And the inclined angle between adjacent segments of the beam is 157.5° . The span of the grid shell is 38 m with the rise-to-span ratio of 0.2. Other geometric parameters are given in Figure 5.

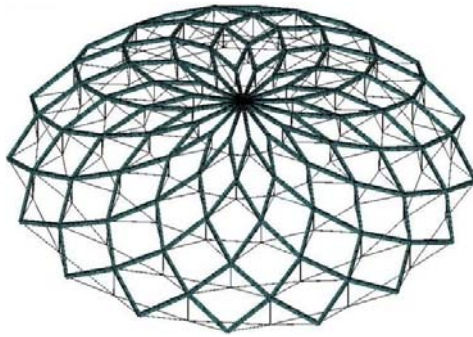


Figure 4. 3D Retractable Suspen-dome in the Closed Configuration

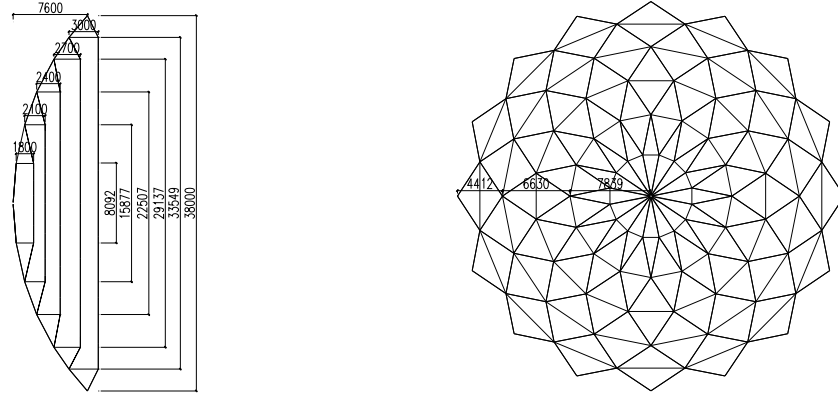


Figure 5. Geometric Parameters of the Retractable Suspended-dome (mm)

The symmetrical load case $g+s$ (dead load +snow load) and asymmetrical load case $g+s/2$ ($s/2$ —snow load distributed over half of the span) will be taken into account in all the following computations. The dead load g consists of a self-weight of 0.5 kN/m^2 including all the beams and cables. The snow load is applied to the top surface of the structure in the vertical direction with a magnitude of 0.5 kN/m^2 .

In this paper, the finite element software ANSYS is used to analyze the structure and the geometric nonlinearity is fully considered. The angulated beams are simulated by BEAM188. Joints of these multi-angulated rods are pinned with the release of rotational degree of freedom and the boundary of the retractable suspended-dome is fixed circularly. Members of multi-angulated beams adopt the box beam with Q345B steel, with dimensions of cross section $300\text{mm} \times 200\text{mm} \times 10\text{mm}$ (height \times width \times wall thickness). Additionally, the cross section area of the cable, which is simulated by tension-only bar element LINK10, is 78.5 mm^2 . The cross-section area of struts, which is simulated by LINK8, is 706.5 mm^2 . The Young's modulus of steel beams, struts and cables are 210 MPa, 210 MPa and 180 MPa, respectively.

3.2 Distribution of Initial Prestress Level of Lower Cable-strut System

In order to resist external loads and prevent the loose of cables, enough vertical forces must be provided by the initial prestress in cables. As stated by Kitipornchai et al. [8], the suspended-dome system is very rigid, and the nonlinear deformation is very small even under a large external load. As a result, the method of superposition can be applied in the analysis of the distribution of initial prestress level without introducing a large degree of error. Then the suspended-dome structure is divided into two parts: the top single-layer dome and the lower cable-strut system. We add the restrictions to the lower cable-strut system for the force finding analysis.

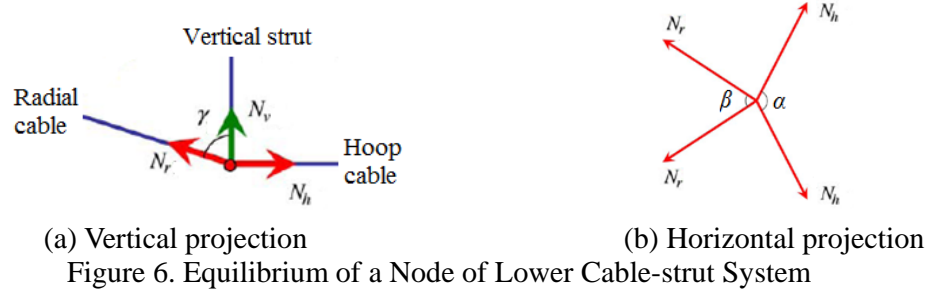
The number of independent inextensional mechanisms is five and the number of independent states of self-stress is also five. The lower cable-strut system have five independent rings after adding the restrictions, so the independent state of self-stress should be the stress distribution of every ring respectively. Because of the symmetry of the structure, there are three types of elements in every state of self-stress: radial cables, hoop cables and vertical struts. From the equilibrium of every nodes of the lower cable-strut system as shown in Figure 6, we can obtain the relationship between the forces of hoop cables, vertical struts and radial cables. It can be seen from Figure 6 that the relation between the hoop cable forces N_h and radial cable forces N_r is

$$N_r \sin \gamma \cos \frac{\beta}{2} = N_h \cos \frac{\alpha}{2} \quad (1)$$

where α denotes the angle between adjacent hoop cables, β denotes the horizontal projection of the angle between adjacent radial cables, γ denotes the angle between the radial cable and the vertical axis. Moreover, the forces relation between the vertical struts N_v and radial cables N_r can be given as

$$N_v = 2N_r \cos \gamma \quad (2)$$

Therefore, the state of self-stress of every ring of lower cable-strut system can be obtained from Eqs. 1 and 2.



The lower structure is divided into five independent sub-structures, thus the force distribution is not affected by other rings. The combination factor of five independent states of self-stress must be determined by other condition. The optimization theory is used in this paper to decide the combination factor.

Step 1 The nodal displacement of all nodes of single-layer dome under dead load can be assembled in the vector d_{sl} .

Step 2 The nodal displacement of all nodes of single-layer dome related to the state of self-stress of lower cable-strut system can be assembled in the vector $d_i (i=1, \dots, s)$.

Step 3 Supposed the combination factor of every independent state of self-stress is $\alpha_i (i=1, \dots, s)$. Then, the nodal displacements of all nodes of single-layer dome is d , can be written

$$d = \sum_{i=1}^s \alpha_i d_i + d_{sl} = \begin{bmatrix} d_1 & d_2 & \dots & d_s \end{bmatrix} \begin{Bmatrix} \alpha_1 \\ \alpha_2 \\ \vdots \\ \alpha_s \end{Bmatrix} + d_{sl} \quad (3)$$

The objective function is

$$\min. \quad \psi(\alpha_i) = \|d\|, \quad i=1 \sim s \quad (4)$$

Then we can obtain the initial prestress in hoop cables from the outer ring to the inner ring are 100MPa, 68.08 MP, 38.47 MPa, 15.67 MP, 3.25 MPa, respectively.

3.3 Stability Behavior

The influence of the material nonlinearity on the stability of single-layer lattice shell or gird shell structures is significant [23]. Moreover, the model containing only geometry nonlinearity will over estimate the failure load of the structure. As to the radially retractable suspen-dome, a new type structure form, the influence of material nonlinearity is still unclear. Therefore, the model considering geometry nonlinear only (Model 1) and the model considering both geometry and material nonlinearity (Model 2) are investigated.

Moreover, the stability behaviors of the radially retractable suspen-dome and the corresponding single-layer grid shell are studied to investigate the effects of lower cable-strut system. The load displacement curves for the node with the maximum vertical displacement are given in Figs. 7 and 8. The load factor is defined as the ratio between the applied load and the design load. Under the symmetric load case (load 1) and the anti-symmetric load case (load 2), the failure load of the radially retractable suspen-dome considering only geometry nonlinearity is larger than that the system considering both geometry and material nonlinearity, i.e. 9.49% higher in load 1 and 14.63% higher in load 2. Therefore, the model considering geometry nonlinearity only leads to a relatively unsafe result and both geometry and material nonlinearity need to be considered in the analysis of the structure.

In addition, it can be found that under both load cases, the first half parts of load displacement curves of the two models are overlapped. It indicates that the influence of the material nonlinearity at the beginning of the loading process is slight. With the increase of the loading, the structure shows plastic behavior. Then the slope of the load displacement curve decreases remarkably and the ultimate capacity drops greatly for the elasto-plastic buckling analysis. For the elasto-plastic failure loads of the two modes, the suspen-dome increases by 146.91% and 10.05% than the corresponding grid shell under the load 1 and the load 2, respectively.

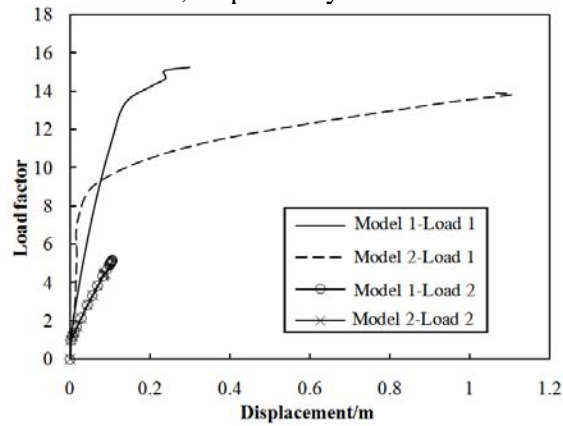


Figure 7. Load Displacement Curve of the Retractable Suspen-dome

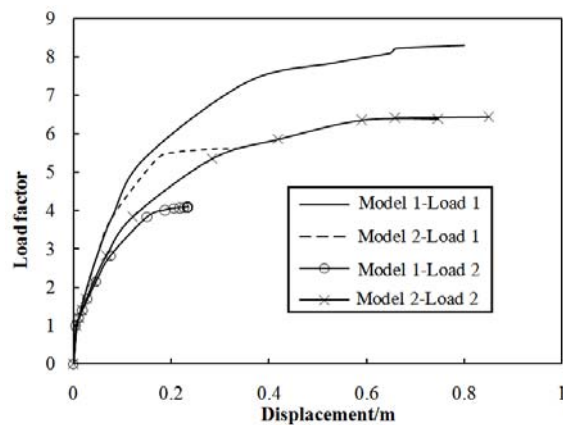


Figure 8. Load Displacement Curve of the Corresponding Single-layer Grid Shell

4. PARAMETRIC STUDIES

In order to better understand the influence of each parameter of the radially retractable suspen-dome on the elasto-plastic ultimate capacity of the structure, effects of the rise-span ratios, steel beams sections, initial cable prestress, cable areas are investigated in this paper.

4.1 Influence of Rise-span Ratios

The elasto-plastic analyses as for the example structure were carried out with different rises (keeping the span constant) to study the effect of rise-span ratios. The rise-to-span ratios correspond to 0.1, 0.15, 0.2 and 0.25, respectively. The load displacement curves of the suspen-dome with different rise-span ratios and the corresponding failure load factors are shown in Figure 9. It can be found that the rise-span ratio has a great influence on the stability behavior of the hybrid grid shell and the failure load increases with the increase of the rise-span ratio. It can be concluded that the rise-span ratio is a key factor of the stability capability of the hybrid grid shell.

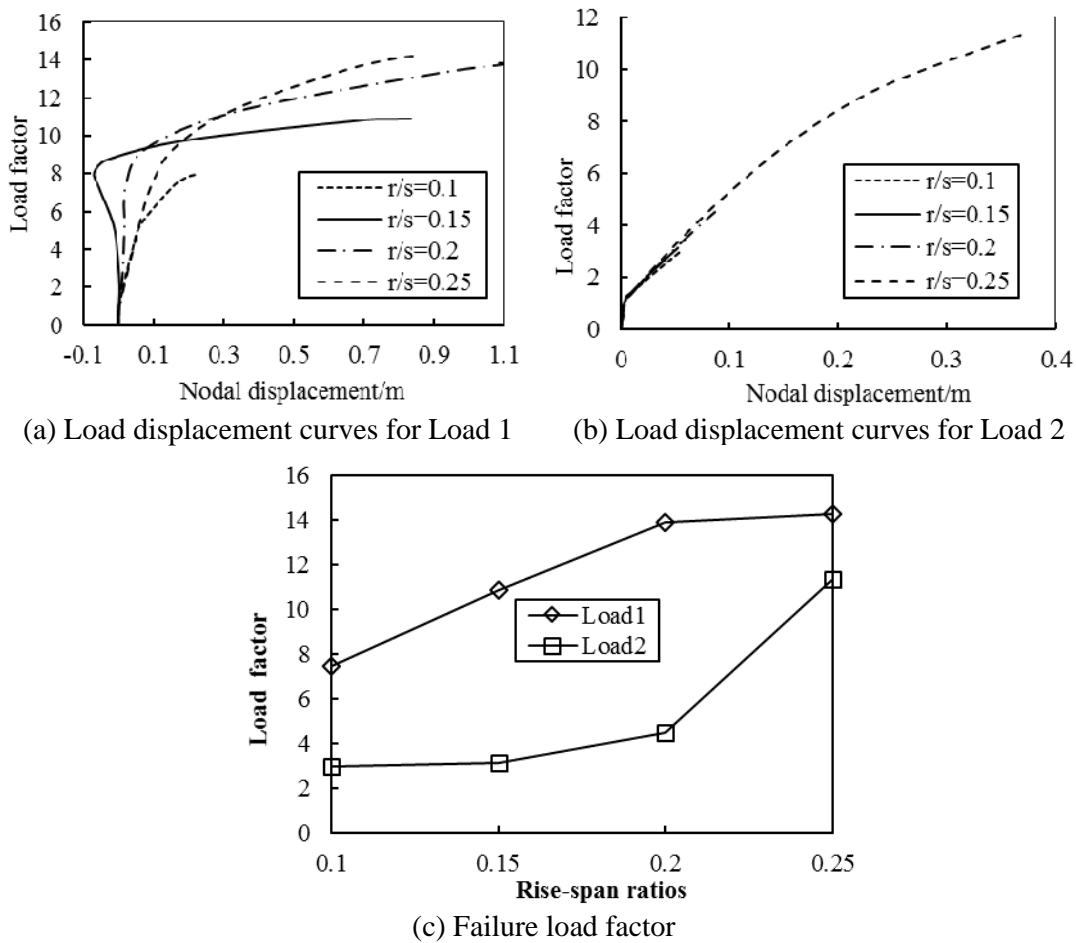
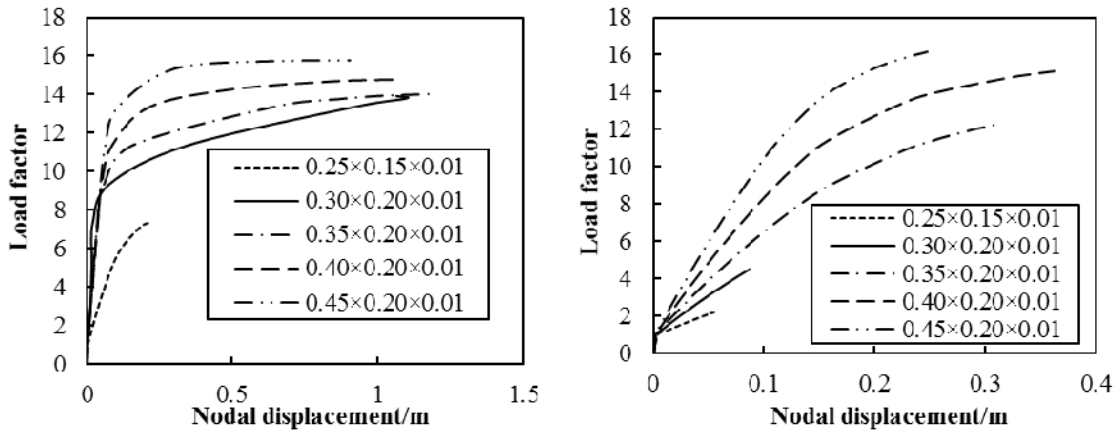


Figure 9. Influence of Rise-span Ratio

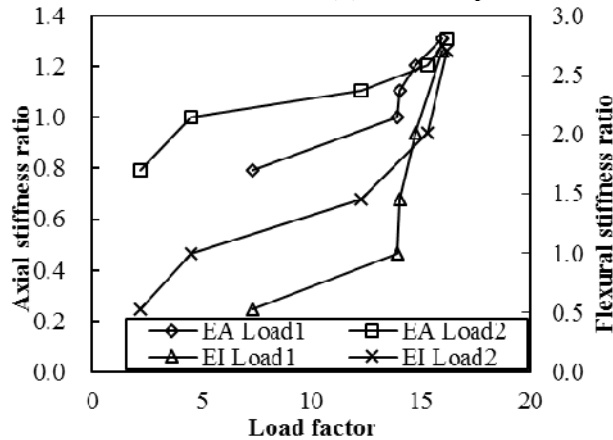
4.2 Influence of the Steel Beam Section

When the geometry of the structure is identified, the cross-section of steel beams can be an important factor that affects the buckling capacity of the suspen-dome. This is because the stiffness of the single-layer grid shell mostly relies on the stiffness of beams, which mainly includes the beam axial stiffness EA and flexural stiffness EI . Regarding the beam rigidity of the basic model as E_0A_0 and E_0I_0 , the stability behavior of the structure is investigated by changing the beam stiffness coefficients EA/E_0A_0 and EI/E_0I_0 .

Five different steel beams sections, $250\text{mm}\times150\text{mm}\times10\text{mm}$, $300\text{mm}\times200\text{mm}\times10\text{mm}$, $350\text{mm}\times200\text{mm}\times10\text{mm}$, $400\text{mm}\times200\text{mm}\times10\text{mm}$, $450\text{mm}\times200\text{mm}\times10\text{mm}$, are chosen to study the influence of beam sections. The load displacement curves are given in Figure 10. It shows that the tendency of load displacement curves is consistent for different beam sections. It can also be found that the failure load factor of the suspen-dome improves with the rise of the bar stiffness. For the symmetric load case, the failure load drops 47.25% when the axial stiffness of bars decreases by 20% and it increases by 14.75% when the flexural stiffness is raised by 30%. For the anti-symmetric load case, the failure load drops 51.67% when the axial stiffness decreases by 20% and it increases by 258.84% when the flexural stiffness is raised by 30%. Meanwhile, the load displacement curves can reveal the characteristic of the structural stiffness. It can be obtained from Figure 10 that the increase of beam sections will enhance the structural stiffness of the hybrid grid shell.



(a) Load displacement curve under Load 1 (b) Load displacement curve under Load 2



(c) Failure load factor

Figure 10. Influence of the Steel Beam Sections

4.3 Influence of Hoop and Radial Cable Areas

The area of hoop and radial cables may also be important factors that affect the elasto-plastic buckling behavior of the retractable hybrid grid shell. The load displacement curves and the failure load against the area of hoop cables are shown in Figure 11. The diameters of hoop cables correspond to 8 mm, 10 mm, 12 mm, 15 mm and 20 mm in Figure 11, respectively. In Figure 11(c), the horizontal coordinate is the cable area ratio, m , which is defined as the ratio of cable areas to the cable area of the basic model. It can be found from Figure 11 that, for both load cases, the failure load factor rises first and then decrease with the increase of the hoop cable area. The load displacement curves also show that the effect of the cable area on the structural stiffness is positive first and then negative. However, it can also be found that the hoop cable area has a limited influence on the ultimate capacity of the suspen-dome. Hence, it is not economical to increase the hoop cable area to improve the structure stability behavior.

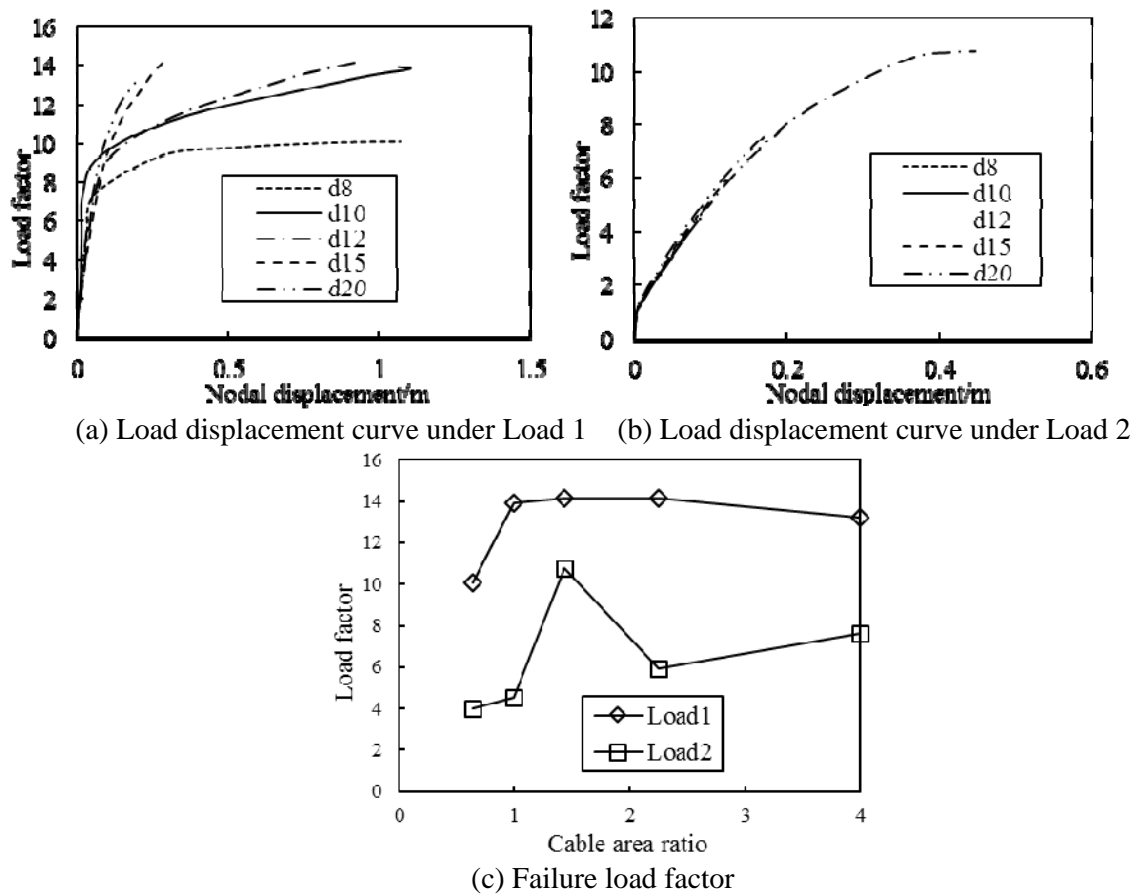


Figure 11. Influence of the Hoop Cable Section

The load displacement curves and the failure load against the area of radial cables are shown in Figure 12. The diameters of radial cables correspond to 8 mm, 10 mm, 12 mm, 15 mm and 20 mm in Figure 12, respectively. It can be found from Figure 12 that, for the symmetric load case, the failure load factor rises with the increase of the radial cable area. However, for the asymmetric load case, the failure load decrease with the increase of the radial cable area. Moreover, it can also be found that the radial cable area has a limited influence on the ultimate capacity of the suspen-dome.

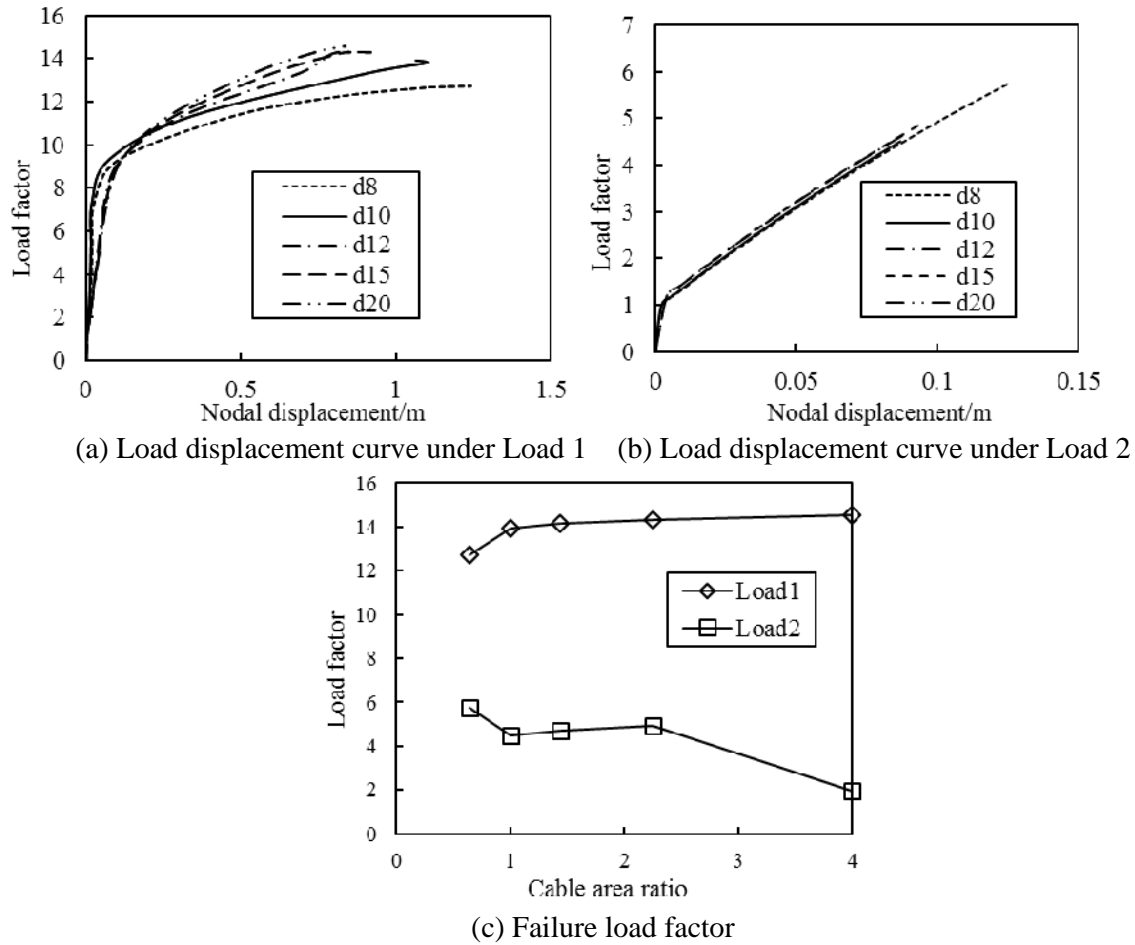


Figure 12. Influence of the Radial Cable Section

4.4 Influence of Cable-strut Prestress Levels

To study the effect of cable-strut pre-stress levels, the initial stresses of hoop cables in the outer ring are set to 0 MPa, 50 MPa, 100 MPa, 150 MPa and 200 MPa, respectively. The initial stresses of other cables and struts can be obtained with the method given in Section 3.2. The results under both load cases are shown in Figure 13. It can be seen from Figure 13 that the ultimate capacity of the suspen-dome enhances with the increase of the initial pre-stress level, but the rate of the increase is slight. The ultimate load just increases 0.29% when the prestress level doubles, and it just decreases by 0.36% when the prestress level is reduced to the half. It can be concluded that the cable-strut pre-stress contributes little to the ultimate capacity of the structure. Therefore, it is not a wise choice to improve the ultimate capacity of the structure by increasing the initial prestress in lower cable-strut system only.

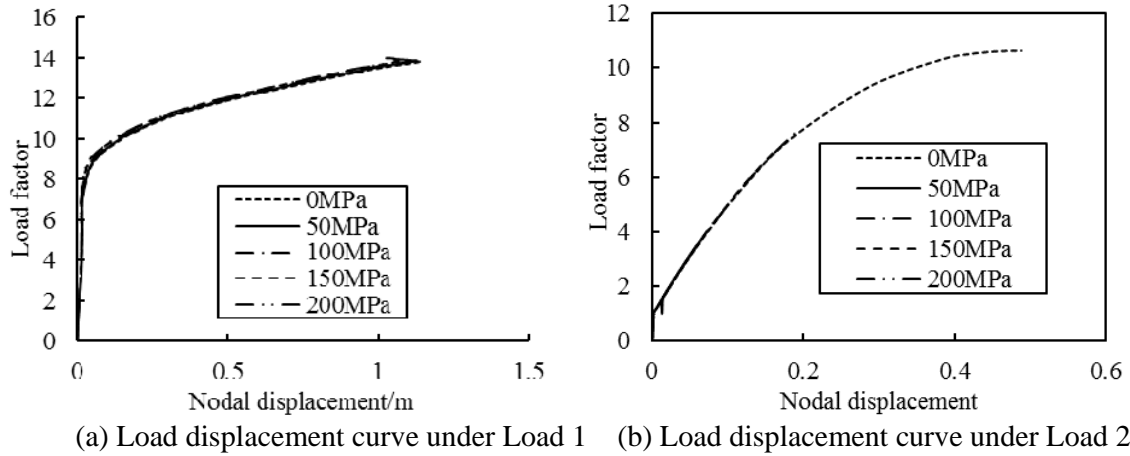


Figure 13. Influence of Cable-strut Prestress Levels

4.5 Influence of Strut Sections

Different strut sections with diameters of 20 mm, 25 mm, 30 mm, 35 mm and 40 mm are adopted to conduct the stability analysis of the structure. Figure 14 shows the influence of the strut section on the elastoplastic ultimate capacity of the suspen-dome. It can be seen from this figure that the load displacement curves are nearly overlapped, which indicates none influence of the strut section on the elastoplastic ultimate capacity. Thus, when choosing the strut section, only its own stability needs to be considered.

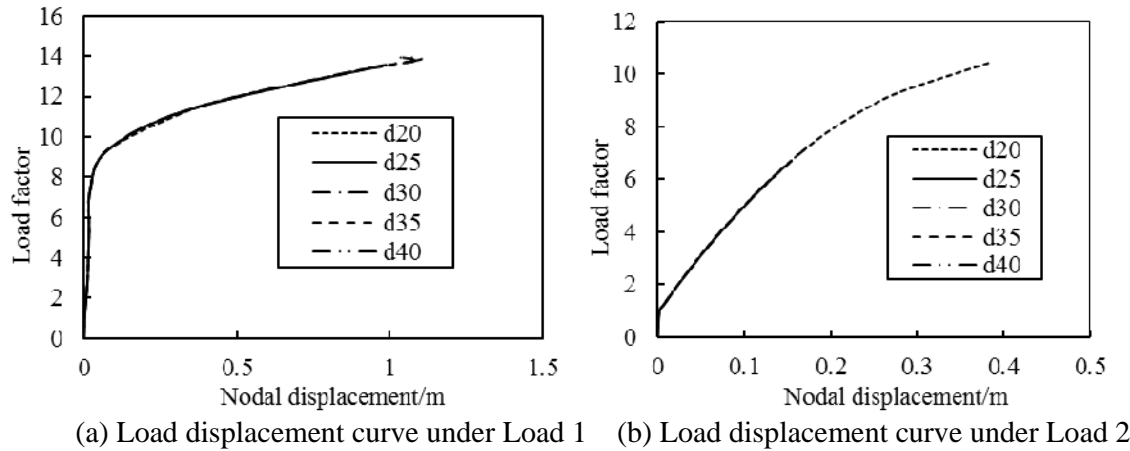


Figure 14. Influence of Strut Sections

5. EFFECTS OF IMPERFECTIONS ON THE STABILITY BEHAVIOR

For the long-span spatial structures, the inaccuracy in construction and installation may trigger a great influence on the forces of the structure. The single-layer grid shell structure is sensitive to imperfections [24, 25]. As a new type of single-layer grid shell, the effect of imperfections on the stability of the radially retractable hybrid grid shell has not been studied. According to the European standard [26] and Chinese code [27], the geometrical imperfection should be taken into account in the non-linear analysis in order to model the structure in a realistic way.

Several methods are available to analyze geometrical imperfections, i.e. the random imperfection mode method [28], the consistent imperfection mode method. In the later method, the imperfection distribution is assumed to be consistent with the deflected shapes, such as eigenvalue buckling

modes and nonlinear buckling shapes. The consistent imperfection mode method is used in this paper. The steps of the imperfect buckling analysis can be concluded as following:

- (1) Conducting the eigenvalue buckling analysis or nonlinear buckling analysis of the structure to obtain its buckling modes;
- (2) Normalizing the buckling modes deriving from the eigenvalue buckling analysis or nonlinear buckling analysis;
- (3) Modifying the joint coordinates of the finite model according to the previous step;
- (4) Conducting the static elastoplastic analysis of the imperfect structure to obtain its ultimate capacity.

As suggested in Cai et al. [24, 25], we have set up the following shapes of imperfections for hybrid grid shell: (1) the first four eigenvalue buckling modes; (2) the displacement shape of the loaded structure obtained from a geometrical non-linear elastic buckling analysis. Both imperfections are easy to compute and therefore can be often used by engineers. The first four eigenvalue buckling modes and the nonlinear buckling mode of the hybrid grid shell under both load cases are given in Figure 15.

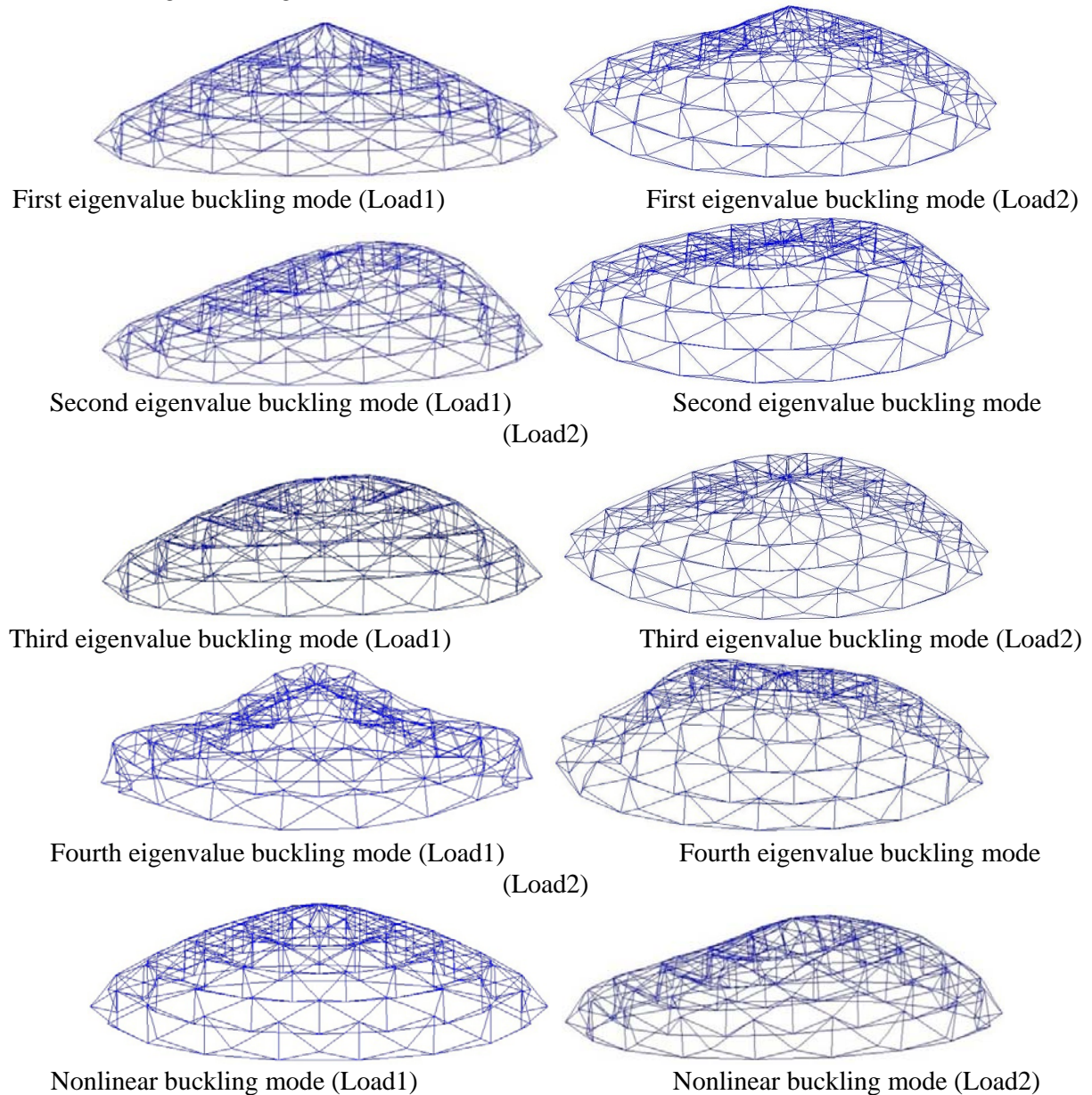


Figure 15. Buckling Modes of the Radially Retractable Suspen-dome

Figure 16 show the failure load factors for different suspen-dome, including the perfect structure. The maximum imperfections of all shapes have been scaled to $\text{span}/300$. It is clear from the figure that the failure load of the hybrid structure under both load cases is significantly affect by the geometric imperfections. It can be found that the lowest buckling load is predicted with the nonlinear buckling mode. Therefore, this imperfection shape is thus employed in all the following analyses.

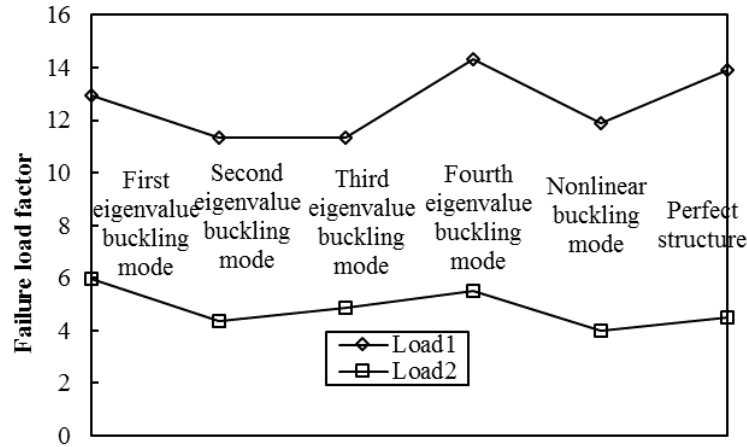


Figure 16. Influence of Imperfection Modes on the Failure Load of Suspen-domes

6. CONCLUSIONS

The buckling capacity of the radially suspen-dome was investigated in this paper. The geometrical non-linear elastic buckling analyses was carried out first. By taking into consideration of material non-linearity using elasto-plastic analyses, the behavior of hybrid structures was found significantly different. The results show that the buckling capacity is reduced by taking account of material non-linearity. Then the effects of different geometrical and parameters on the failure loads were studied. The analysis results show that under a particular span, the buckling capacity increases with the increase of the rise-span ratio. Moreover, increasing the cross-section of steel beams notably improves the stability performance of the structure. However, the section area and pre-stress of lower cable-strut system pose virtually little effect on the structural stability. Finally, the effects of imperfections on the stability behavior were also investigated. It can be found that radially retractable suspen-dome is highly imperfection sensitive and the reduction of the failure load due to imperfections can be considerable. Furthermore, when imposing imperfections, the proper shape is also important. The results show that the nonlinear buckling mode is the most critical imperfection shape.

ACKNOWLEDGEMENTS

The work presented in this article was supported by the National Natural Science Foundation of China (Grant No. 51308106 and No. 51578133), a Project Funded by the Priority Academic Program Development of Jiangsu Higher Education Institutions, and the Excellent Young Teachers Program of Southeast University.

REFERENCES

- [1] Mao, Decan and Luo, Yaozhi, "Analysis and Design of a Type of Retractable Roof Structure", *Advances in Structural Engineering*, Vol. 11, No. 4, pp. 343-354.
- [2] Van, Mele T, De, Temmerman N, De, Laet L. and Mollaert, M., "Scissor-hinged Retractable Membrane Structures", *Int. J. Structural Engineering*, 2010, Vol. 1, No. 3/4, pp. 374-396.
- [3] De, Temmerman N., Alegria, Mira L. and Vergauwen, A., "Feasibility of the Universal Scissor Component (USC): Building a Full-scale Deployable Dome", *Journal of the International Association for Shell and Spatial Structures*, 2012, Vol. 53, No. 4, pp. 227 – 236.
- [4] Hoberman, C., "Reversibly Expandable Doubly-curved Truss Structures", US Patent 4, 942,700, 1990.
- [5] Hoberman, C., Radial Expansion Retraction Truss Structure", US Patent Vol. 5,024,031, 1991.
- [6] Hoberman, C., "Art and Science of Folding Structures", *Sites*, Vol. 24: pp. 61-69, 1992.
- [7] Cai, J.G., Xu, Y.X. and Feng, J., "Kinematic Analysis of Hoberman's Linkages with the Screw Theory", *Mechanism and Machine Theory*, 2013, Vol. 63, pp. 28-34.
- [8] You, Z. and Pellegrino, S., "Foldable Bar Structures", *International Journal of Solids and Structures*, 1997, Vol. 34, No. 15, pp. 1825-1847.
- [9] Teall, M.J., Deployable Roof Structures. Masters Dissertation, University of Cambridge, UK, 1996.
- [10] Cai, J.G., Jiang, C., Deng, X.W., etc., "Static Analysis of a Radially Retractable Hybrid Grid Shell in the Closed Position", *Steel and Composite Structures*, 2015, Vol. 18, No. 6, pp. 1391-1404.
- [11] Abedi, K. and Parke, G.A.R., "Progressive Collapse of Single-layer Braced Domes", *International Journal of Space Structures*, 1996, Vol. 11, No. 3, pp. 291-306.
- [12] Kawaguchi, M., Abe, M. and Tatemichi, I., "Design, Tests and Realization of Suspend-dome System", *Journal of International Association of Shell and Spatial Structures*, 1999, Vol. 40, No. 131, pp. 179-192.
- [13] Kawaguchi, M., Abe, M., Hatato, T., et al., "Structural Tests on the "Suspen-dome" System", In: *Proceedings of the IASS symposium*. Atlanta, USA, 1994.
- [14] Kang, W.J., Chen, Z.H., Lam, H., et al., "Analysis and Design of the General and Outmost-ring Stiffened Suspen-dome Structures", *Engineering Structures*, 2003, Vol. 25, No. 13, pp. 1685-1695.
- [15] Kitipornchai, S., Kang, W.J., Lam, H., et al., "Factors Affecting the Design and Construction of Lamella Suspend-dome Systems", *Journal of Construction Steel Research*, 2005, Vol. 61, No. 6, pp. 764-785.
- [16] Li, K.N. and Huang, D.H., "Static Behavior of Kiewitt6 Suspendome", *Structural Engineering and Mechanics*, 2011, Vol. 37, No. 3, pp. 309-320.
- [17] Liu, H.B., Chen, Z.H. and Zhou, T., "Research on the Process of Pre-Stressing Construction of Suspen-Dome Considering Temperature Effect", *Advances in Structural Engineering*, 2012, Vol. 15, No. 3, pp. 489-493.

- [18] Li, Z.Q., Zhang, Z.H., Dong, S.L., et al., "Construction Sequence Simulation of a Practical Suspen-dome in Jinan Olympic Center", *Advanced Steel Construction*, 2012, Vol. 8, No. 1, pp. 38-53.
- [19] Chen, Z.H., Wu, Y.J., Yin, Y., et al., "Formulation and Application of Multi-node Sliding Cable Element for the Analysis of Suspen-Dome Structures", *Finite Elements in Analysis and Design*, 2010, Vol. 46, No. 9, pp. 743-750
- [20] Liu, H.B., Han, Q.H., Chen, Z.H., et al. "Precision Control Method for Prestressing Construction of Suspen-dome Structures", *Advanced Steel Construction*, 2014, Vol. 10, No. 4, pp. 404-425
- [21] Guo J.M., Yuan X.F., Li Y.Y., et al., "A Simple Approach for Force Finding Analysis of Suspended-Domes Based on the Superposition Principle", *Advances in Structural Engineering*, 2014, Vol. 17, No. 11, pp. 1681-1691.
- [22] Zhou, Z., Feng, Y.L., Meng, S.P., et al., "A Novel form Analysis Method Considering Pretension Process for Suspen-dome Structures", *KSCE Journal of Civil Engineering*, 2014, Vol. 18, No. 5, pp. 1411-1420.
- [23] Fan, F., Cao, Z.G. and Shen, S.Z., "Elasto-plastic Stability of Single-layer Reticulated Shells", *Thin-Walled Structures*, 2010, Vol. 48, No. 10-11, pp. 827-836.
- [24] Cai, J.G., Gu, L.M., Xu, Y.X., Feng, J. and Zhang, J., "Nonlinear Stability of a Single-layer Hybrid Grid Shell", *Journal of Civil Engineering and Management*, 2012, Vol. 18, No. 5, pp. 752-760.
- [25] Cai, J.G., Zhou, Y., Xu, Y.X. and Feng, J., "Non-linear Stability Analysis of a Hybrid Barrel Vault Roof, Steel and Composite Structures", 2013, Vol. 14, No. 6, pp. 571-586.
- [26] Eurocode 2003, European Standard. 3: Design of Steel Structures, Parts 1–6: Strength and Stability of Shell Structures, European Committee for Standardisation, 2004.
- [27] JGJ7-2010, Technical Specification for Space Frame Structures, Beijing: China Architecture Industry Press [in Chinese], 2010.
- [28] Yamada, S., Takeuchi, A., Tada, Y. and Tsutsumi, K., "Imperfection-sensitive Overall Buckling of Single-layer Lattice Domes", *J. Eng Mech*, 2001, Vol. 4, pp. 382-396.

INTEGRATED FIRE-STRUCTURE SIMULATION OF A LOCALIZED FIRE TEST ON A CEILING STEEL BEAM

Guo-Qiang Li ^{1,2} and Chao Zhang ^{2,*}

¹ State Key Laboratory for Disaster Reduction in Civil Engineering, Tongji University, China

² College of Civil Engineering, Tongji University, China

*(Corresponding author: E-mail: 08_chao_zhang@tongji.edu.cn)

Received: 5 May 2016; Revised: 24 June 2016; Accepted: 1 July 2016

ABSTRACT: Performance based method is increasingly used for structural fire safety design of modern buildings with large enclosure. The design fire scenarios in large enclosure are localized fires. Integrated fire-structure simulation method is required to accurately predict the response of structures in realistic fires (e.g. localized fires). In recent years, there is an increase in use of FDS (Fire Dynamics Simulator) – FEM (finite element method) approach for performance-based structural fire design. This paper discusses the FDS-FEM approach for predicting the thermal response of structures subjected to localized fires. A fire-structure interface, named adiabatic surface temperature (*AST*), was applied to transfer data from FDS to ANSYS. By comparing the predicted and measured heat fluxes and steel temperatures of a steel ceiling beam exposed to a localized fire condition, the FDS-FEM method was tested. The FDS predicted heat fluxes matched well with the test data. The difference between the predicted and measured maximum heat fluxes was within 6% for the investigated two cases. The FDS-FEM method gave good prediction of the steel temperatures. The over-prediction of maximum steel temperature was within 11% for the investigated case. The methods described in this study provide a feasible way to study the complex behavior of structures in realistic fires.

Keywords: Integrated fire-structure simulation, Fire Dynamics Simulation (FDS), Finite element method (FEM), Localized fire, Steel ceiling beam, Performance based design, Temperature

DOI: 10.18057/IJASC.2017.13.2.3

1. INTRODUCTION

At high temperature nearly all structural materials lose some of their strength and stiffness. Structural steel retains only about half of its room temperature yield strength and elastic modulus at about 550 °C [1]. Temperature induced thermal strain, if restrained, generates additional stress in structures which might accelerate structure failure in fire. Because steel has high conductivity and low heat capacity, when exposed to fire the bare steel structures elevate to a high temperature in a short time which might result in structure collapse before complete evacuation of the building. Bare steel structures' frangible to fire has been investigated in many disastrous fire accidents, typically the WTC fire [2] and the Windsor Tower fire [3]. Therefore, comparing with other structures such as concrete structures and masonry structures, the fire safety of steel structures is of primary importance.

Traditionally, the fire safety of steel structures is insured by requiring the structural steel components have sufficient fire resistance. The fire resistance of a building component is determined by a standard fire resistance test conducted on an isolated member subjected to a specified time temperature curve. The standard fire resistance test, which was developed more than a century ago, has been criticized for its shortcomings [4]:

- The standard temperature-time curve is not representative of a real fire in a real building. A real fire includes both heating and cooling phases while the standard fire curve does not decrease with time. Also, the standard fire represents a uniform heating condition while the heating condition in a real fire is non-uniform, e.g. gas temperature distribution in localized fires in large enclosure is highly non-uniform spatially [5].

- The behaviour of the isolated members cannot represent the behaviour of the components in an entire structure. In a real building, a component is restrained by the surrounding structures. The restraints induce thermal stress in the heated component and also might activate alternative load-bearing modes (e.g., membrane action of composite floor slab [6, 7] and catenary action of restrained beams [8, 9]). Furthermore, there exist alternative load paths in restrained components. In entire structures, when some structural components begin to fail, the adjacent components will restrain to resist the further failure of the weakened components.

As a result, the design approach based on the standard fire cannot assess the actual level of safety of a structure exposed to fire and usually yields a fire protection design that is too conservative, which has been proved by both accident fires (e.g. the Broadgate Phase 8 fire [10]) and real fire tests (e.g. the Cardington full-scale fire test [11]). It should be noted, however, that a fire protection design based on a standard fire test or prescriptive code is not guaranteed to be conservative, as being found by recent numerical studies [12-15].

Over the past 30 years, there have been significant advances in structural fire research. New insights, data, and calculation methods have been reported, which form the basis for modern performance-based (PB) codes for structural fire safety [16]. The PB approach involves the assessment of the structural response in real fires and, therefore, requires advanced computational approaches for fire and structural modeling. Sophisticated computational fluid dynamics (CFD) models are typically used to simulate realistic fires [5], while finite element method (FEM) codes are mostly used for structural modeling [12-15, 17]. An integrated CFD-FEM simulation approach is needed for advanced structural fire analysis [18]. Fire Dynamics Simulator (FDS) is an open source CFD code, developed by NIST [19]. It has been widely used in fire engineering for modeling the gas phase environment (temperature, heat flux, velocity, species concentrations, etc.) in fires. Recently, there has been increased research in the application of FDS for structural fire analysis [20, 21]. Fire-structure interface tools for transferring data from FDS to particular FEM codes (such as ANSYS, ABAQUS, SAFIR) have been developed [21]. Although the FDS-FEM simulation approach has been used in practical projects [22, 23], validation of the integrated fire-structure simulation method is quite limited [24]. This paper presents a validation study of the integrated FDS-FEM simulation methodology against a localized fire test on a steel ceiling I beam reported by Hasemi et al. [25, 26]. This localized fire test was selected for model validation because of the applicability to real-world thermal conditions and because the test was well controlled (e.g. the heat release rate of the fire was controlled by computer), and detailedly measured.

2. INTEGRATED FIRE-STRUCTURE SIMULATION METHODOLOGY

2.1 The CFD-FEM Approach

Figure 1 illustrates the CFD-FEM simulation approach for structural fire analysis. The fire-structure interaction is fundamentally two-way, while one-way coupling may be advantageous under certain conditions [18]. In a one-way coupling, the Navier-Stokes equations, radiation transport equations, etc., for the fluid domain in a fire compartment are solved for the complete time duration of interest by a CFD code to get gas temperatures, velocities, chemical species, incident heat fluxes, film coefficients, etc. The heat equations for the solid domain (building elements) use the thermal boundaries from the CFD simulation to get the thermal response (temperature rise) within the building elements. Kinematics equations, constitutive equations, etc., for the solid domain are solved by a FEM code to get the deformations, stresses, strains, etc. Fire-structure and thermo-mechanical interfaces are used to transfer data between different models. In a two-way

coupling, the same set of equations is solved except that at discrete time steps through the simulation the solid phase FEM code provides feedback to update the CFD model.

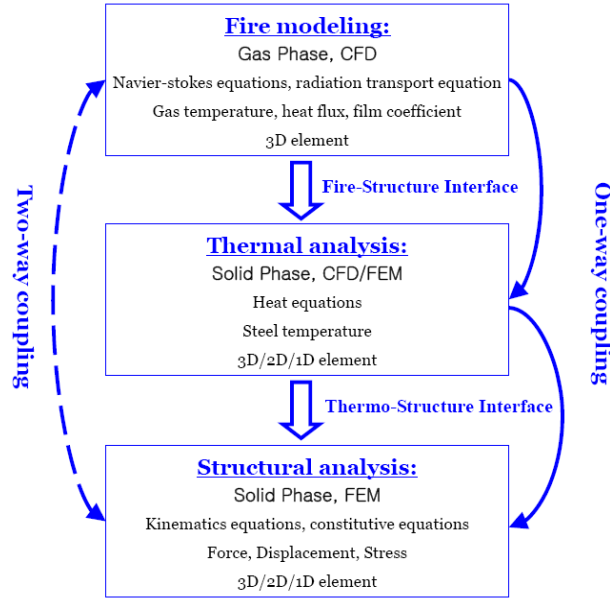


Figure 1. Coupled CFD-FEM Simulation Approach for Structural Fire Analysis [24]

2.2 The FDS Code

Fire Dynamics Simulator (FDS) is a large-eddy simulation (LES) based CFD code [19]. In this study, FDS version 5 is used. LES is a technique used to model the dissipative processes (viscosity, thermal conductivity, material diffusivity) that occur at length scales smaller than those that are explicitly resolved on the numerical grid. In FDS, the combustion is based on the mixing-limited, infinitely fast reaction of lumped species, which are reacting scalars that represent mixtures of species. Thermal radiation is computed by solving the radiation transport equation for gray gas using the Finite Volume Method (FVM) on the same grid as the flow solver. FVM is based on a discretization of the integral forms of the conservation equations. It divides the problem domain into a set of discrete control volumes (CVs) and node points are used within these CVs for interpolating appropriate field variables. The governing equations are approximated on one or more rectilinear grids. Obstructions with complex geometries are approximated with groups of prescribed rectangles in FDS. One-dimensional (1D) heat conduction is assumed for solid-phase calculations. Detailed descriptions of the mathematical models used in FDS can be found in [19].

2.3 The Fire Structure Interface

The concept of adiabatic surface temperature is used to transfer thermal boundary data from a FDS model to a FEM model. Consider an ideal adiabatic surface exposed to a heating condition; the net heat flux to the surface is by definition zero, thus

$$\varepsilon_{AS} (\dot{q}_{in}'' - \sigma T_{AS}^4) + h_{c,AS} (T_g - T_{AS}) = 0 \quad (1)$$

where ε_{AS} is emissivity of the adiabatic surface; T_{AS} is temperature of the adiabatic surface or adiabatic surface temperature; and $h_{c,AS}$ is film coefficient between the adiabatic surface and the surrounding gas.

From Eq. 1, the incident radiative flux to a surface can be calculated from an adiabatic surface temperature,

$$\dot{q}_{in}'' = \frac{h_{c,AS}(T_{AS} - T_g)}{\varepsilon_{AS}} + \sigma T_{AS}^4 \quad (2)$$

Consider a real surface exposed to the same heating condition, the net heat flux to the surface can be calculated by

$$\dot{q}'' = \varepsilon_s \sigma (T_{AS}^4 - T_s^4) + \frac{\varepsilon_s}{\varepsilon_{AS}} h_{c,AS} (T_{AS} - T_g) + h_c (T_g - T_s) \quad (3)$$

If the emissivity of the adiabatic surface is taken as the emissivity of the real surface ($\varepsilon_{AS} = \varepsilon_s$), and the film coefficient between the adiabatic surface and the surrounding gas is equal to the film coefficient between the real surface and the surrounding gas ($h_{c,AS} = h_c$), we get

$$\dot{q}'' = \varepsilon_s \sigma (T_{AS}^4 - T_s^4) + h_c (T_{AS} - T_s) \quad (4)$$

Eq. 4 shows that the net heat flux to a surface can be approximately calculated by using a single parameter T_{AS} . In practice, the adiabatic surface temperatures of interest can be approximately measured by a plate thermometer [27]. Consider the case at high temperature (above about 400 °C), where convection is not the dominant mode of heat transfer in fire [28]; from Eq. 3 or 4 the adiabatic surface temperature measured by a plate thermometer can be used to predict the net heat flux to a surface with a different emissivity. FDS [18] includes an output quantity of adiabatic surface temperature calculated by Eq. 4 according to the idea proposed by Wickstrom [29]. It should be noted that the calculated adiabatic temperature of a surface is fundamentally influenced by the convection or film coefficient (see Eq. 3) so that the value for film coefficient should be carefully selected when using the concept for calculations where convection is important [30].

3. VALIDATION STUDY

3.1 Description of the Experiment

Figure 2 shows the experimental layout in Hasemi et al.'s experiments [26]. The rectangular flat ceiling consists of two layers of 12 mm thick mineral fiber Perlite board with dimensions 1.83×3.60×0.024 m. The ceiling is reinforced by a steel frame and is horizontally placed over the beam held by two steel vertical posts at the ends. H-section bare steel beam with the following dimensions was used: 3.6 m long, 75 mm width, 150 mm height, 5 mm (thickness of web), 6 mm (thickness of flange). The height of the beam and the ceiling was adjusted by lifting these specimens up and down the posts. Heat flux measurements were made at nine horizontal distances from the stagnation point of the beam. Water-cooled Schmidt-Boelter heat flux gauges were installed flush with the beam surface through the holes made in the beam shown in Figure 2. The heat flux to the upper flange, web and also lower and upper surfaces of the lower flange was measured. Temperature measurements were made with thermocouples at 27 points, arranged symmetrically to the points of the heat flux gauges with regard to the center of the beam. Thermocouples were 0.2 mm K-type and were installed 0.5 mm from the beam surface, as shown in Figure 2. A 0.5 m diameter round and a 1.0 m square porous propane burner were used as the fire source.

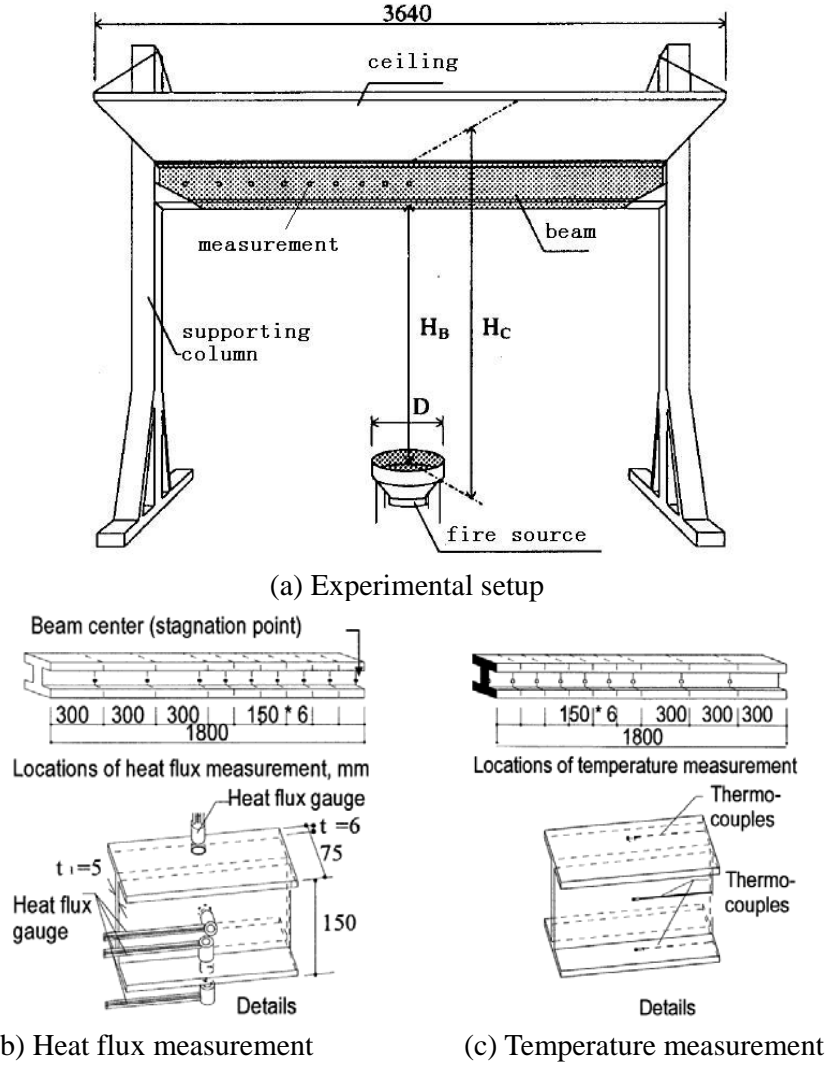


Figure 2. Experimental Setup and Measurements in Hasemi et al.'s Test [26]

3.2 FDS Numerical Model

Figure 3 shows the FDS numerical model for the localized fire test cases using 1.0 m square burner in [26]. Two cases with steady heat release rates of 540 kW and 900 kW were considered. In both cases, the distance from the burner to the lower flange of the ceiling beam was 1.2 m. The computational domain had dimensions of 4.0 m (X) \times 2.0 m (Y) \times 1.8 m (Z). Boundary conditions at four sides of the computational domain are opening. The flanges and web of the beam were modeled as steel sheets with thickness of 6mm. Both ceiling and floor were modeled as 24 mm thick perlite boards. The densities of steel and perlite were 7850 kg/m³ and 789 kg/m³ [31]. The emissivity of all solid surfaces was taken as 0.9 [31]. Other properties of the materials were taken from [31]

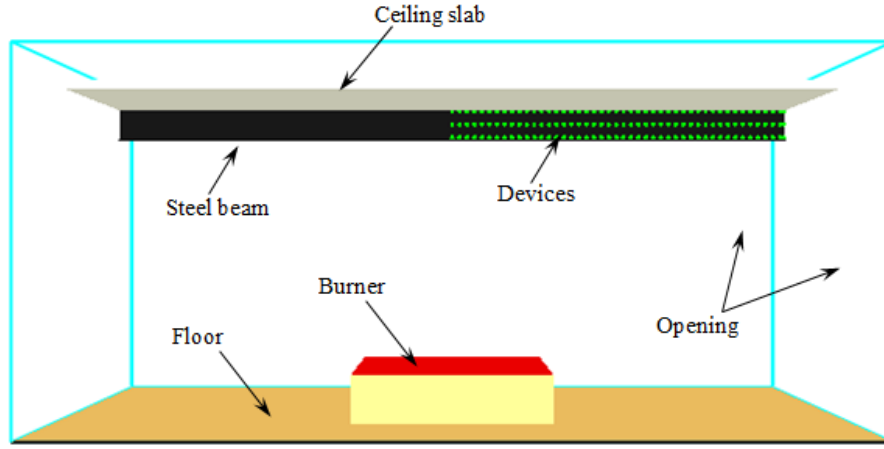
$$c_s = 582.3 - 0.8896T + 2.289 \times 10^{-3}T^2 - 1.486 \times 10^{-6}T^3 + 2.97 \times 10^{-10}T^4 \quad (5)$$

$$c_p = 1493 - 4.658T + 0.013743T^2 - 1.4585 \times 10^{-4}T^3 + 5.128 \times 10^{-9}T^4 \quad (6)$$

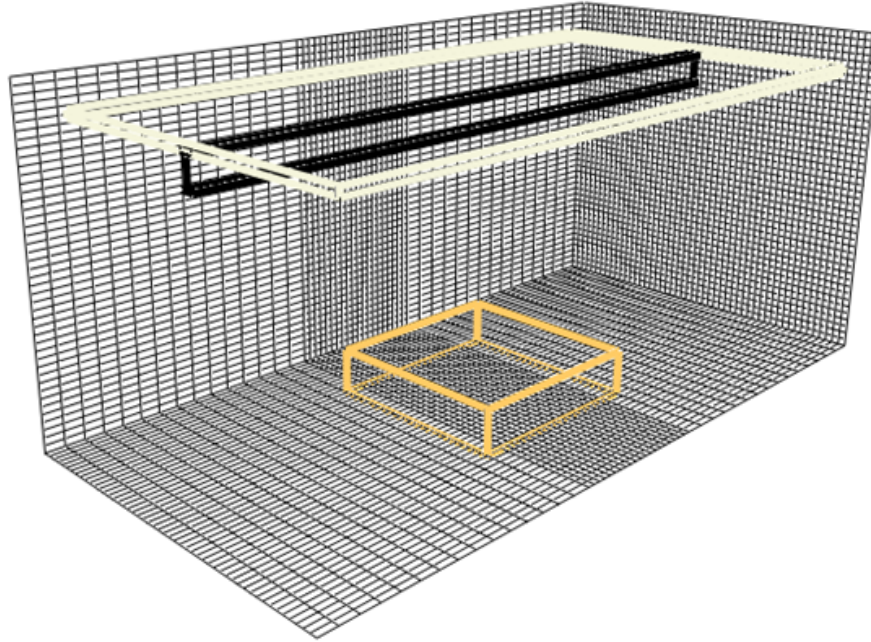
$$k_s = 70.45 - 0.02767T - 4.847 \times 10^{-5}T^2 + 4.722 \times 10^{-8}T^3 - 1.068 \times 10^{-11}T^4 \quad (7)$$

$$k_p = 0.3314 - 8.834 \times 10^{-4}T + 1.932 \times 10^{-6}T^2 - 1.96 \times 10^{-9}T^3 + 7.226 \times 10^{-13}T^4 \quad (8)$$

where c_s , ρ_s are the specific heat of steel and perlite respectively; k_s, k_p are the conductivity of the steel and perlite respectively.



(a)



(b)

Figure 3. FDS Model for the Investigated Localized Fire Case

The grid sizes used is one of the most important numerical parameter in CFD dictating its numerical accuracy. The necessary spatial resolution for a proper LES simulation is customary defined in terms of the characteristic diameter of a plume, which is defined as [19],

$$D^* = \left(\frac{\dot{Q}}{\rho_\infty c_p T_\infty \sqrt{g}} \right)^{2/5} \quad (9)$$

The special resolution R^* of a numerical grid is defined as,

$$R^* = \frac{\delta x}{D^*} \quad (10)$$

where δx is the characteristic length of a cell for a given grid. The necessary resolution suggested in most studies is between 1/5 and 1/20 [19]. For the FDS model, the whole domain consisted of 50 (X) \times 50 (Y) \times 45 (Z) = 112,500 control volumes. The grids in the Y and Z directions were uniform (4 cm), where that in the X direction was stretched to yield the grid size in the flame region of 4 cm. Therefore, the resolution at the flame region was about 1/23 for 900 kW and about 1/19 for 450 kW.

3.3 FEM Thermal Model

Figure 4 shows the FEM model for the ceiling beam composite. By symmetry, a quarter of the composite was used. By the consideration that the temperatures of the lower flange and web of the steel I beam were not significantly affected by the thermal conduction from the ceiling slab, the width of the ceiling slab was taken as a half of the steel I beam in the FE model. The three dimensional (3D) layered shell element SHELL131 in ANSYS was used. SHELL131 has in-plane and through-thickness thermal conduction capacity. It has 4 nodes with up to 32 temperature degrees of freedom at each node. Thermal conduction through-thickness for the lower flange and the web of the steel I beam was ignored because of the high conductivity of steel. The composite section of the steel upper flange and perlite slab was divided into one steel layer and 5 perlite layers to consider thermal conduction between the upper flange and the slab (Figure 4b). As shown in Figure 4c, an additional external node was defined for each element (SHELL131) to apply the thermal boundary condition using the concept of adiabatic surface temperature (*AST*). The temperature of the external node was taken as the *AST* for the element (surface) transferred from FDS.

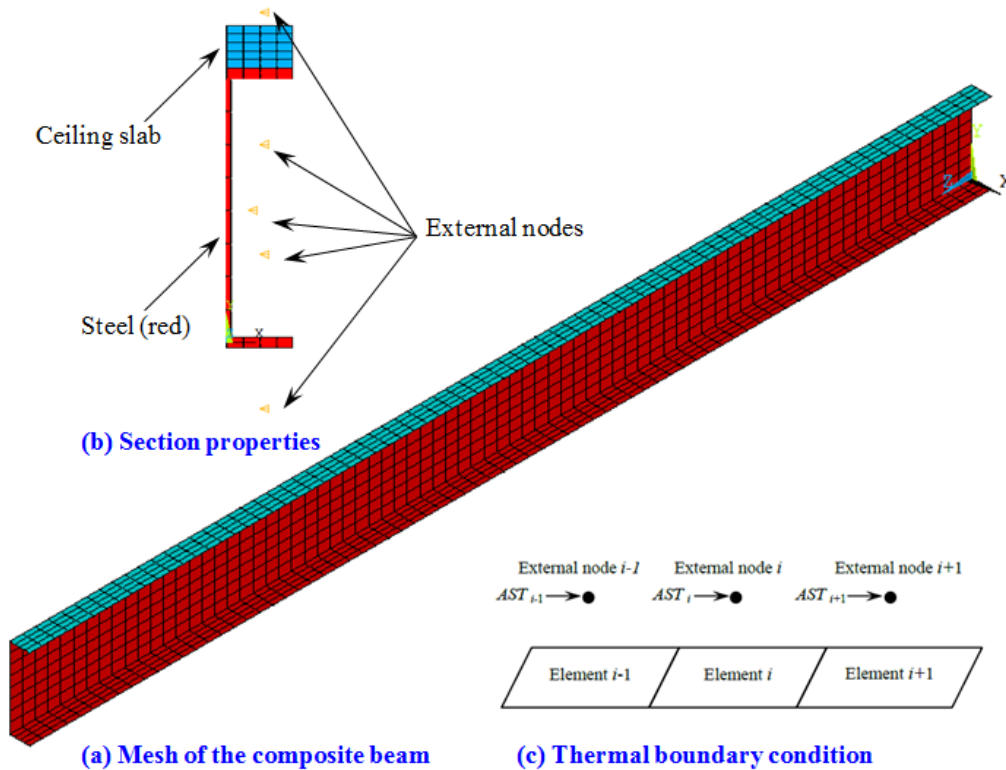


Figure 4. FE Model for the Investigated Localized Fire Case

4. RESULTS AND DISCUSSION

Figure 5 shows the time history of the heat fluxes and adiabatic surface temperatures (*ASTs*) predicted by FDS. The fluctuation of the curves is due to the turbulent combustion behavior. Figure 6 shows the time averaged *ASTs* along the length of the beam. The unsmoothness of the curves is because the measured value of a point located in a control volume is taken as the value of the nearby grid point. The horizontal axis, x , is the distance to the beam center. *ASTs* decrease with increasing the distance to the beam center. Generally, the bottom surface of the lower flange has the highest *ASTs*. The other surfaces have similar *ASTs*.

Figures 7 and 8 show the good match between the FDS predicted heat fluxes and the test data. The difference between the predicted and measured maximum heat fluxes was about 3 kW/m² (about 7%) for the 540 kW case and about 5 kW/m² (about 6%) for the 900 kW case. Figure 9 compares the FDS-FEM predicted steel temperatures with the test data. For the lower flange and the web of the steel I beam, the predicted steel temperatures agree very well with the test data. The over-prediction of maximum steel temperature for the lower flange is about 60 °C (about 11%) and for the web is about 44 °C (about 8%). The under-prediction of the upper flange steel temperature is caused by the ignorance of the horizontal heat conduction between the nearby slab to the steel section. Figure 10b shows the distribution of the *ASTs* on the exposed surfaces. Because of the flame impingement (Figure 10a) the *ASTs* on the slab surface were higher than those on the upper flange surface, which indicated that heat fluxes were transferred from the slab to the steel in some area.

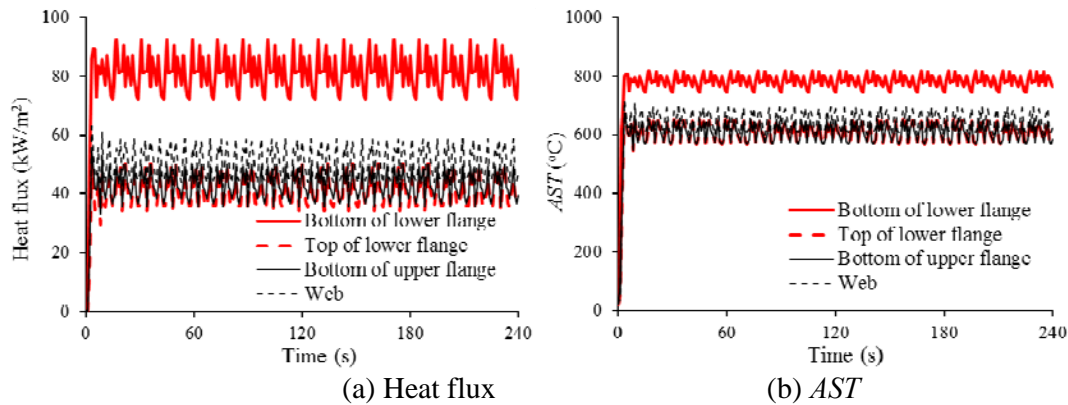


Figure 5. Time History of FDS Predicted Heat Fluxes and *ASTs* (900 kW case)

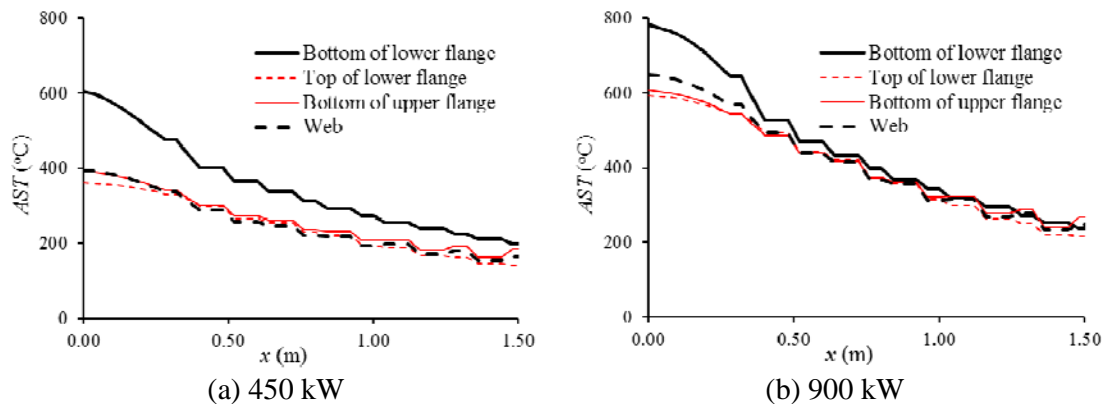


Figure 6. Time Averaged *ASTs*

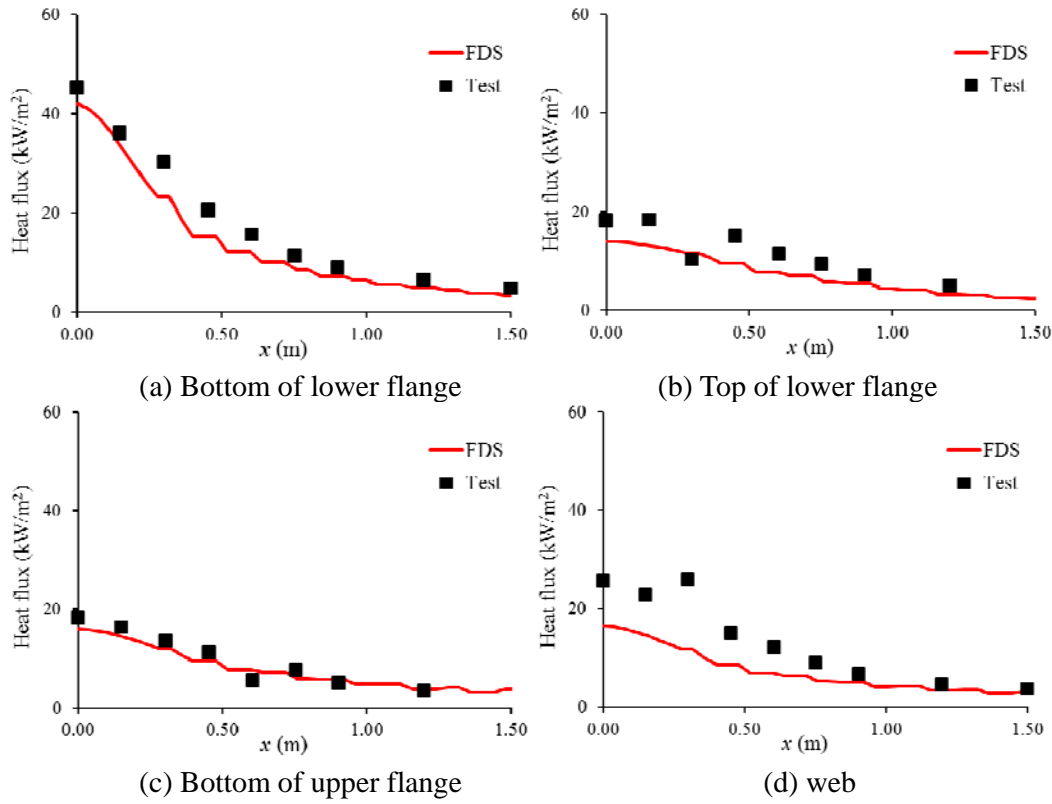


Figure 7. FDS Predicted Heat Fluxes and the Test Data for the Investigated Case with HRR of 450 kW

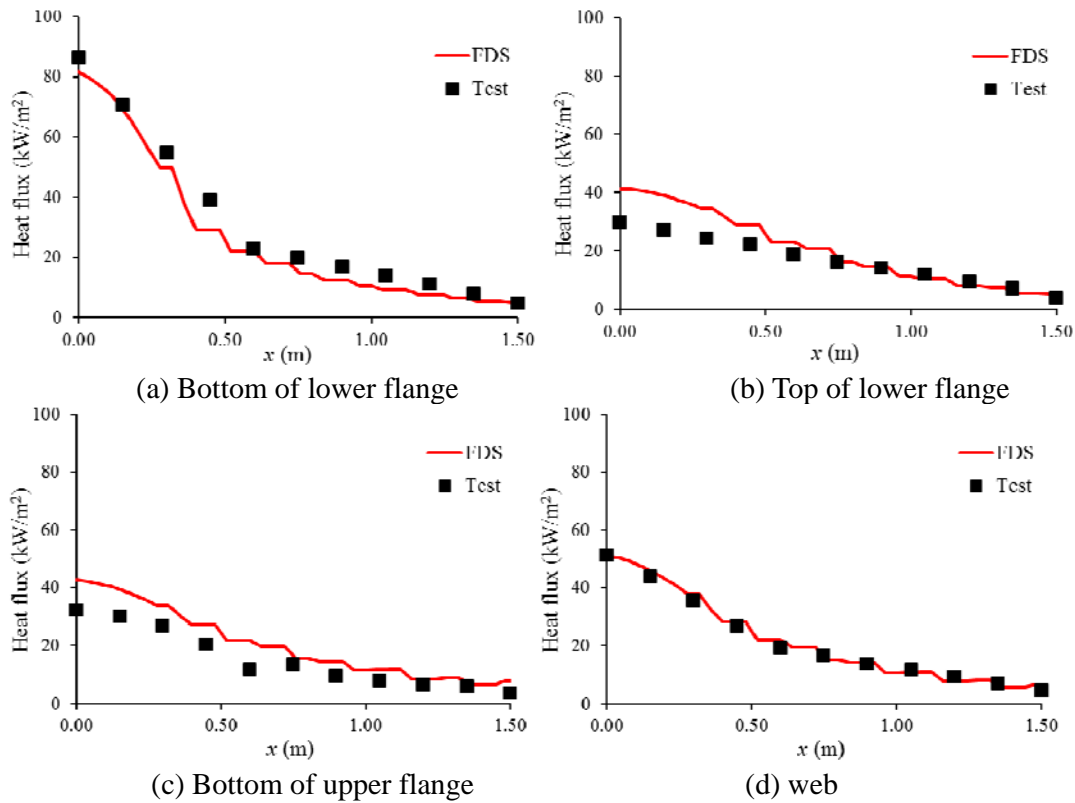


Figure 8. FDS Predicted Heat Fluxes and Test Data for the Investigated Case with HRR of 900 kW

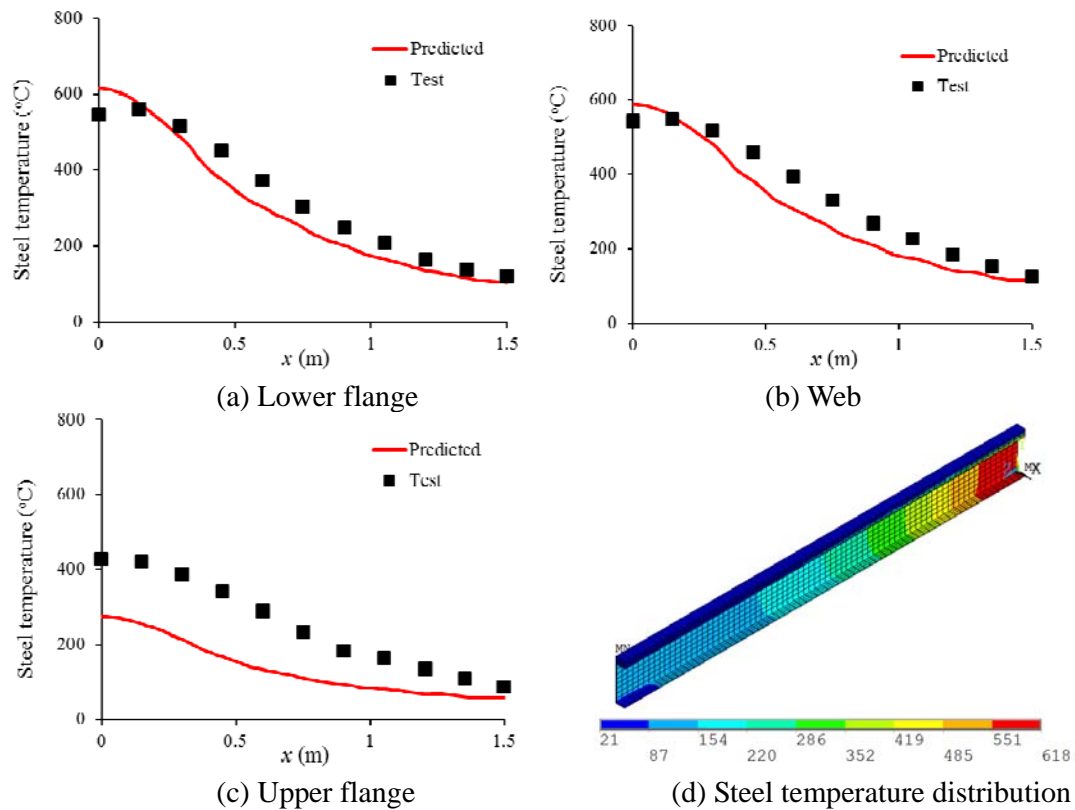
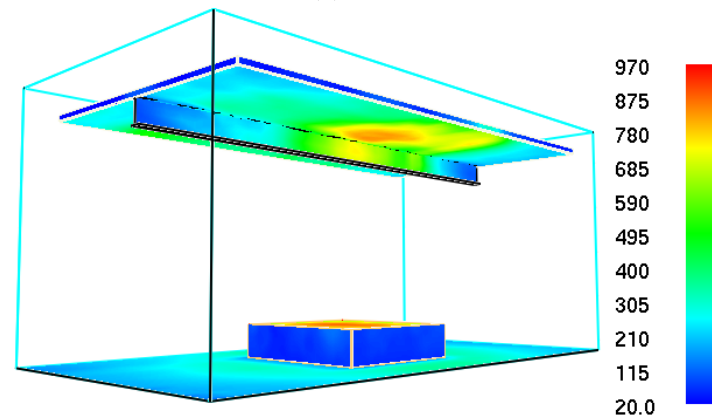


Figure 9. FDS-FEM Predicted Steel Temperatures for the Investigated Case with HRR of 900 kW



(a) Flame



(b) Adiabatic surface temperature

Figure 10. FDS Predicted Adiabatic Surface Temperature

5. CONCLUSIONS

This paper discusses the integrated fire-structure simulation methodology for performance based fire safety design. A fire-structure interface, named adiabatic surface temperature, was applied to transfer data from FDS to ANSYS. By comparing the predicted and measured heat fluxes and steel temperatures of a steel ceiling beam exposed to a localized fire condition, the FDS-FEM method was tested. The FDS predicted heat fluxes match well with the test data. The difference between the predicted and measured maximum heat fluxes was within 6% for the investigated two cases. The FDS-FEM method gave good prediction of the steel temperatures. The over-prediction of maximum steel temperature was within 11% for the investigated case. The methods described in this study provide a feasible way to study the complex behavior of structures in realistic fires.

REFERENCES

- [1] BSI. Eurocode 3: Design of Steel Structures, Part 1.2: General Rules – Structural Fire Design. British Standard, 2005.
- [2] McAllister, T.P., Gann, R.G., Averill, J.D., Gross, J.L., Grosshandler, W.L., Lawson, J.R., McGrattan, K.B., Nelson, H.E., Pitts, W.M., Prasad, K.R. and Sadek, F.H., “Federal Building and Fire Safety Investigation of the World Trade Center Disaster: Structural Fire Response and Probable Collapse Sequence of World Trade Center Building 7. NIST NCSTAR 1–9”, National Institute of Standards and Technology, Gaithersburg, MD, USA, 2008.
- [3] National Institute for Land and Infrastructure Management (NILIM). Report on the Windsor Building Fire in Madrid, Spain, Japan, 2005.
- [4] Garlock, M., Kruppa, J., Li, G.Q. and Zhao, B., “Fire Behavior of Steel Structures (White Paper)”, Fire Resistance Structures Workshop, NIST, May 2014.
- [5] Zhang, C. and Li, G.Q., “Fire Dynamic Simulation on Thermal Actions in Localized Fires in Large Enclosure”, *Advanced Steel Construction*, 2012, Vol. 8, pp. 124–36.
- [6] Bailey, C.G., “Membrane Action of Unrestrained Lightly Reinforced Concrete Slabs at Large Displacements”, *Engineering Structures*, 2001, Vol. 23, pp. 470-83.
- [7] Li, G.Q., Guo, S.X. and Zhou, H.S., “Modeling of Membrane Action in Floor Slabs Subjected to Fire”, *Engineering Structures*, 2007, Vol. 29, pp. 880-87.
- [8] Liu, T.C.H., Fahad, M.K. and Davies, J.M., “Experimental Investigation of Behaviour of Axially Restrained Steel Beams in Fire”, *Journal of Constructional Steel Research*, 2002, Vol. 58, pp. 1211-30.
- [9] Li, G.Q. and Guo, S.X., “Experiment on Restrained Steel Beams Subjected to Heating and Cooling”, *Journal of Constructional Steel Research*, 2008, Vol. 64, pp. 268-74.
- [10] SCI P113. Structural Fire Engineering: Investigation of Broadgate Phase 8 Fire, The Steel Construction Institute, 1991.
- [11] Kirby, B.R., “The Behaviour of a Multi-story Steel Framed Building Subjected to Fire Attack, Experimental Data”, British Steel, 2000.
- [12] Zhang, C., Li, G.Q. and Usmani, A., “Simulating the Behavior of Restrained Steel Beams to Flame Impinged Localized Fires”, *Journal of Constructional Steel Research*, 2013, Vol. 83, pp. 156-65.
- [13] Zhang, C., Gross, J.L. and McAllister, T., “Lateral Torsional Buckling of Steel W-beams to Localized Fires”, *Journal of Constructional Steel Research*, 2013, Vol. 88, pp. 330-8.
- [14] Zhang, C., Gross, J.L., McAllister, T.P. and Li, G.Q., “Behavior of Unrestrained and Restrained Bare Steel Columns Subjected to Localized Fire”, *Journal of Structural Engineering-ASCE*, 2015, Vol.141. DOI:10.1061/(ASCE)ST.1943-541X.0001225.

- [15] Zhang, C., Choe, L., Seif, M. and Zhang, Z., Behavior of Axially Loaded Steel Short Columns Subjected to a Localized Fire”, *Journal of Constructional Steel Research*, 2015 Vol. 111, pp. 103-111.
- [16] Li, G.Q. and Zhang, C., “The Chinese Performance-based Code for Fire-resistance of Steel Structures”, *International Journal of High-Rise Buildings*, 2013, Vol. 2, pp. 123-30.
- [17] Li, G.Q. and Zhang, C., “Creep Effect on Buckling of Axially Restrained Steel Columns in Real Fires”, *Journal of Constructional Steel Research*. 2012, Vol. 71, pp. 182-8.
- [18] Welch, S., Miles, S.D., Kumar, S., Lemaire, T. and Chan, A., “Firestruc – Integrating Advanced Three-dimensional Modelling Methodologies for Predicting Thermo-mechanical Behaviour of Steel and Composite Structures Subjected to Natural Fires”, *Fire Safety Science*, 2008, Vol. 9, pp. 1315-26.
- [19] McGrattan, K., Klein B., Hostikka, S., and Floyd J., “Fire Dynamics Simulator (Version 5), User's Guide”, NIST Special Publication 1019-5, National Institute of Standards and Technology, Gaithersburg, MD, USA, 2007.
- [20] Li, G.Q. and Zhang, C., “Thermal Response of Steel Columns Exposed to Localized Fires - Numerical Simulation and Comparison with Experimental Results”, *Journal of Structural Fire Engineering*, 2011, Vol. 2, pp. 311-7.
- [21] Tondini, N., Vassart, O. and Franssen, J.M., “Development of An Interface between CFD and FE Software”, In *Proceedings of the Seventh International Conference on Structures in Fire*, pp. 459-68, Zurich, Switzerland, 2012.
- [22] Alos-Moya, J., Paya-Zaforteza, I., Garlock, M.E.M., Loma-Ossorio, E., Schiffner, D. and Hospitaler, A., “Analysis of a Bridge Failure due to Fire Using Computational Fluid Dynamics and Finite Element Models”, *Engineering Structures*, 2014, Vol. 68, pp. 96-110.
- [23] Henneon, N., Roosed, M. and Zhao, B., “Application of Structural Fire Safety Engineering to the Canopy of the Forum DES Halles, in Paris”, In *Proceedings of the 8th International Conference on Structures in Fire*, pp. 1047-54, 2014.
- [24] Zhang, C., Silva, J.G., Weinschenk, C., Kamikawa, D. and Hasemi, Y., “Simulation Methodology for Coupled Fire-Structure Analysis: Modeling Localized Fire Tests on a Steel Column”, *Fire Technology*, 2016, Vol.52, pp.239-62.
- [25] Hasemi, Y., Yokobayashi, Y., Wakamatsu, T. and Ptchelintsev, A., “Modeling of Heating Mechanism and Thermal Response of Structural Components Exposed to Localized Fires: A New Application of Diffusion Flame Modeling to Fire Safety Engineering”, NIST Internal Report 6030, National Institute of Standards and Technology, Gaithersburg, Maryland, 1997.
- [26] Yokubayashi, Y., Hasemi, Y. and Wakamatsu, T., “Experimental Study on the Heating Mechanism and Thermal Response of a Steel Beam under Ceiling Exposed to Localized Fires”, *J. Struct. Constr. Eng., AIJ*, 1997, Vol. 498, pp. 169-75. (in Japanese).
- [27] Wickstrom, U., “The Plate Thermometer - A Simple Instrument for Reaching Harmonized Fire Resistance Tests”, *Fire Technology*, 1994, Vol. 30, pp. 195-208.
- [28] Zhang, C. and Usmani, A., “Heat Transfer Principles in Thermal Calculation of Structures in Fire”, *Fire Safety Journal*, 2015, Vol. 78, pp. 85-95.
- [29] Wickstrom, U., Duthinh, D. and McGrattan, K.B., “Adiabatic Surface Temperature for Calculating Heat Transfer to Fire Exposed Structures”, In *Proceedings of the 11 the International Interflam Conference*, pp. 943-53, London, England, 2007.
- [30] Zhang, C., Li, G.Q. and Wang, R.L., “Using Adiabatic Surface Temperature for Thermal Calculation of Steel Members Exposed to Localized Fires”, *International Journal of Steel Structures*, 2013, Vol. 13, pp. 547-58.
- [31] Wakamatsu, T., Hasemi, Y. and Ptchelintsev, A.V., “Heating Mechanism of Building Components Exposed to a Localizedfire: CFD Prediction of the Heat Flux of a Steel Beam”, *Fire Science & Technology*. 2000, Vol. 20, pp. 1-12.

STRUCTURAL PERFORMANCE OF BOLTLESS BEAM END CONNECTORS

S.N.R. Shah¹, N.H. Ramli Sulong^{2,*}, R. Khan³ and M.Z. Jumaat²

¹*Civil Engineering Department, Mehran University of Engineering & Technology, SZAB Campus, Khairpur, Pakistan*

²*Department of Civil Engineering, University of Malaya, 50603, Kuala Lumpur, Malaysia*

³*Mechanical Engineering Department, Al-Imam Muhammad Ibn Saud Islamic University, Riyadh 11432, Kingdom of Saudi Arabia*

**(Corresponding author: E-mail: hafizah_ramli@um.edu.my)*

Received: 9 May 2016; Revised: 23 July 2016; Accepted: 13 August 2016

ABSTRACT: This study examines the structural performance of beam end connectors used as connection device in semi-rigid boltless beam-to-column connections (BCCs) in steel pallet racks (SPRs). A total of six types of specimens were tested which were distinguished by the three different types of beam end connector (BEC) thicknesses and two different numbers of tabs in the (BEC). The experimental testing was performed using double-cantilever test method and the moment-rotation ($M-\theta$) behavior of the connections and key failure modes were evaluated. The influence of variation in the thickness and the number of tabs of the BEC on the behavior of connection was also investigated. Increased connector thickness enabled the connector tabs to sustain higher failure moment. The findings showed that by varying the geometrical properties, the stiffness of the connection was affected at a higher rate as compared to the strength of the connection. A non-linear three dimensional (3D) finite element (FE) model was developed to simulate the experimental investigations. The FE model showed a close agreement with experimental results.

Keywords: steel pallet racks, beam end connector, moment-rotation behavior, double-cantilever test, down-aisle direction

DOI: 10.18057/IJASC.2017.13.2.4

1. INTRODUCTION

Steel storage racks are the most widely used cold-formed steel (CFS) structures for the storage of multitude of goods in the warehouses and supermarkets [1]. These lightweight structures can carry live loads much heavier than their self-weight [2]. The most commonly used type of storage racks is 'steel pallet racks (SPRs)'. The SPRs satisfactorily solve the storage problems when the space available to store the goods is comparatively less sufficient to the volume of items. These racks require a ready re-adjustment of the members depending upon the storage requirement [1]. Despite a variety in the manufacturing of steel storage racks, the main configuration of these structures is classified into two major directions, namely, the cross-aisle direction and down-aisle direction. The cross-aisle direction is braced with struts whereas, bracing is avoided in the down-aisle direction and the stability of the frame is governed by the beam-to-column connections (BCCs). The bracing in cross-aisle direction starts generally at 160 mm from the bottom of the column. The bracing is connected to the column using bolts and nuts. For horizontal bracing to column, a brace spacer is fitted over the bolt to locate the bracing against the inside flange of the column. Standard base plates are used with anchor bolts for floor-to-column connection.

As a consequence of its constructional design, a storage rack differs very much from a traditional steel framework. For instance, the columns used in storage racks have pre-designed perforations, depending on an optimal pitch, in their cross-section. The column of a rack frame is a vertical member subjected to compressive forces parallel to their longitudinal axes [3]. The perforated columns used in SPRs are thin shell elements. The thickness of these columns normally varies

between 1.8 mm and 3.0 mm. Perforations in columns reduce their cross-sectional area and make them vulnerable for local and/or distortional buckling [4]. A global buckling of the structure may also happen if these columns are not properly designed. The other unique feature of SPRs are the unique boltless connections used as BCCs in these structures [5]. These boltless connections are considered semi-rigid connections in nature [2]. By contrast to the common structural steel connections where bolts or welds are used for joining the beams and columns, these structures utilized a connection device namely the 'beam end connector' (BEC), which is welded at the end of pallet beam and its stiffness supports the bending capacity of the pallet beam. Unique types of hooks are punched inside the BEC which are engaged with column perforations in a special manner to establish the BCCs [6] and allowed free to rotate. A safety lock must be fully inserted into every BEC. If installed correctly, the safety lock will be positioned vertically, with long leg pointing downwards. Once the end connector is secured with the safety locks, the beam can resist an upward force. This helps the BEC to stay in desired position under the accidental impact of fork lift truck when lifting the pallets [6]. Figure 1 shows a typical boltless SPR BCC.

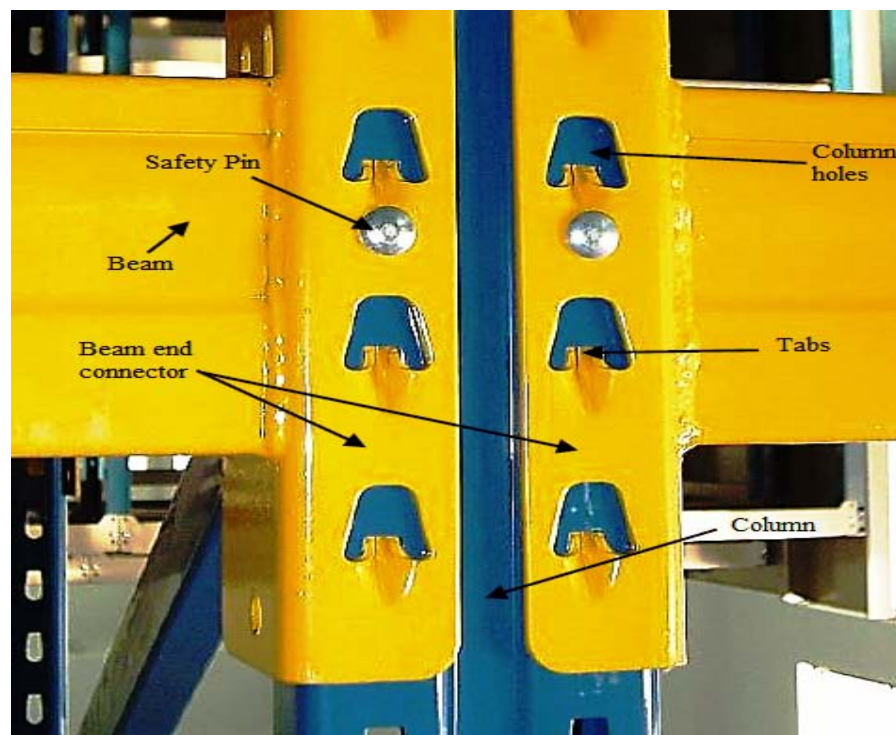


Figure 1. Typical SPR BCC

Despite the availability of several studies available on the behavior of traditional steel connections [7-10], the studies discussing the behavior of SPR BCCs are rare. Being not similar to common building steel connections, the difference in geometry of the BECs available in the market does not allow a generalized global analytical model. This motivated the researchers to predict the structural behavior of SPR BCCs through experimental testing and numerical modelling. Markazi et al. [11] tested different types of connectors using simple cantilever method and declared the influential parameters and failure modes of BCCs. In another study of Markazi et al. [12], numerical modeling was performed for semi-rigid boltless connections and experimental results were validated.

The connection influence on overall rack performance under monotonic and cyclic loading was also investigated by Bernuzzi and Castiglioni [13]. The distortion of tabs and the nodal zone were the governing failure modes. Furthermore, the loading types and the design of connectors also affected the behavior of connections.

Filiatrault et al. [14], Filiatrault et al. [15] and Sideris et al. [16] also investigated the behavior of connection while testing the overall rack structure under seismic loading. Zhao et al. [17] tested the storage rack connections using the standard cantilever testing and useful information was provided. Recently, Castiglioni [18] provided significant information about the seismic performance of SPR systems and highlighted the important design considerations required for seismic design of various components of racking systems included BCCs. Shah et al. [19] highlighted the behavior and performance of SPR BCCs under fire using experimental and numerical investigations. Literature suggests that in order to develop a general analytical model, experimental testing of different types of BEC should be performed [20, 21].

This study emphasizes on experimental testing and finite element (FE) analysis of SPR BCCs. Three different thicknesses of the BECs with different number of tabs were tested. The dimensions of the column and pallet beam were kept constant throughout the investigations. The dominant types of failure were observed and the moment-rotation ($M-\theta$) relationship was developed. The effect of the thickness and depth of the BEC is also highlighted. A non-linear three dimensional (3D) FE model was generated and validated against the experimental results.

2. EXPERIMENTAL INVESTIGATIONS

2.1 Material Properties

CFS sections were used for columns and beams. Hot rolled steel was used to manufacture the BEC. Table 1 shows the material properties of the connection components.

Table 1. Material Properties of the Specimens

Member	Young's Modulus (E) (GPa)	Poisson's ratio (ν)	Yield strength (f_y) (MPa)	Ultimate strength (f_u) (MPa)
Column	210	0.3	459	575
Beam			353	497
BEC			263	365

2.2 Specimen Details

Six tests were conducted based on the differences in the thickness and number of tabs of the BEC. The type of column perforation is shown in Figure 2.

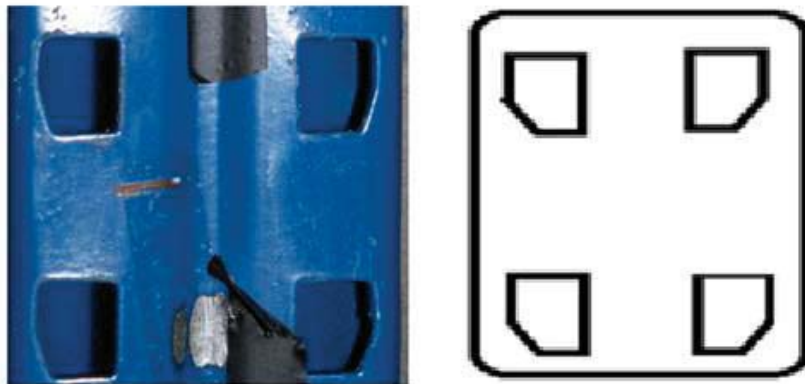


Figure 2. Type of Column Perforation

The cross section and dimensions of the column section are given in Figure 3 (a) and Table 2, respectively. Box beam was used for testing and its cross section is shown in Figure 3 (b). The detail of the beam section is given in Table 3. B represents the types of beam, i.e., box beam. The dimensions and cross section of the BEC are presented in Table 4 and Figure 3 (c), respectively. The numbers are used to show the thickness of the BEC. Symbol 'A' is used to show the connectors with three tabs, whereas symbol 'B' is used to show the connector with five tabs. For instance, the type of the BEC '2A' shows that the three-tab BEC with a thickness of 2 mm.

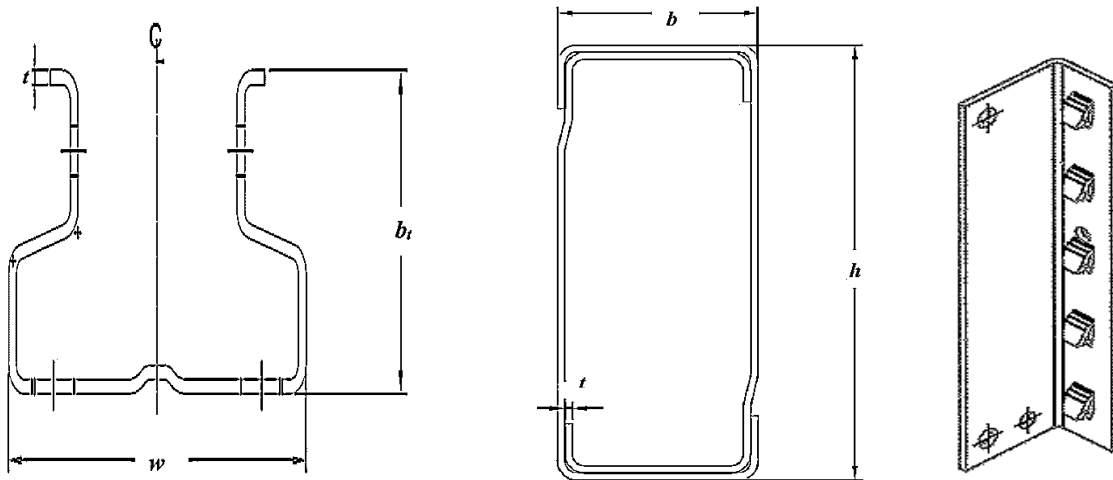


Figure 3. Cross-section of the Connection Components
(a) Column, (b) Beam, (c) BEC

Table 2. Dimension Details of Column

Thickness 't' (mm)	Web 'w' (mm)	Flange width 'b _t ' (mm)	Height 'h' (mm)
2.0	112.2	67.6	500

Table 3. Beam Dimensions

Beam type	Width 'b' (mm)	Depth 'h' (mm)	Thickness 't' (mm)
B	40	92	1.5

Table 4. Dimension Detail of the Tested BECs

Type of the BEC	Number of tabs	Breadth 'b' (mm)	Width 'w' (mm)	Depth 'h' (mm)	Thickness 't' (mm)
2A	3	40	64	150	2
2B	5	40	64	250	2
4A	3	40	64	150	4
4B	5	40	64	250	4
6A	3	40	64	150	6
6B	5	40	64	250	6

Each set of specimen is given a specific specimen ID. For example, in the specimen ID 'B-2.0UT-92BD-3T-2CT', 'B' indicates the type of beam (box beam), 2.0UT represents the column thickness as 2.0 mm, 92 BD represents the depth of beam as 92 mm, 3T represents the number of tabs in the connector which is three, and 2CT represents the thickness of the BEC, which is 2 mm. For an easy understanding, each specimen has been assigned a numeric ID which is listed in Table 5.

Table 5. Numeric ID Assigned to the Specimens

Specimen ID	Numeric ID
B-2.0UT-92BD-3T-2CT	Specimen 1
B-2.0UT-92BD-3T-4CT	Specimen 2
B-2.0UT-92BD-3T-6CT	Specimen 3
B-2.0UT-92BD-5T-2CT	Specimen 4
B-2.0UT-92BD-5T-4CT	Specimen 5
B-2.0UT-92BD-5T-6CT	Specimen 6

A sketch of tested specimen 5 with its dimensions is shown in Figure 4. The connection depicts a BEC of 4 mm is welded to one end of the beam with tabs punched into it. The leg of the angle with tabs is in contact with column web after assembly, while there is a 2 mm gap between the second legs, perpendicular to the column web. Figure 4 is modified from Figure 2 of [2]. However, in this study, the tabs of the BEC were reversely engaged into the column perforations.

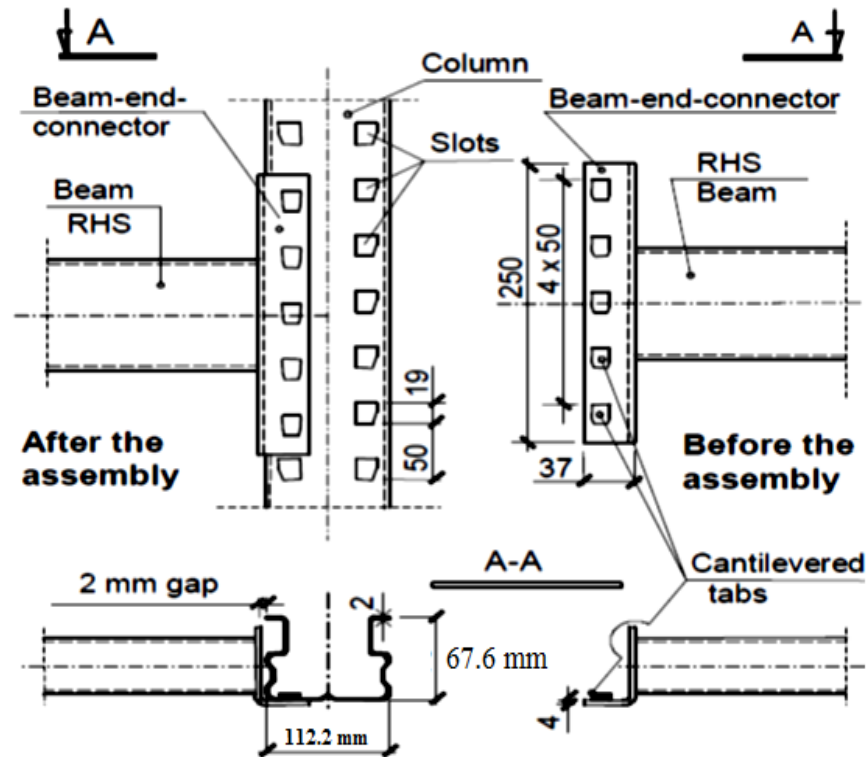


Figure 4. Dimensions of Tested Connection (Specimen 5)

2.3 Selection of Test Method

The international design standards of storage rack design such as The Rack Manufacturing Institute (RMI) [22], European Committee for Standardization (EN 15512) [23] and Standards Australia (AS4084) [24] suggest alternative testing methods for the testing of SPR BCCs. The RMI [22] and AS4084 [24] suggest 'Cantilever test method' and 'Portal frame test method', whereas the EN

15512 [23] suggest only Cantilever Test Method which considers a cantilever beam connected to the perforations of column through tabs. This test method was modified by researchers [25, 26] by attaching an extra beam to the other side of column and placing the column in between two full length beams and, hence, is called the double cantilever test method. The efficiency of the double-cantilever test method for the testing of SPR BCCs is clearly evident in various studies [25-27]. This study has followed the double-cantilever test method to forecast the M- θ behavior of SPR BCCs.

2.4 Testing Arrangement

Figure 5 shows the schematic diagram of experimental arrangement used in this research for connection testing. The column was aligned accurately under the loading instrument and two pallet beam were then attached to the perforations of column with reversely positioned tabs on both left and right sides. In order to prevent the lateral twisting of pallet beams near the connection, the beams were adjusted into two rectangular hollow sections which were welded to angle sections and bolted to strong floor. Roller supports with a distance of 2 m between each other were provided for the unconnected ends of both the beams. A displacement controlled loading method was chosen and the force was applied at the top of the column through a 50 kN hydraulic actuator at a rate of 1 mm/min until the a drop of 1 kN in the load was observed or the connection showed no resistance to further load. Applying the load at the top of the column caused the top of the connection in compression and the bottom in tension. EN 15512 [23] suggests that the end rotation of beams can be evaluated through the inclinometers placed closer to the connection. Two digital inclinometers were placed as possible as close to the connection and the end the end rotation of beams was directly recorded. The deflection in beams was monitored by two dial gauges, placed at $L/4$ distance from the center of roller support. A dial gauge was attached to the column at its bottom, in order to record central deflection. The dial gauges were connected to a computerized data logger to record real time loading and displacements.

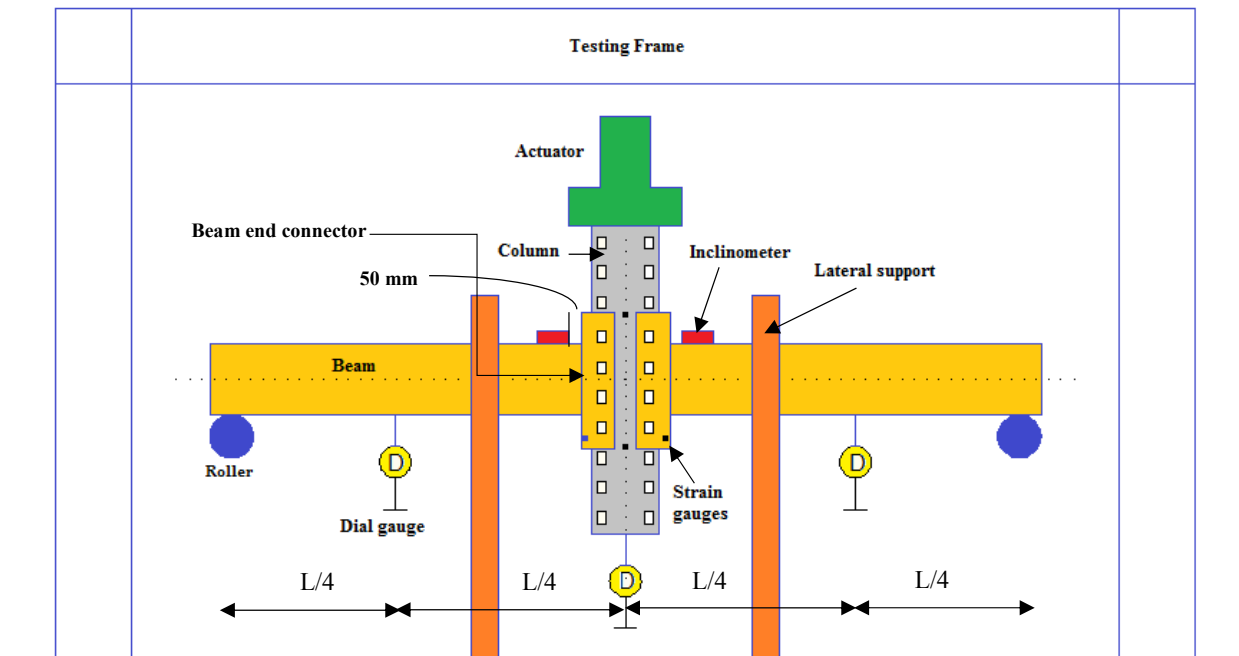


Figure 5. Schematic Diagram of Test Set-up

3. RESULTS AND DISCUSSION

3.1 M- θ Behavior and stiffness

All the specimens showed non-linear behavior from the start. This may be either due to the imperfections in the constructional design of the specimens or non-linear geometrical configurations [28]. Figure 6 shows the M- θ graphs for all six connections. It can be seen from Figure 6 that the decline in the moment capacity was occurred in the ultimate stage. It may be due to the complete rupture of top two tabs after sustaining a reasonable amount of load in its yield stage. The stiffness was calculated using Equal area method, however no correction factor was applied to the achieved moments; mainly due to the larger stiffness of the beam sections. Table 6 presents the test results for all six specimens.

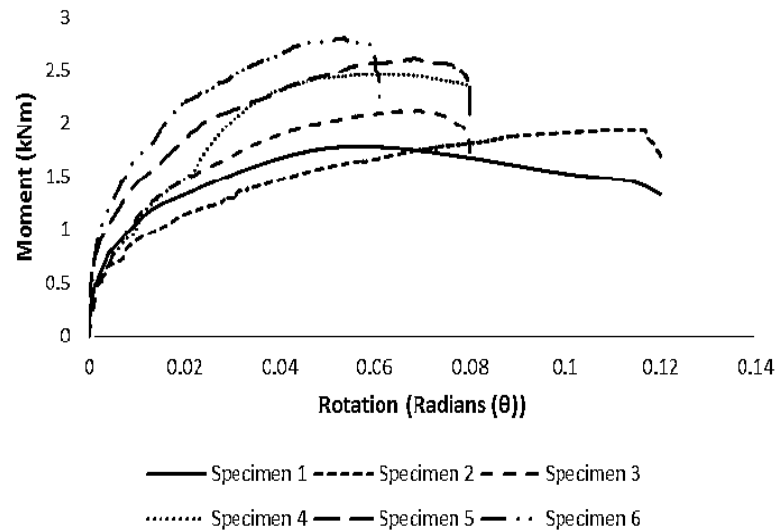


Figure 6. M- θ Curves for All Tested Specimens

Table 6. Test Results

Specimen	Failure Load (kN)	Ultimate Moment Capacity (kNm)	Rotation (Radians)	Stiffness (kNm/rad)
1	3.79	1.78	0.12	23.36
2	4.06	1.91	0.12	26.54
3	4.52	2.13	0.08	31.1
4	5.23	2.46	0.08	36.6
5	5.54	2.61	0.08	46.8
6	5.97	2.81	0.06	49.23

3.2 Failure Modes

The failure was considered when a drop of 1 kN was observed in the applied load. During the experimental testing, three types of failures were observed. These types included: (i) failure of connector tabs (ii) deformation of column, and (iii) distortion of the BEC itself. For specimen 1, with the increase in load, the top two tabs tried to come out from the column perforations, cut the column web and ruptured completely. The last tab did not cause any cut in the web and just came out from the column slot. The failure of specimen '2' was similar to the specimen '1', except the difference in the value of failure load. A considerable distortion of the BEC was also noticed. In the case of specimen '3', the greater number of tabs and increased thickness of the BEC allowed the specimen to sustain larger in-plane moment. No tab showed a complete rupture, however, the

failure initiated with the distortion of top tabs and ended with the distortion of column web caused by the cuts developed by the tabs. For specimens '4-6', the amount of failure load was extensively higher than specimens, '1-3' and the full rupture of any tab was not noticed. However, tearing of column was observed near the top tabs under compression. Overall, a ductile behavior was shown by almost all the specimens. The typical failure modes of the BEC, the connection and the column and are shown in Figure 7 (a-c), respectively.

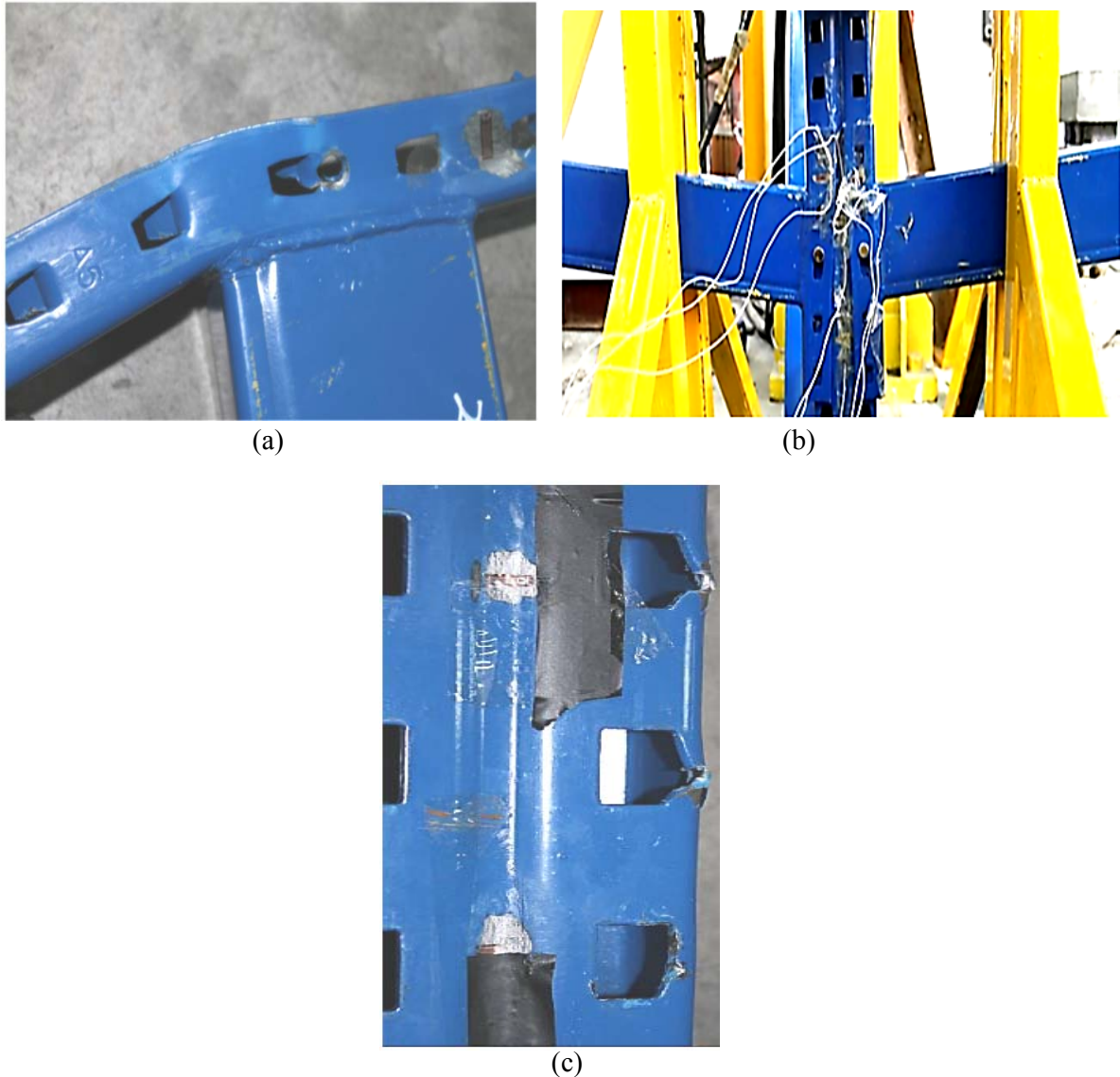


Figure 7. Failure Modes
(a) BEC, (b) connection, (c) column

4. EFFECT OF GEOMETRY OF THE BEC ON THE CONNECTION PERFORMANCE

The parameters analyzed in this study are the thickness of the BEC and number of tabs in the BEC. Figure 6 and Table 6 show that specimen 2 showed 7% higher moment capacity than specimen 1. The stiffness was increased by 12%. The similar behavior was observed when the thickness of BEC was changed from 2 mm to 6 mm. Specimen 3 showed 16% increased moment capacity as

compared to the specimen 1. A 24% increase in the stiffness was observed. These statistics clearly shows the effect of increased thickness of the BEC. When the number of tabs changed from 3 to 5 (from specimen 1 to specimen 4), the moment capacity and stiffness of specimen 4 were increased by 28% and 37%, respectively. This shows that in all the cases, the geometrical properties has affected the stiffness of the connection.

5. FINITE ELEMENT (FE) MODELING

5.1 Modeling Approach

A non-linear 3D FE model was developed on a commercially available software ABAQUS [29]. The FE model was capable of incorporating the geometrical and material non-linearity. The specimen 2 was considered for FE modeling and a bi-linear elasto-plastic model was developed based on the material properties defined in Table 1. The column, pallet beam and the BEC were modeled using Element C3D8R (i.e., continuum 3D with eight nodes and reduced integration). The number of elements in each beam/ BEC were 18812 whereas in column, the number of element was 46404. Distortion energy density criterion or von Mises yield criterion is used to predict yielding. It should be noted that the few of previous studies did not consider the modeling of tabs that hampers to obtain realistic modeling of the strength and deformation behavior of connector tabs which were the most crucial element of SPR BCCs. In this study, SOLID element was used to model the tabs. Although, modeling of tabs as solid element complexed the model, nevertheless, the original experimental conditions were replicated and helped in evaluating the actual deformation behavior of tabs. Figure 8 shows the geometry of modeled tabs.

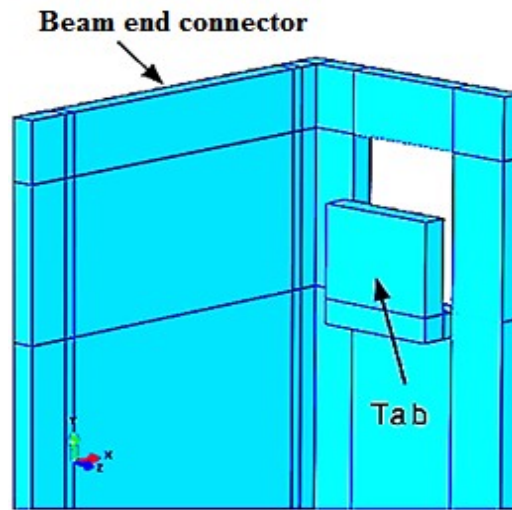


Figure 8. Geometry of Modeled Tabs

5.2 Surface Interaction

The surface-to-surface interactions (front and side) between the column and the BEC and the column and the tabs were assigned through tangential frictionless contact, and normal hard contact and tangential frictionless contact, respectively. The tangential frictionless contact removes the relative movement between the surfaces of the column and the tab, whereas the normal hard contact restrains the sideways movement (normal to longitudinal axes) of the column.

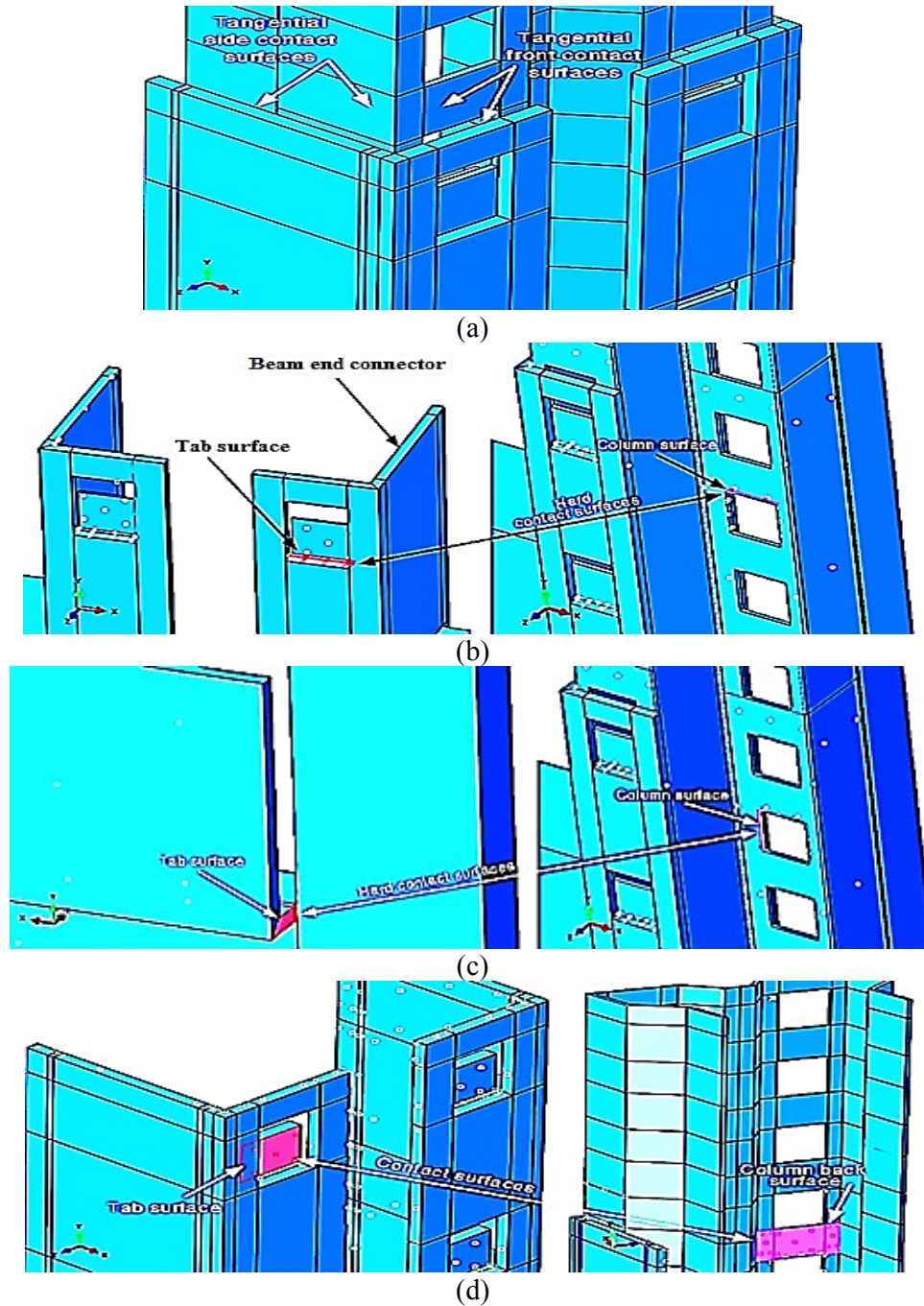


Figure 9. Surface to Surface Interaction Among Components

5.3 Loading and Boundary Conditions

Simulating the boundary conditions adopted in the experimental investigations, the following boundary conditions were modeled: $U_x = U_y = U_{Ry} = U_{Rz} = 0$, where U and U_R are the displacement and rotation, respectively. The boundary conditions assigned to the column were $U_x = U_z = U_{Rx} = U_{Ry} = U_{Rz} = 0$, where U_y is the applied displacement. The displacement loading was applied on the top of the column in 10,000 steps. The step size was further sub-divided, resulting in a displacement rate of 70×10^{-4} mm/sub-step size. This minor value avoids the influence of strain rate on the structural behavior of the assembly.

5.4 Meshing

A structured discretization scheme was employed to mesh the beams and BECs, and a structured free meshing scheme was adopted for the column because of its complex geometry. Experimental observations showed large deformations at the punching point of tabs with the BEC; hence, this region was assigned with a high-density mesh. Various types of non-linearity such as contact, geometric and material increased the convergence issues at some regions during simulation, however, this problem was successfully overcome by decreasing the time step size and enhancing the mesh density in those regions. Figure 10 shows the complete geometry of the modeled connection.

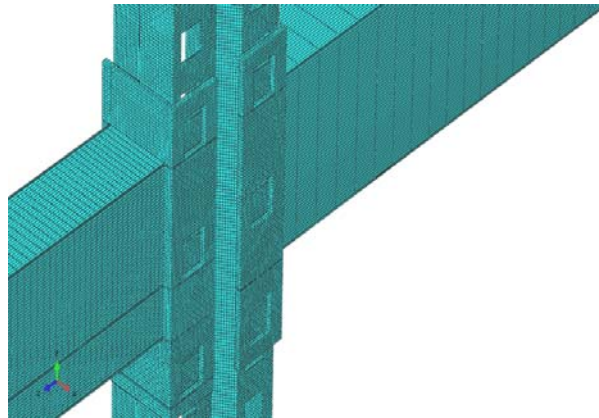


Figure 10. Complete Geometry of the Modeled Connection

5.5 FE Results

5.5.1 Failure modes

The failure modes showed by FE simulation were very much closer to the experimental failure modes. Again, the failure of tabs was the major failure mode showed by FE analysis. Similar to the experimental investigations, the bottom tabs of the connector showed high deformations and tried to cut the column perforations. The disengagement of tabs and distortion of column material were observed by FE model at a relatively lesser intensity as compared to the experimental results which, consequently, led to a higher ultimate moment capacity. The BEC showed noteworthy twist in the tension region. The FE failure of the BEC is illustrated in Figure 11. A closer look of the failure of bottom tab is presented in Figure 12. The deformation of the column is presented in Figure 13. It can be seen that the top and bottom tabs distorted the column slots. The failure of full connection is presented in Figure 14.

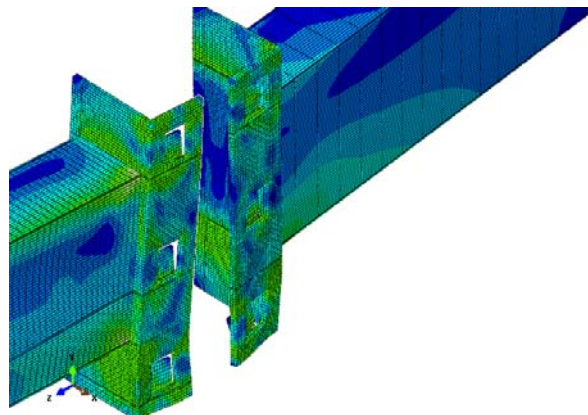


Figure 11. Failure of the Tabs and the Beam End Connector

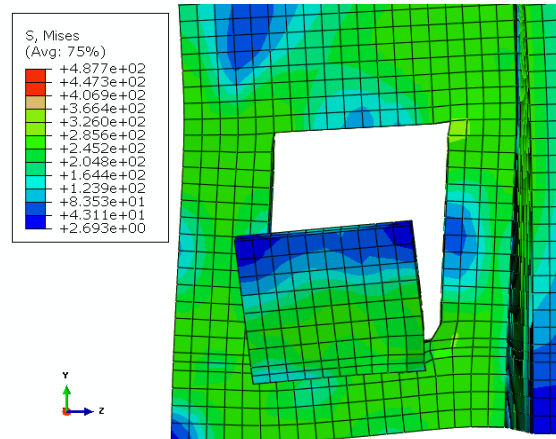


Figure 12. Failure of the Bottom Tab

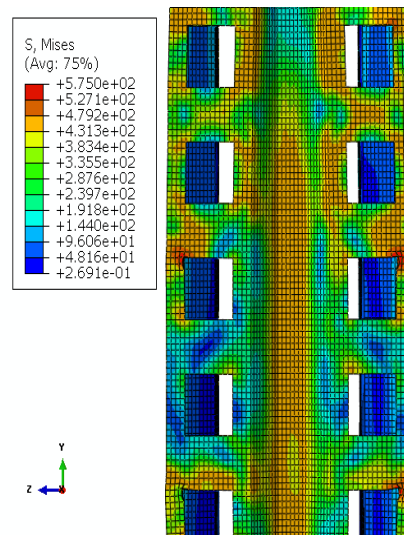


Figure 13. Failure of Column

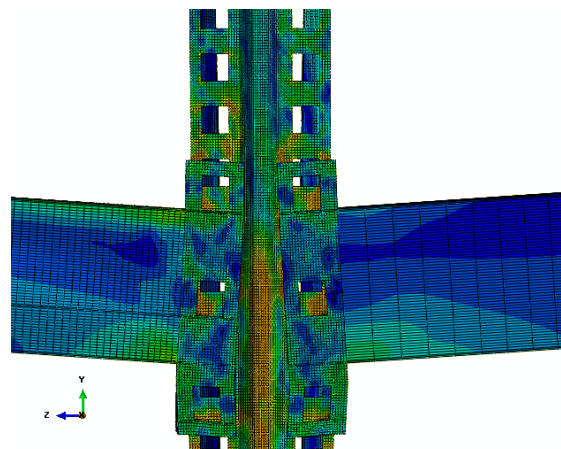
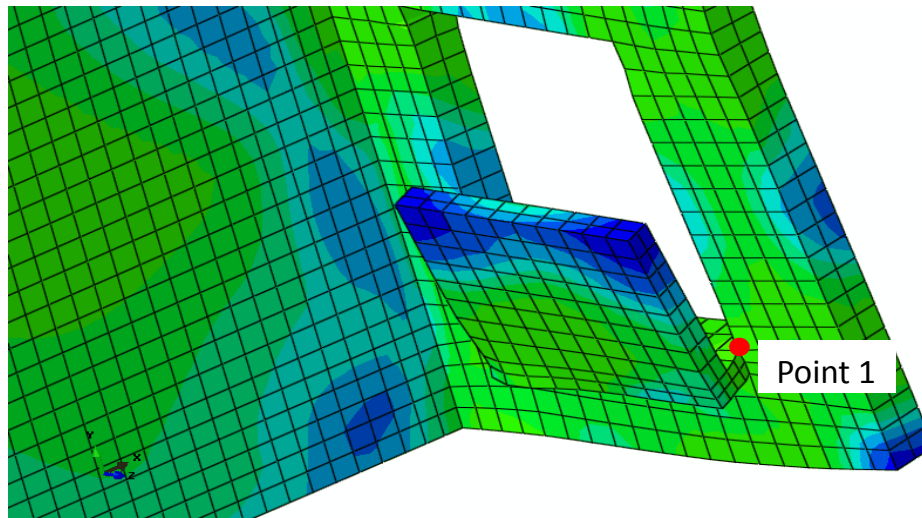


Figure 14. Failure of the Connection

5.5.1 Stress pattern

It can be observed from Figure 13 that the highest stress value in the column occurred in the tension region of BCC. Therefore, the tabs in third slot of the column experienced higher stress compared with those in the compression zone because of the chosen point of application of the load onto the column. This phenomenon substantiates the case of selecting the double cantilever test method for testing purpose. Furthermore, engaging the tabs reversely into the column slots generated higher stress concentration at the joining region of the tabs and the column.

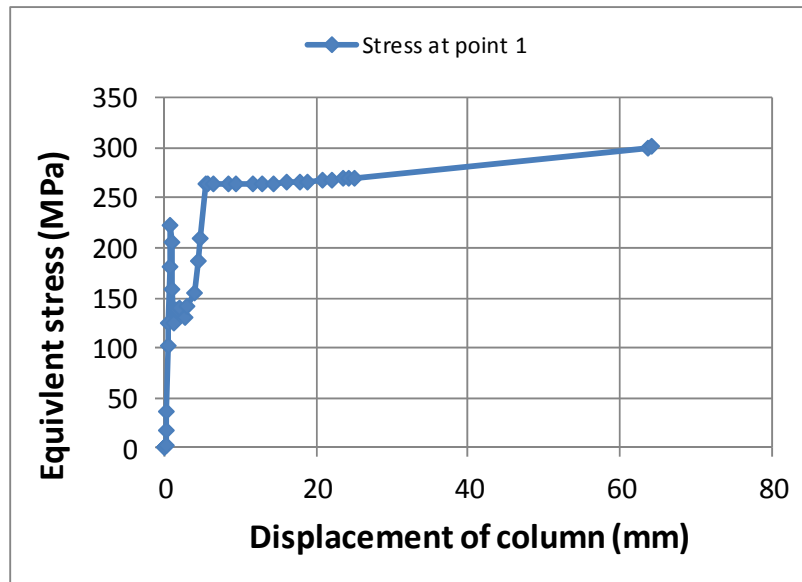
The Von Mises stress distribution at a specific point in the last tab in the tension zone is shown in Figure 15(a), while Figure 15(b) shows the variation of equivalent stress (Von Mises stress) at point 1 as shown in Figure 15(a) with respect to column vertical displacement. Point 1 is the upper joining point between tab and column. It is evident from Figure 15(b) that the equivalent stress reaches to 300 MPa which is the approximate yield strength (304 MPa) of beam end connector, as given in Table 1. This shows the permanent failure of tab due to excessive deformation. Furthermore, stress relaxation at the initial stage of deformation is observed. This could be happened due to slipping action between column surface and tab but at intermediate and higher stages of deformation, stress increment is observed due to significant deformation of tab. Stress magnitude is higher than yield strength, indicating that permanent deformation has occurred in the tabs.



(a) Stress distribution at a specific point in the last tab

5.5.2 Moment-rotation ($M-\theta$) behavior

A higher level of similarity was noticed between the FE and experimental $M-\theta$ behavior of the BCCs. The FE model was able to predict the experimental behavior to a large extent. The initial stiffness portion of the curve matches that of the test results well. However, a minor variation was observed between the failures of column perforations exhibited by the experimental and FE investigations. In the test, failure occurred with the tearing of column perforation by the lower tabs. The tabs slit the column wall. Meanwhile, the FE model was unable to consider the same intensity of distortion of column slots. Therefore, the connection's ultimate moment capacity obtained by using the FE model was higher than that obtained from the test. A comparison of the $M-\theta$ graphs plotted for specimens 2 for both experimental and FE investigations is provided in Figure 16. Table 7 shows a comparison of the moment capacity and stiffness of the experimental and FE investigations.



(a) Equivalent stress and column displacement graph

Figure 15. Von Mises Stress Distribution in the Tab in the Tension Zone

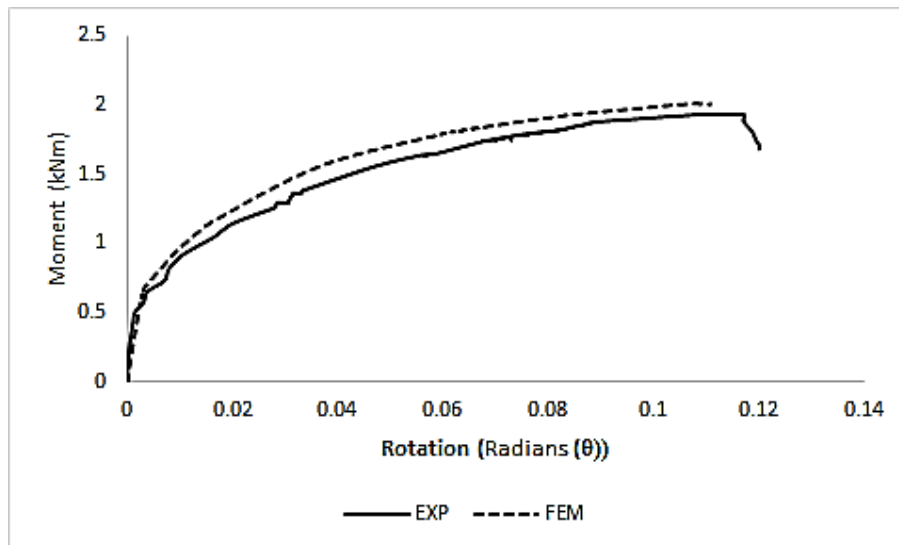
Figure 16. Experimental and FEM Comparison of the M- θ Graphs for Specimens 2

Table 7. Comparison of the Moment Capacity and Stiffness of the Experimental and FE Investigations for Specimen 2

Specimen	Ultimate Moment capacity (kNm)		Stiffness (kNm/rad)	
	Experimental	FEM	Experimental	FEM
2	1.91	2.01	26.54	27.42

6. CONCLUSION

The variation in the geometrical features of the commercially available BECs used in the SPR BCCs is the major hurdle in the development of a generalized analytical approach to predict the M- θ relationship for SPR BCCs. The main contribution of this study is twofold: (1) to identify the effect of the geometry of the BEC on the strength and stiffness of SPR BCCs (ii) to identify the possible failure modes of steel rack connections. A series of experiments was performed by varying the thickness of the BEC and number of tabs in the BEC. FE simulations were performed and their results were validated against experimental findings. The FE model showed a good agreement with experimental results. It was revealed by the experimental findings that the failure of all the specimens was originated due to the distortion of tabs which promoted the unbalanced stress concentration in the column perforation and consequently, into the beams. The tearing of column material and the twist in the BEC for the specimens with relatively lesser thickness and lesser number of tabs in the BEC was observed. The influence of parameters was also investigated. A comparison of the achieved M- θ relationship showed that the number of tabs is more critical factor than the connector thickness for the overall performance of SPR BCCs.

ACKNOWLEDGEMENT

The study presented herein was made possible by the University of Malaya Grants: (i) UMRG RP004C-13AET and, (ii) PPP grant PG055-2013B. The authors would like to acknowledge the support.

REFERENCES

- [1] Pekoz, T. and Winter, G., "Cold-Formed Steel Rack Structures", Proceedings of Second Specialty Conference on Cold-Formed Steel Structures. USA, 1973.
- [2] Ślęczka, L. and Kozłowski, A., "Experimental and Theoretical Investigations of Pallet Racks Connections", *Advanced Steel Construction*, 2007, Vol. 3, No. 2, pp. 607-610.
- [3] Sajja, S., Beale, R.G. and Godley, M.H.R., "Shear Stiffness of Pallet Rack Column Frames", *Journal of Constructional Steel Research*, 2008, Vol. 64, pp. 867-874.
- [4] Moen, C.D. and Schafer, B., "Elastic Buckling of Cold-formed Steel Columns and Beams with Holes", *Engineering Structures*, 2009, Vol. 31, pp. 2812-2824.
- [5] Kozłowski, A. and Ślęczka, L., "Preliminary Component Method Model of Storage Rack Joint", *Proceedings of Connections in Steel Structures V. Amsterdam*, 2004, pp. 253-262.
- [6] Gilbert, B.P. and Rasmussen, K.J.R., "Experimental Test on Steel Storage Rack Components", *Research Report No R899*, University of Sydney, Australia, 2009.
- [7] Al-Jabri, K.S., Burgess, I.W., Lennon, T. and Plank, R.J., "Moment-rotation-temperature Curves for Semi-rigid Joints", *Journal of Constructional Steel Research*, 2005, Vol. 61, No. 3, pp. 281-303.
- [8] Al-Jabri, K.S. and Al-Alawi, S.M., "Predicting the Behaviour of Semi-rigid Joints in Fire Using an Artificial Neural Network", *Steel Structures*, 2007, Vol. 7, pp. 209-217.
- [9] Lee, Y.H., Tan, C.S., Mohammad, S., Md Tahir, M. and Shek, P.N., "Review on Cold-formed Steel Connections", *The Scientific World Journal*, 2014.
- [10] Ali, B. A., Saad, S., Osman, M. H. and Ahmad, Y., "Finite Element Analysis of Cold-formed Steel Connections", *International Journal of Engineering*, 2011, Vol. 5, No. 2, pp. 55-61.
- [11] Markazi, F.D., Beale, R.G. and Godley, M.H.R., "Experimental Analysis of Semi-rigid Boltless Connectors", *Thin-walled structures*, 1997, Vol. 28, No. 1, pp. 57-87.

- [12] Markazi, F.D., Beale, R.G. and Godley, M.H.R., "Numerical Modelling of Semi-rigid Boltless Connectors", *Computers & Structures*, 2001, Vol. 79, pp. 2391-2402.
- [13] Bernuzzi, C. and Castiglioni, C.A., "Experimental Analysis on the Cyclic Behaviour of Beam-to-column Joints in Steel Storage Pallet Racks", *Thin-Walled Structures*, 2001, Vol. 39, pp. 841-859.
- [14] Filiatrault, A., Bachman, R.E. and Mahoney, M.G., "Performance-based Seismic Design of Pallet-type Steel Storage Racks", *Earthquake spectra*, 2006, Vol. 22, pp. 47-64.
- [15] Filiatrault, A., Higgins, P.S., Wanitkorkul, A. and Courtwright, J., "Experimental Stiffness of Pallet-Type Steel Storage Rack Teardrop Connectors", *Practice Periodical on Structural Design and Construction*, 2007, Vol. 12, No. 4, pp. 210-215.
- [16] Sideris, P., Filiatrault, A., Leclerc, M. and Tremblay, R., "Experimental Investigation on the Seismic Behavior of Palletized Merchandise in Steel Storage Racks", *Earthquake Spectra*, 2010, Vol. 26, pp. 209-233.
- [17] Zhao, X., Wang, T., Chen, Y. and Sivakumaran, K.S., "Flexural Behavior of Steel Storage Rack Beam-to-column Connections", *Journal of Constructional Steel Research*, 2014, Vol. 99, pp. 161-175.
- [18] Castiglioni, C. A., *Seismic Behavior of Steel Storage Pallet Racking Systems*, Springer 2016.
- [19] Shah, S. N. R., Sulong, N.H. R., Shariati, M., Khan, R. and Jumaat, M.Z., "Behavior of Steel Pallet Rack Beam-to-column Connections at Elevated Temperatures", *Thin-Walled Structures*, 2016, Vol. 106, pp. 471-483.
- [20] Shah, S.N.R., Sulong, N.H.R., Shariati, M. and Jumaat, M.Z., "Steel Rack Connections: Identification of Most Influential Factors and a Comparison of Stiffness Design Methods", *PLOS One*, 2015, Vol. 10, No. 10, e0139422.
- [21] Shah, S.N.R., Sulong, N.H.R., Khan, R., Shariati, M. and Jumaat, M.Z., "Behavior of Industrial Steel Rack Connections", *Mechanical Systems and Signal Processing*, 2016, Vol. 70-71, pp. 716-725.
- [22] Rack Manufacturers Institute (RMI), *Specification for the Design, Testing and Utilization of Industrial Steel Storage Racks*, Material Handling Industry, MH16.1. Charlotte, NC, 2012.
- [23] EN 15512. *Steel Static Storage Systems—Adjustable Pallet Racking Systems—Principles for Structural Design*, European Committee for Standardization. Brussels, Belgium, 2009.
- [24] AS4084, *Standards Australia. Steel Storage Racking*, Sydney, Australia, 2012.
- [25] Bajoria, K.M. and Talikoti, R.S., "Determination of Flexibility of Beam to Column Connectors used in Thin Walled Cold Formed Steel Pallet Racking Systems", *Thin Walled Structures*, 2006, Vol. 44, pp. 372-380.
- [26] Sangle, K.K., Bajoria, K.M. and Talicotti, R.S., "Stability and Dynamic Analysis of Cold-formed Storage Rack Structures with Semirigid Connections", *International Journal of Structural Stability and Dynamics*, 2011, Vol. 11, No. 6, pp. 1059-1088.
- [27] Prabha, P., Marimuthu, V., Saravanan, M. and Jayachandran, S.A., "Evaluation of Connection Flexibility in Cold Formed Steel Racks", *Journal of Constructional Steel Research*, 2012, Vol. 66, No. 7, pp. 863-872.
- [28] Shah, S. N. R., Sulong, N. R., Jumaat, M. Z. and Shariati, M., "State-of-the-art Review on the Design and Performance of Steel Pallet Rack Connections", *Engineering Failure Analysis*, 2016, Vol. 66, pp. 240-258.
- [29] ABAQUS Software Version 6.11 2012. Dassault Systems

THERMAL MODELLING OF LOAD BEARING COLD-FORMED STEEL FRAME WALLS UNDER REALISTIC DESIGN FIRE CONDITIONS

A.D. Ariyanayagam, P. Keerthan and M. Mahendran *

Science and Engineering Faculty, Queensland University of Technology, Brisbane, Australia

**(Corresponding author: E-mail: m.mahendran@qut.edu.au)*

Received: 14 August 2015; Revised: 9 June 2016; Accepted: 12 July 2016

ABSTRACT: Cold-formed Light gauge Steel Frame (LSF) walls lined with plasterboards are increasingly used in the building industry as primary load bearing components. Although they have been used widely, their behaviour in real building fires is not fully understood. Many experimental and numerical studies have been undertaken to investigate the fire performance of load bearing LSF walls under standard fire conditions. However, the standard fire time-temperature curve given in ISO 834 [1] does not represent the fire load present in typical modern buildings that include considerable amount of thermoplastic materials. Some of these materials with high in calorific values increase the fire severity beyond that of the standard fire curve. Fire performance studies of load bearing LSF walls exposed to realistic design fire curves have also been limited. Therefore in this research, finite element thermal models of LSF wall panels were developed to simulate their fire performance using the recently developed realistic design fire time-temperature curves [2]. Suitable thermal properties were proposed for plasterboards and insulations based on laboratory tests and available literature. The developed finite element thermal models were validated by comparing their thermal performance results with available realistic design fire test results, and were then used in a detailed parametric study. This paper presents the details of the developed finite element thermal models of load bearing LSF wall panels under realistic design fire time-temperature curves and the results. It shows that finite element thermal models of LSF walls can be used to predict the fire performance including their fire resistance rating with reasonable accuracy for varying configurations of plasterboard lined LSF walls exposed to realistic design fire time-temperature curves.

Keywords: Numerical studies, Light gauge steel frame (LSF) walls, realistic design fire time-temperature curves, load bearing walls, cold-formed steel structures, gypsum plasterboard, specific heat, thermal conductivity, mass loss (relative density)

DOI: 10.18057/IJASC.2017.13.2.5

1. INTRODUCTION

Light gauge Steel Frame (LSF) walls are usually made of cold-formed steel studs, and are lined with gypsum plasterboard layers on both sides with and without cavity insulations (Figure 1). Cold-formed steel stud sections in LSF walls panels when exposed to fire heat up quickly resulting in fast reduction in their strength and stiffness. Hence the studs are commonly lined with plasterboard and insulation materials as fire protecting materials. These lining materials protect steel studs during building fires by delaying the temperature rise. The wall configurations include single and double layers of plasterboard lined walls with and without insulation. Insulated wall panels can be either cavity insulated or externally insulated, i.e. a thin insulation layer sandwiched between two plasterboards.

The types and thickness of plasterboard and insulation layers used will significantly influence the fire resistance ratings (FRR) of LSF wall panels. Plasterboard types include specially manufactured fire resistant gypsum plasterboards or the general purpose plasterboards in thicknesses ranging from 8 to 16 mm. Currently, gypsum plasterboard lined LSF wall systems are increasingly used in low-rise and multi-storey buildings, but without a full understanding of their fire performance.

Similarly insulation type includes rock fibre, glass fibre or cellulose fibre in different thicknesses and densities. All these materials have a significant impact on the performance of LSF wall panels when subjected to fire from one side as they delay the temperature rise of thin-walled LSF wall studs.

Many experimental and numerical studies have been undertaken to investigate the fire performance of load bearing LSF walls under standard fire conditions [1]. However, it is questionable whether it truly represents the fire scenarios in modern buildings. In reality, modern residential and commercial buildings incorporate both traditional wooden items and modern items such as cushion/fabric furniture, mattresses, fabric coated partitions, etc., which make use of thermoplastic materials including synthetic foams and fabrics. During a fire, some of these thermoplastic materials melt and flow to the floor and burn significantly faster, with higher heat release rates, than the standard fire curve used to obtain FRR, thus increasing the fire severity [2]. This means LSF walls may not provide safe evacuation, or offer the required life safety for occupants and fire rescuers. Therefore suitable realistic design fire time-temperature curves were developed and full scale fire tests of load bearing LSF walls were conducted by Ariyanayagam and Mahendran [2,4]. Type-K cable thermocouples were used to measure the temperatures across and along the LSF wall panels. Their study has shown that LSF wall studs failed when they reached their critical maximum hot flange temperatures and if similar conditions exist, LSF wall panel failure mainly depends on stud hot flange temperature. However, their experimental study was limited to six realistic design fire time-temperature curves including both rapid and prolonged fires. Hence to investigate the fire performance of LSF wall systems for a range of different fire scenarios, finite element thermal models were developed and used in a detailed study. This paper presents the details of the finite element thermal analyses of load bearing LSF walls exposed to realistic design fire time-temperature curves. It includes the details of the developed finite element thermal models of load bearing LSF wall panels and the results. Most importantly, it describes the thermal performance of LSF wall systems exposed to a range of realistic design fire time-temperature curves.

2. THERMAL BEHAVIOUR OF LOAD BEARING LSF WALLS USING EXPERIMENTAL STUDIES

Six full scale fire tests were conducted on 2400 mm x 2100 mm LSF wall panels to investigate the structural and thermal performance of load bearing LSF wall panels exposed to realistic design fire time-temperature curves [4]. LSF wall panels consisted of four cold-formed steel lipped channel sections (90 x 40 x 15 x 1.15 mm) spaced at 600 mm centres and tracks (top and bottom) made of unlipped channel sections (92 x 50 x 1.15 mm). Both studs and tracks of 2400 mm length were fabricated from 1.15 mm galvanized steel sheets having a minimum yield strength of 500 MPa (G500 Steel). Test specimens were built by lining the steel frames with one or two layers of 16 mm thick Firestop™ gypsum plasterboards manufactured by Boral Plasterboard, Australia (Figure 1). The 25 mm thick ROXUL Stonewool MPS400 Rock fibre insulation was used in externally insulated wall panels. Tests were conducted using the recently developed realistic design fire curves [2] shown in Figure 2. They were based on Eurocode Parametric [3] and Barnett's 'BFD' [5] fire curves with appropriate compartment characteristics. Details of the development of these realistic design fire curves are given in Ariyanayagam and Mahendran [2].

Fire tests were conducted in a specially designed test rig shown in Figure 3. Test specimen was placed with the stud centroids aligning with those of four loading plates and hydraulic rams. The wall studs were first loaded in axial compression using these hydraulic rams attached to a single pump via loading plates. This pre-determined axial compression load was based on the required

load ratios of 0.2 and 0.4. It was 15 kN for Tests LSF1 to LSF4 and 30 kN for Tests LSF5 and LSF6. Following the load application, one face of the test wall specimen was exposed to heat in a propane-fired vertical gas furnace while maintaining the applied load. During the tests time-temperature profiles at various locations across the specimen thickness were measured using thermocouples.

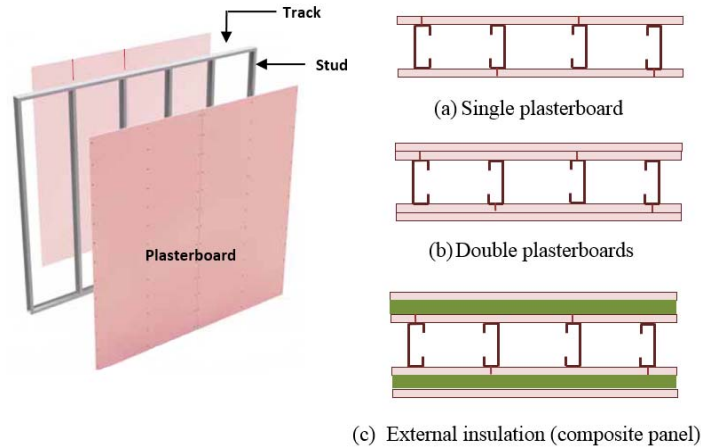


Figure 1. LSF Wall Panels

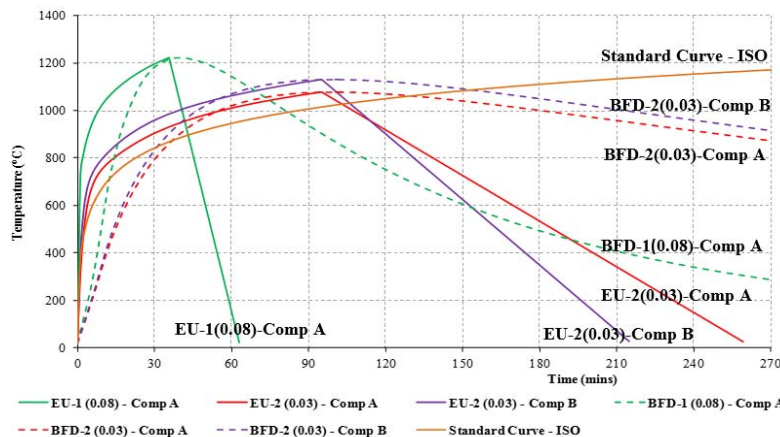


Figure 2. Realistic Design Fire Time-Temperature Curves Used in Fire Tests [2]

Table 1 shows the details of tested LSF walls and their failure times. It highlights that some realistic design fires (Tests LSF3 to LSF6) can cause severe damage to LSF wall panels than the standard fire [1] while other realistic design fire time-temperature curves (Tests LSF1 and LSF2) are not as severe as the standard fire. Ariyanayagam and Mahendran [4] provide a full description of the full scale fire tests conducted for three different LSF wall configurations and the results. Experimental studies showed that in all the fire tests structural failure of studs initiated the wall failure instead of insulation or integrity failure, except for Test Specimen LSF1 that did not fail even after 180 minutes of fire exposure. No significant differences were observed between the two different fire curves used in the tests [4]. In the initial stages of the fire, studs simply followed the shape of the fire time-temperature curve and after the calcination of gypsum plasterboard, stud temperatures increased rapidly and led to the failure of LSF wall panel. The presence of wall lining material significantly influenced the failure times of single plasterboard lined walls as the plasterboard fall-off led to higher furnace temperature exposure and loss of lateral restraint to studs. This study also showed that if similar conditions exist, i.e. restraints and applied loads are similar, LSF wall panel failure depends mainly on the maximum stud hot flange temperature [4].

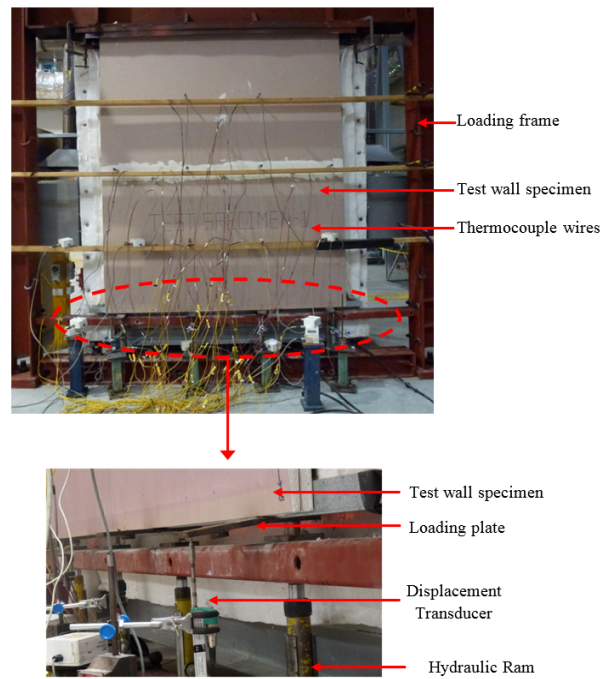
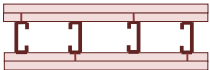
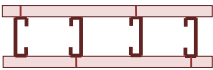
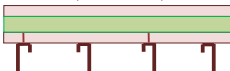


Figure 3. Fire Test Set-up [4]

Table 1. Test LSF Wall Configurations and Failure Times [4]

Test	LSF Wall Configuration	Insulation Type	Fire Curve	Failure Time (mins)
LSF1	Double layers of plasterboards (LR=0.2)	-	EU-2(0.03)-Comp A	No Failure
LSF2			BFD-2(0.03)-Comp A	139
Gunalan et al. [21]			ISO 834 [1]	111
LSF3	Single layer of plasterboard (LR=0.2)	-	EU-1(0.08)-Comp A	28
LSF4			BFD-1(0.08)-Comp A	39
Gunalan et al. [21]			ISO 834 [1]	53
LSF5	Externally insulated panel (LR=0.4)	Rock Fibre	BFD-2(0.03)-Comp B	118
LSF6			EU-2(0.03)-Comp B	120
Gunalan et al. [21]			ISO 834 [1]	134

Note: LR – Load ratio, the ratio between the applied axial compression load to the test ultimate capacity of the stud at ambient temperature.

3. THERMAL BEHAVIOUR OF LOAD BEARING LSF WALLS USING NUMERICAL STUDIES

This section presents the details of numerical studies into the thermal behaviour of tested load bearing LSF wall panels exposed to realistic fire time-temperature curves and their results. Recently many numerical heat transfer models have been developed and used by researchers [6-10]. Also there are many general finite element analysis programs that can be used for thermal analyses. The finite element model employed in this study to predict the thermal behaviour of load bearing LSF wall panels was based on SAFIR Version 2004 [11] while GID Version 10.0.1 was used as pre and post-processors.

Finite element program SAFIR was used to study the two-dimensional (2D) heat transfer analysis of cold-formed light gauge steel frame walls lined with gypsum plasterboards exposed to realistic design fire curves. Most of the earlier thermal models were based on one-dimensional (1D) heat transfer analysis using mathematical models exposed to standard fire curve. SAFIR used in this study accommodates the use of various elements to accurately simulate material response and stress-strain behaviour. 2D analysis is undertaken by SAFIR with triangular (3 node) or quadrilateral (4 node) solid elements. In SAFIR, heat transfer within a body of elements is modelled through conduction, whereas heat transfer from boundary elements is modelled with both convection and radiation transfer modes.

SAFIR has some limitations in its ability to model gypsum plasterboard assemblies. Ablation has the effect of reducing the cross-sectional thickness of gypsum plasterboard and hence increasing the heat flux across the plasterboard. SAFIR does not allow the user to eliminate any elements from the section to simulate ablation. Hence ablation process must be taken into account through the use of suitable apparent thermal properties of plasterboard. Modelling moisture movement across the cavity is a complex problem and it only influences heat transfer across the cavity at low temperatures [12]. Also as it is not incorporated in SAFIR, this process is neglected in this study. To investigate the thermal performance of load bearing LSF walls under realistic design fire curves, finite element models of tested wall panels [4] were developed. Figure 4 shows the developed finite element models of LSF walls under realistic fire curves. These models were validated using the fire test results of load bearing LSF walls exposed to realistic design fire time-temperature curves [4].

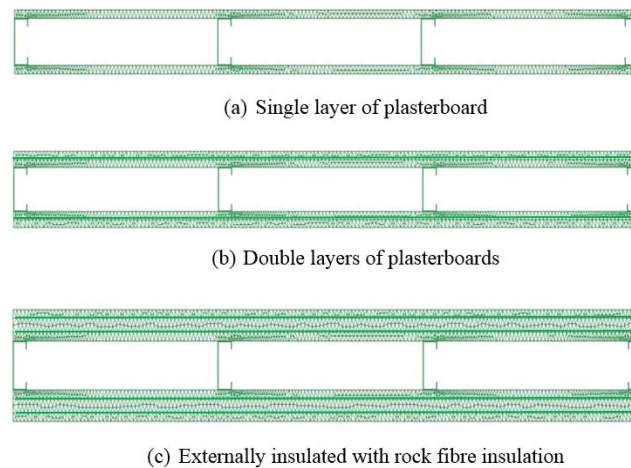


Figure 4. Finite Element Modelling of LSF Wall Panels

3.1 Thermal Boundary Conditions

The heat flux at the LSF wall boundary conditions was computed from the temperature of the fire curve T_g and the temperature on the surface T_s based on Equation (1).

$$q = h(T_g - T_s) + \sigma \varepsilon (T_g^4 - T_s^4) \quad (1)$$

where

q - Total heat flux

ε - Relative emissivity

σ - Stefan–Boltzmann constant ($5.67\text{E}-08\text{W/m}^2/\text{K}^4$)

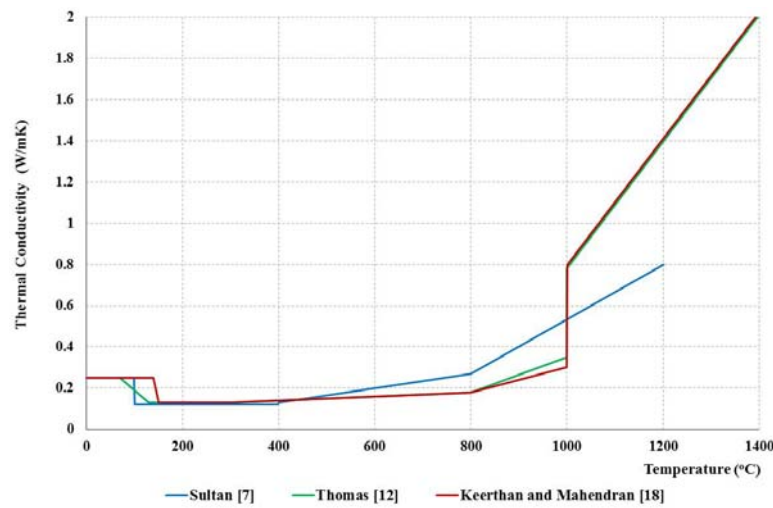
T_g and T_s - Gas and surface temperatures

In this study convective heat transfer coefficients (h) of 25 and 10 $\text{W/m}^2\text{K}$ [13-16] were used on the fire exposed and unexposed sides, respectively. Emissivity of 0.9 was used for the fire exposed surface [13,15,16]. A finite element mesh size of 2 mm was used in this study (Figure 4). This mesh size was selected based on the convergence studies undertaken by Keerthan and Mahendran [13] for similar conditions. The study showed that finite element models with a 2 mm mesh produced results that were closer to fire test results. Hence it was assigned to the plasterboard, and an automatic mesh generation was used in developing finite element models. In the numerical model three voids were created and the heat transfer in the cavities (void) was defined by radiation and convection between the boundaries of the cavity.

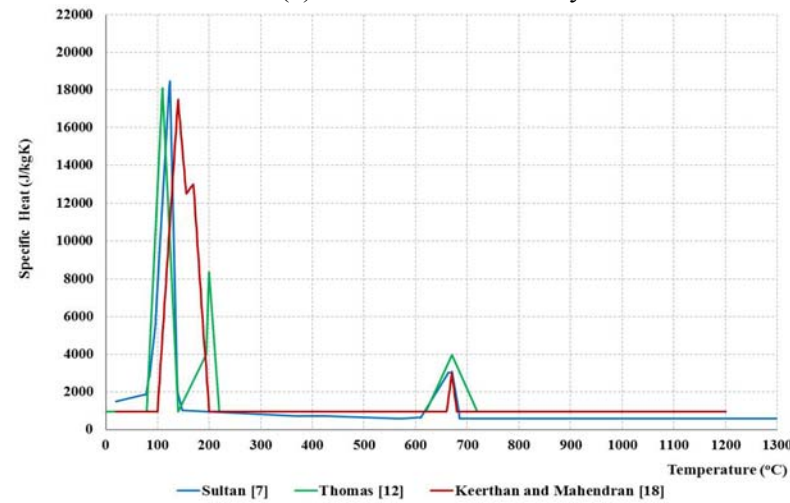
3.2 Thermal Properties of LSF Wall Components

In order to develop appropriate finite element thermal models to study the behaviour of LSF walls at elevated temperatures, accurate thermal properties of LSF wall components are needed. Thermal property values include thermal conductivity, specific heat and mass loss (relative density). The values at elevated temperatures for LSF wall components are summarized by Keerthan and Mahendran [13,15] based on a series of experimental results [15] and past research studies [6-10] for Australian gypsum plasterboards and rock fibre insulation materials. Hence these values are used in this study.

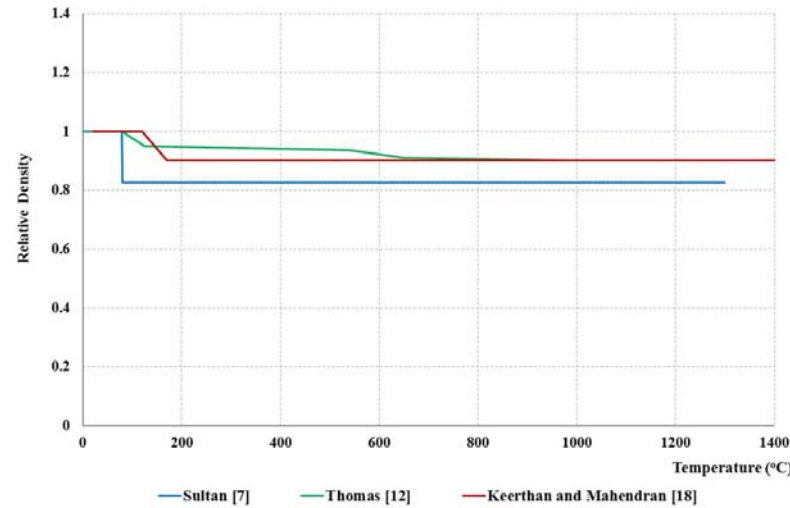
Initially, a finite element model of gypsum plasterboard was developed using finite element analysis software, SAFIR. The time-temperature curves across the plasterboard were then obtained and validated with fire test results [17] conducted for the standard fire curve [1]. This study was then extended [13] to thermal analysis of LSF wall panels lined with single and double layers of plasterboards, and cavity and externally insulated LSF wall panels, based on which suitable thermal property values for gypsum plasterboard and insulation were proposed (Figures 5 and 6). These finite element models were also validated using fire test results in [16] and are reported in [13]. A good agreement was obtained with fire test results (time-temperature curves) for LSF walls exposed to a standard fire curve, considering the complexity of gypsum plasterboard behaviour affected by processes such as ablation of plasterboards and migration of moisture into the cavity. These processes were taken into account by considering suitable values for the thermal conductivity of gypsum plasterboard [19]. Details of this process and the proposed values for specific heat, thermal conductivity and mass loss (relative density) are reported in [13,15,16]. Hence these thermal property values were used in this research for gypsum plasterboard and insulation materials to study the behaviour of LSF wall panels exposed to realistic design fire curve while cold-formed steel stud thermal properties were based on Eurocode 3 Part 1.2 [18].



(a) Thermal conductivity



(b) Specific heat



(c) Relative density

Figure 5. Thermal Properties of Gypsum Plasterboard versus Temperature

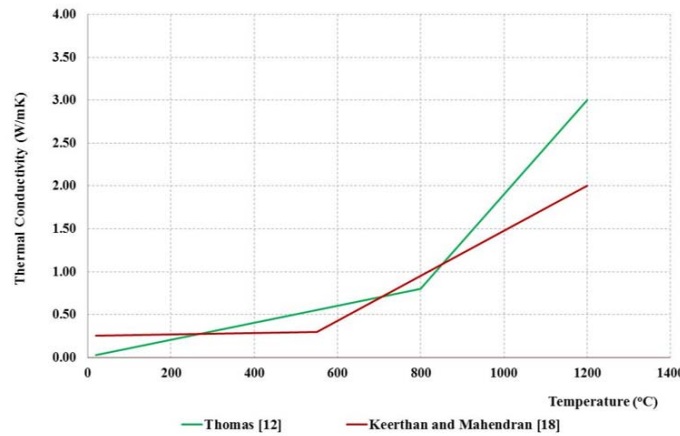


Figure 6. Thermal Conductivity of Rock Fibre Insulation versus Temperature

3.3 Comparison of Finite Element Thermal Analysis Results with Fire Test Results

Finite element thermal analysis results were compared with corresponding results from the realistic design fire tests conducted by Ariyanayagam and Mahendran [4]. Figure 7 shows the temperature distributions across the cross-section of LSF walls lined with double layers of plasterboard, whereas Figures 8 to 10 show stud time-temperature curves for the three wall configurations considered in this study. Average time-temperature curves of studs were used from the fire tests in these comparisons. The comparisons show a reasonable agreement between the fire test and finite element analysis (FEA) results for single and double layers of plasterboard lined LSF walls. The variation in stud temperatures was less than 50°C for double plasterboard lined LSF walls with a better agreement for Test LSF1 than Test LSF2 (Figure 8). The single plasterboard lined specimens also showed a temperature difference of less than 50°C between fire test and FEA results (Figure 9). The differences between the stud temperatures obtained from fire tests and FEA are relatively high for LSF wall specimens with external insulation (Figure 10). Finite element analyses overestimated the stud temperatures in this case. This could be due to the influence of rock fibre insulation as it is the new material used in the externally insulated walls other than in single and double plasterboard lined walls. As mentioned earlier, the same rock fibre insulation thermal property values used with the standard fire tests were used in the simulation of realistic design fire tests. Thermal property values of rock fibre insulation were idealized by Keerthan and Mahendran [15] based standard fire test results from [21, 22]. But these values do not appear to provide a good agreement for realistic design fire time-temperature curves. This could be due to the variation in rock fibre insulation thermal properties.

Load bearing LSF walls exposed to fires are also affected by processes such as ablation of plasterboard and insulation, migration of moisture vapours and penetration of cool ambient air or hot furnace gases into the cavity. Effects of these processes were taken into account in the models through the use of suitable thermal conductivity values for plasterboards and insulations. Although they have been considered by using apparent thermal properties values, these effects could vary with wall configurations and rate of heating. The different rate of fire temperature rise in the realistic design fire time-temperature curves influenced the stud temperatures as a result of changes to the gypsum plasterboard and rock fibre insulation thermal properties. Also gypsum plasterboard and rock fibre insulation are non-homogenous materials.

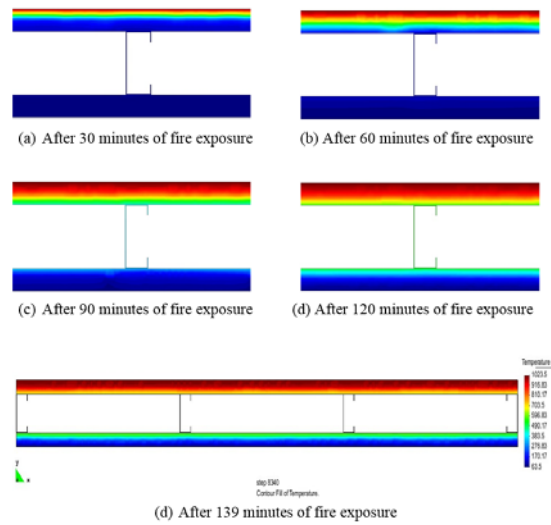
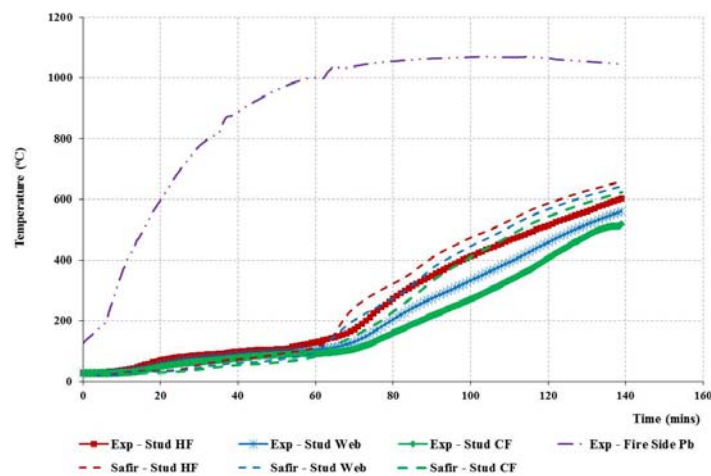
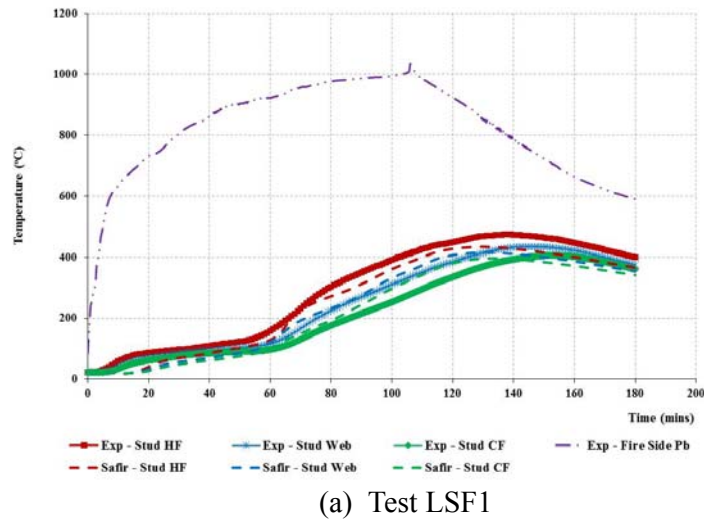
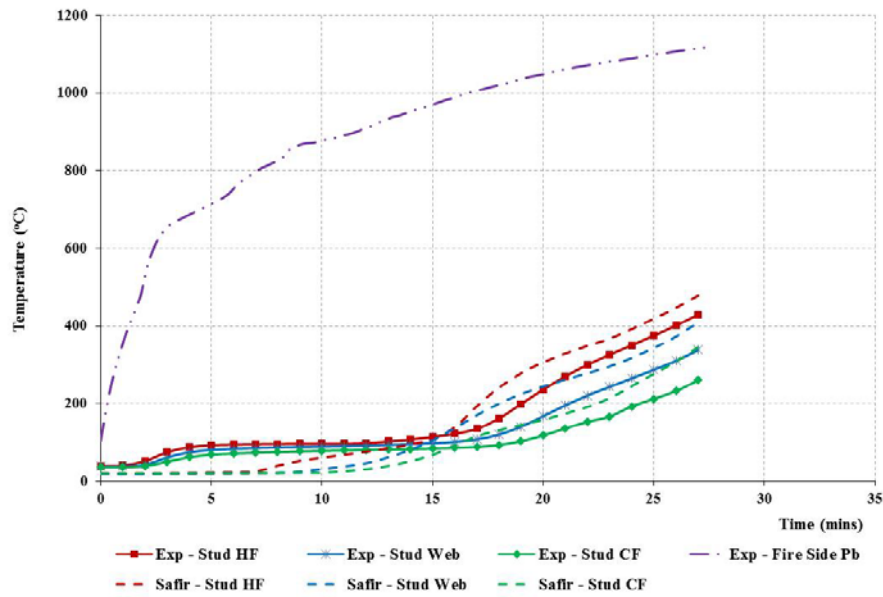


Figure 7. Temperature Distribution of Double Layers of Plasterboard Lined LSF Wall - Test Specimen LSF2

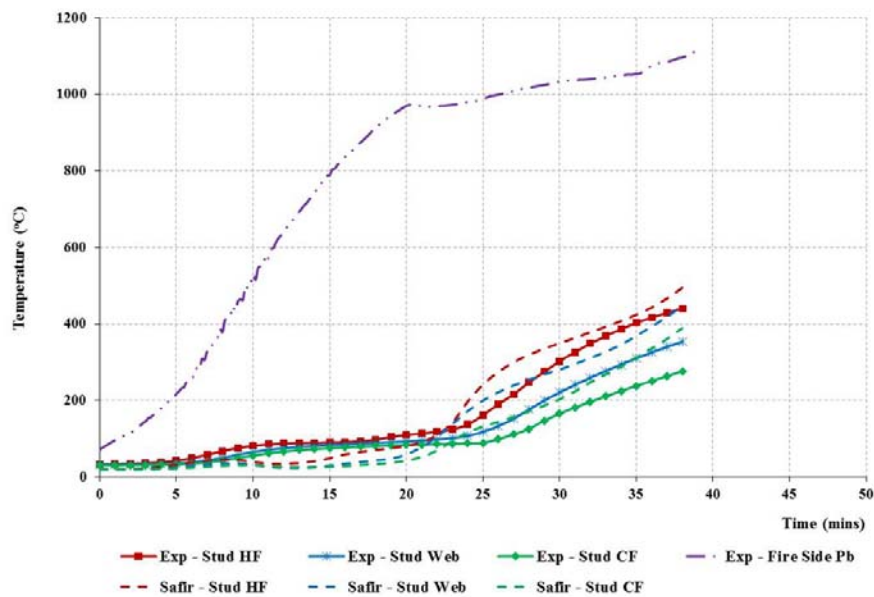


Note: HF: Hot flange; CF: Cold flange.

Figure 8. Stud Time-Temperature Curves from Fire Tests and Thermal Analyses for LSF Walls Lined with Double Layers of Plasterboards



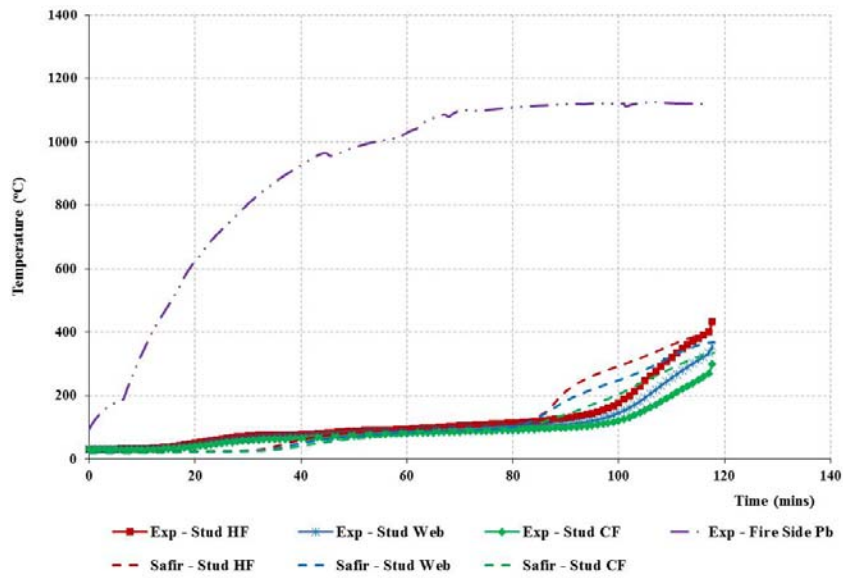
(a) Test LSF3



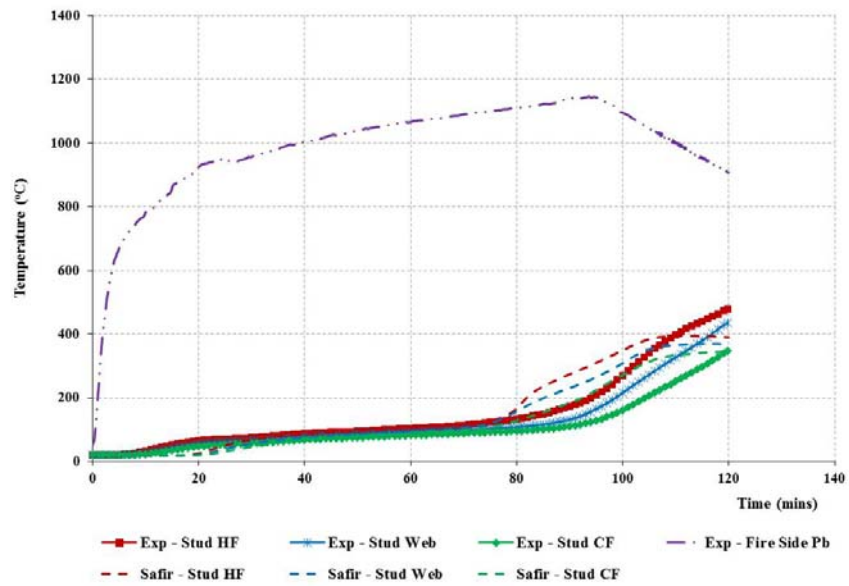
(b) Test LSF4

Note: HF: Hot flange; CF: Cold flange.

Figure 9. Stud Time-Temperature Curves from Fire Tests and Thermal Analyses for LSF Walls Lined with Single Layer of Plasterboard



(a) Test LSF5



(b) Test LSF6

Note: HF- hot flange, CF- cold flange.

Figure 10. Stud Time-Temperature Curves from Fire Tests and Thermal Analyses for LSF Walls with Rock Fibre External Insulation

Thermal analyses conducted by Paulik et al. [23], Hopkin et al. [24], Sergey et al. [25] and Thomas [12] for similar wall panels also found that thermal properties of gypsum plasterboard depend on the heating rate. Numerical analysis conducted by Thomas [12] on light timber framed walls on slow developing and rapid fires also showed similar results, where a good agreement was observed in slow developing fires than rapid fires. Our numerical analysis showed higher temperatures than fire test results, i.e. overestimated the stud temperatures. The likely cause for the difference in results is not including the effects of processes such as moisture flow and ablation of plasterboards that are affected by higher heating rates. The variation in stud temperatures in the early stages of the fire for single plasterboard lined walls could also be due to this higher heating rate as they were exposed to a heating rate well above 50°C/min. This higher heating rate affected the dehydration process of gypsum plasterboard. This process was studied in detail by Paulik et al. [23] and they concluded that the rate of temperature rise influenced the dehydration process, which will thus affect the specific heat values of gypsum plasterboard. In this study, the specific heat values used were measured at a heating rate of 20°C/min under a constant nitrogen gas flow. However, rapid fire curves have a heating rate of 50°C/min. Ang and Wang [26] proposed a correction factor for the specific heat to incorporate the moisture transfer inside the gypsum plasterboard. This is based on numerical analysis of heat and mass transfer in gypsum plasterboard when exposed to fire. However, under fire conditions gypsum plasterboards in LSF walls may also experience ablation, shrinkage and collapse, which were not incorporated in this correction factor. Hence in this study the correction factor for the specific heat of gypsum plasterboard was not considered, and an apparent specific heat value based on the experimental study conducted in [13,15] was used.

In our FEA, elevated temperature thermal properties used with the standard fire tests were used for both rapid and pro-longed fire curves. Hence detailed experimental studies are needed to investigate the effect of rapid fire time-temperature curves on the thermal properties of gypsum plasterboards. However, in most situations the predicted stud temperatures from FEA are higher than those from fire tests, ie. conservative predictions. Considering this outcome, it was decided to use the developed finite element model in this study to obtain the stud hot flange temperatures for a range of realistic design fire time-temperature curves for single and double plasterboard lined walls, and walls with double plasterboard lining and external rock fibre insulation. However, our test and numerical analysis results and past research studies show that specific heat of gypsum plasterboard depends on the heating rate. Detailed experimental studies should be undertaken to investigate the effect of rapid real fires (50°C/min) on the thermal properties of gypsum plasterboards and the thermal performance of LSF wall panels.

4. EFFECT OF REALISTIC DESIGN FIRE TIME-TEMPERATURE CURVES ON THE THERMAL BEHAVIOUR OF LOAD BEARING LSF WALLS

A detailed parametric study was undertaken based on the validated finite element model to investigate the thermal performance of load bearing LSF walls under realistic design fire curves. The parameter considered in this study is the type of fire time-temperature curve, hence as in the fire tests two different types of fire time-temperature curves were selected: Eurocode parametric [3] and Barnett's 'BFD' [5] curves. Eurocode parametric time-temperature curves are influenced by compartment characteristics such as ventilation openings, fuel loads and thermal inertia of the compartment lining material. To simulate both rapid and prolonged fires, two opening factors 0.06 and 0.03 m^{1/2}, were considered with fuel loads of 1268 and 780 MJ/m² of floor area. The compartment thermal lining materials are gypsum plasterboard lined walls and ceilings while concrete floor is assumed in one compartment and timber floor in the other. This will vary the thermal inertia of the compartment from 400 to 715 J/m²S^{1/2}K. Hence the use of two values for each of the three fire parameters; ventilation opening, fuel load and thermal inertia, gave eight

different fire time-temperature curves for Eurocode parametric design fires [3]. Similarly eight Barnett's 'BFD' curves [5] were also developed for the same fire parameters. Thus it resulted in a total of 16 fire time-temperature curves for a wall configuration. Also as in the fire tests, three different wall configurations were considered; single and double plasterboard lined walls and walls with external rock fibre insulation. Hence a total of 48 different fire time-temperature curves were considered in this study.

4.1 LSF Walls Lined with Double Layers of Plasterboards

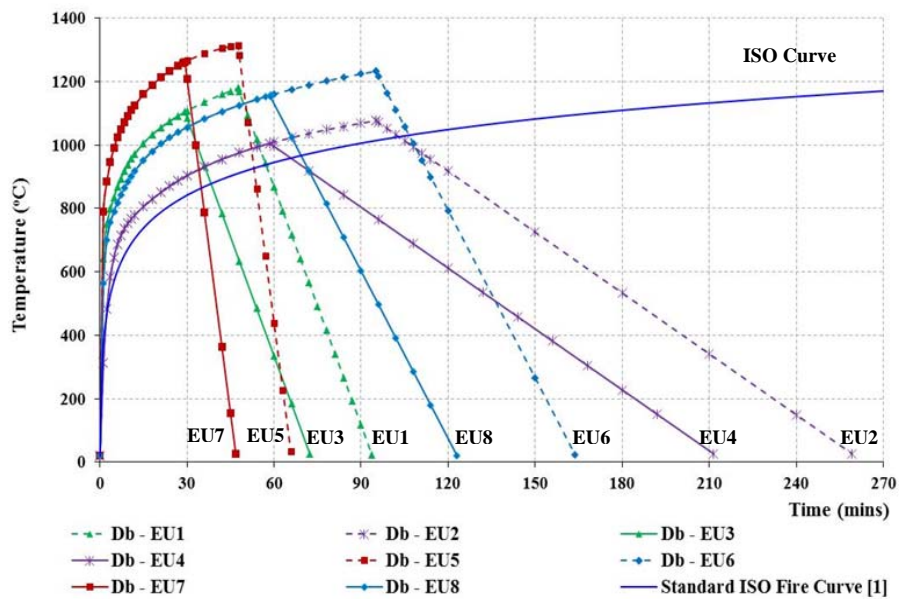
Table 2 presents the design parameters used in developing the Eurocode parametric and 'BFD' design fire time-temperature curves for LSF walls lined with double gypsum plasterboards. The developed fire curves are more severe than the standard fire curve in terms of maximum temperature and time to reach the maximum temperature (Figures 11(a) and 12(a)). Further, all these fire curves have a decay phase. Fire curves Db-EU2 and Db-EU4 are closer to the standard fire curve, but with a decay phase. Fire curves Db-EU1, Db-EU3, Db-EU5 and Db-EU7 represent rapid fires, where a rapid increase in temperature is seen and a maximum temperature higher than 1100°C is reached in less than 45 minutes. Also they have a rapid temperature decrease in the decay phase of the fire. Fire curves Db-EU2, Db-EU4, Db-EU6 and Db-EU8 represent prolonged fires for which the maximum temperature is reached after 90 minutes of fire duration and the total fire duration is more than 2 hours including a linear decay phase. The maximum temperature of the fire curves Db-BFD1, Db-BFD3, Db-BFD5 and Db-BFD7 is nearly 1200°C and it is 1057°C for other fire curves. The rate of temperature rise is gradual compared to Eurocode parametric and standard fire curves, and the decay phase is also very slow.

The stud hot and cold flange time-temperature curves for the Eurocode parametric and 'BFD' design fire curves were obtained using the finite element thermal analyses and are shown in Figures 11(b) and 12(b). The stud hot and cold flange time-temperatures for the standard fire curve are also shown in these figures for comparison purposes. For nearly 30 minutes the stud temperatures agreed well with each other despite the differences in the rate of temperature rise in the fire curve and the temperatures are also less than 100°C. This is due to the dehydration process of gypsum plasterboard. Beyond this, the stud temperatures increased and followed the fire time-temperature curve. The rapid increase in temperatures in Fire curves Db-EU1, Db-EU3, Db-EU5 and Db-EU7 in the early stage of the fire caused the stud temperatures to increase more quickly. However, the stud temperatures started to decrease after reaching the maximum when the fire time-temperature curves were in the decay phase. In the LSF walls exposed to Eurocode parametric design fire curves, the stud temperatures decrease rapidly as soon as the fire time-temperature curves are in the decay phase. This is due to the rapid decay rate in the parametric fires. But for the studs exposed to 'BFD' curves, the stud temperatures are maintained at the maximum for considerable time or are seen to increase with time.

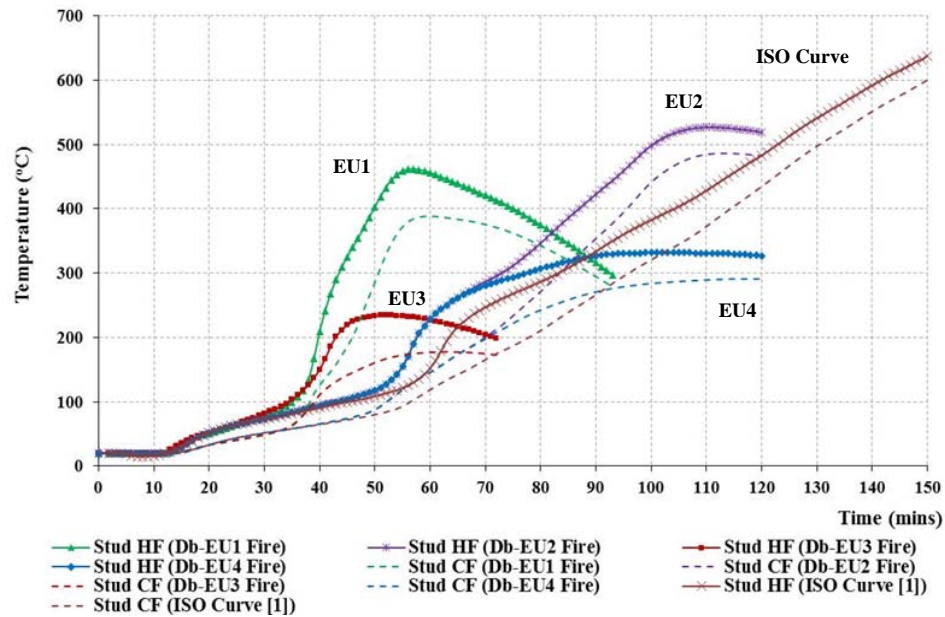
Table 2. Fire Compartment Characteristics Used in the Development of Design Fire Curves for LSF Walls Lined with Double Layers of Plasterboards

(a) Eurocode parametric fire curves					
Eurocode Parametric Fire Curves [3]	Opening Factor ($\text{m}^{1/2}$)	Compartment Thermal Inertia ($\text{J/m}^2\text{S}^{1/2}\text{K}$)	Fuel Load (MJ/m^2)		
Db - EU1	0.06	710.3	1268		
Db - EU2	0.03	702.1	1268		
Db - EU3	0.06	710.3	780		
Db - EU4	0.03	702.1	780		
Db - EU5	0.06	423.4	1268		
Db - EU6	0.03	423.2	1268		
Db - EU7	0.06	423.4	780		
Db - EU8	0.03	423.2	780		

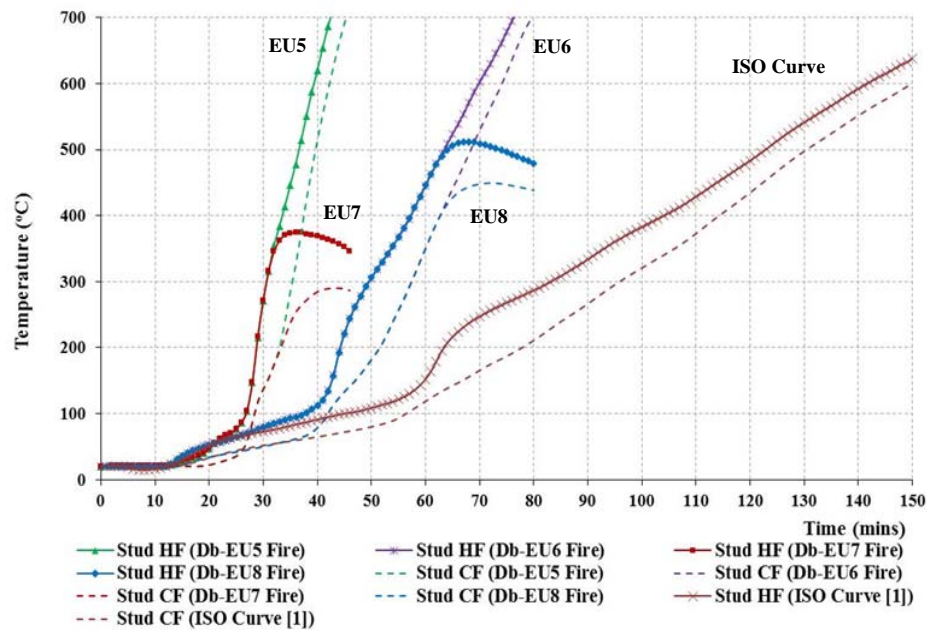
(b) 'BFD' fire curves					
'BFD' Fire Curves [5]	Opening Factor ($\text{m}^{1/2}$)	Fuel Load (MJ/m^2)	Fire Maximum Temperature - T_m ($^{\circ}\text{C}$)	Time to reach Maximum Temperature - t_m (mins)	Shape Constant - c
Db - BFD1	0.06	1268	1193	48	38
Db - BFD2	0.03	1268	1057	95	38
Db - BFD3	0.06	780	1193	29	38
Db - BFD4	0.03	780	1057	59	38
Db - BFD5	0.06	1268	1193	48	16
Db - BFD6	0.03	1268	1057	95	16
Db - BFD7	0.06	780	1193	29	16
Db - BFD8	0.03	780	1057	59	16



(a) Eurocode parametric design fire curves

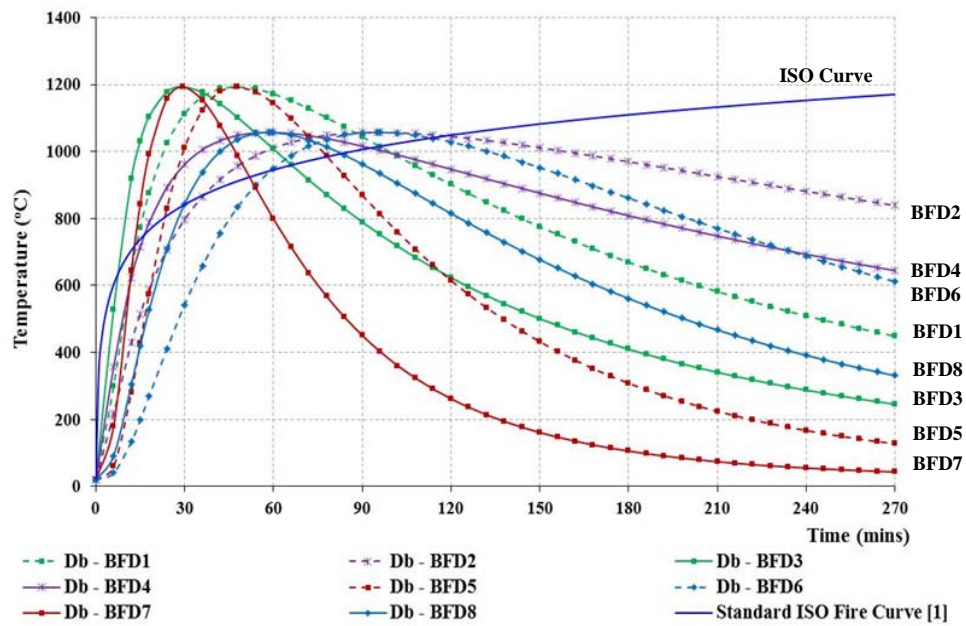


(b) Stud hot and cold flange temperatures for Fire Curves Db-EU1 to Db-EU4

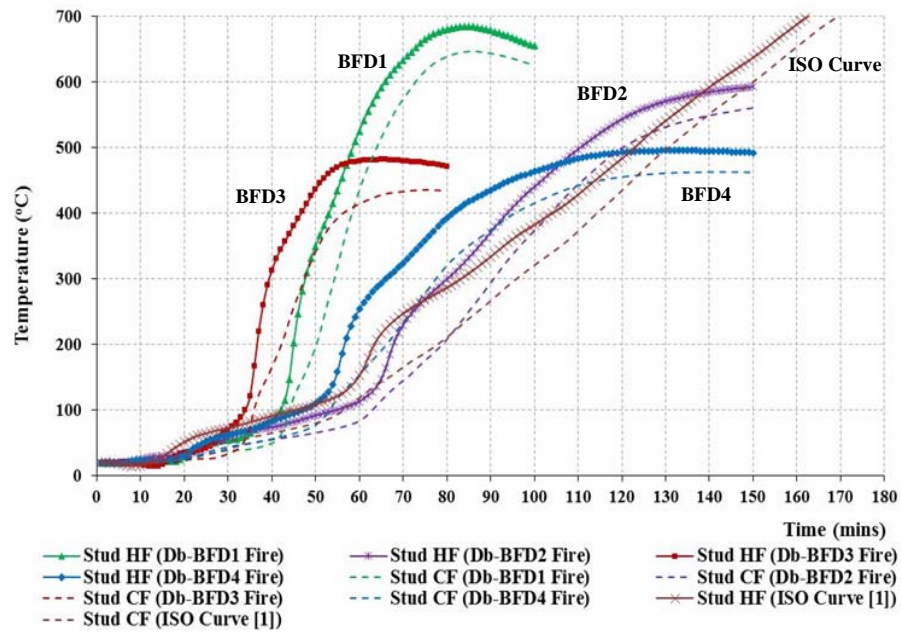


(c) Stud hot and cold flange temperatures for Fire Curves Db-EU5 to Db-EU8

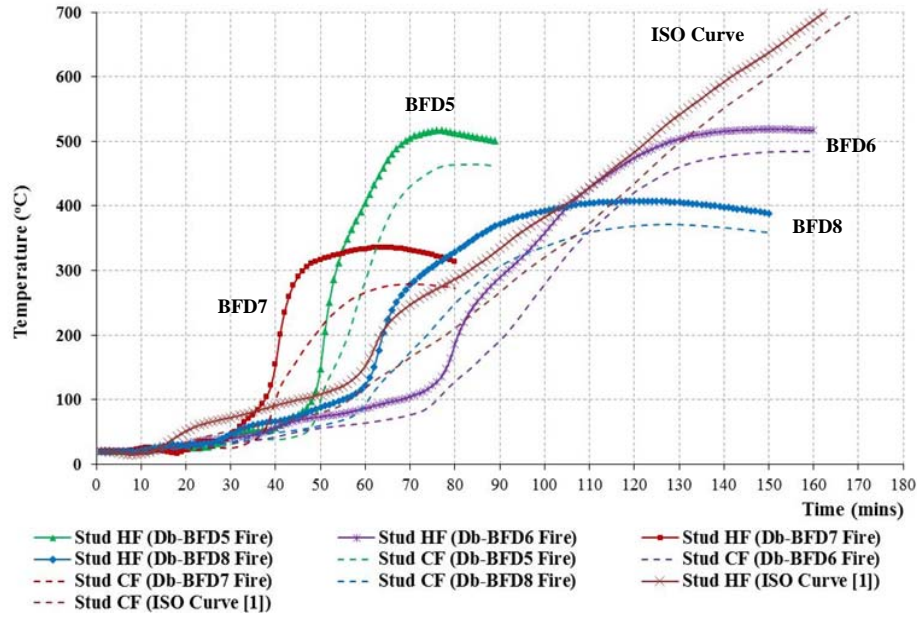
Figure 11. Stud Time-Temperature Curves Obtained from FEA for Double Layers of Plasterboard Lined LSF Walls Exposed to Eurocode Parametric Fire Curves



(a) 'BFD' design fire curves



(b) Stud hot and cold flange temperatures for Fire Curves Db-BFD1 to Db-BFD4



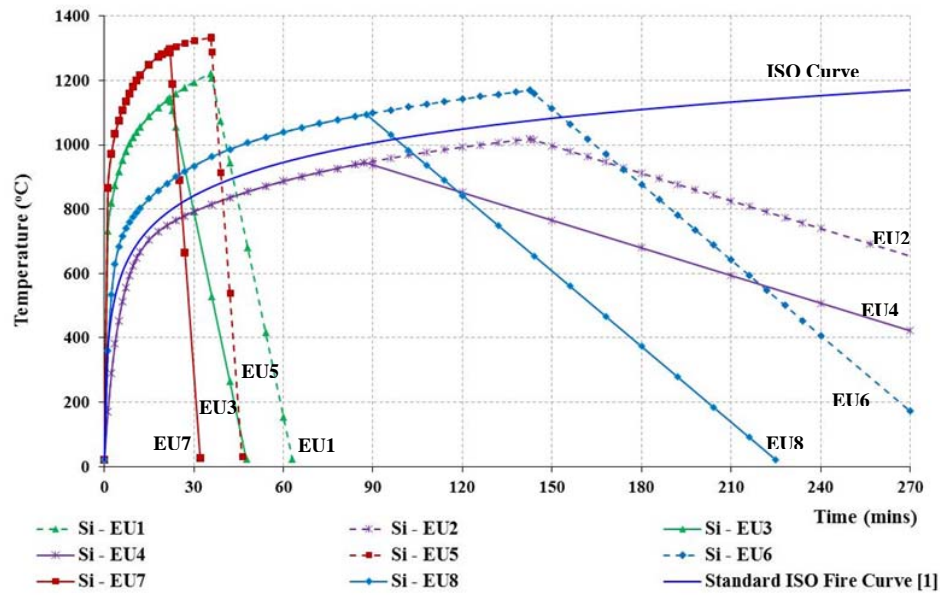
(c) Stud hot and cold flange temperatures for Fire Curves Db-BFD5 to Db-BFD8

Figure 12. Stud Time–Temperature Curves Obtained from FEA for Double Layers of Plasterboard Lined LSF Walls Exposed to ‘BFD’ Fire Curves

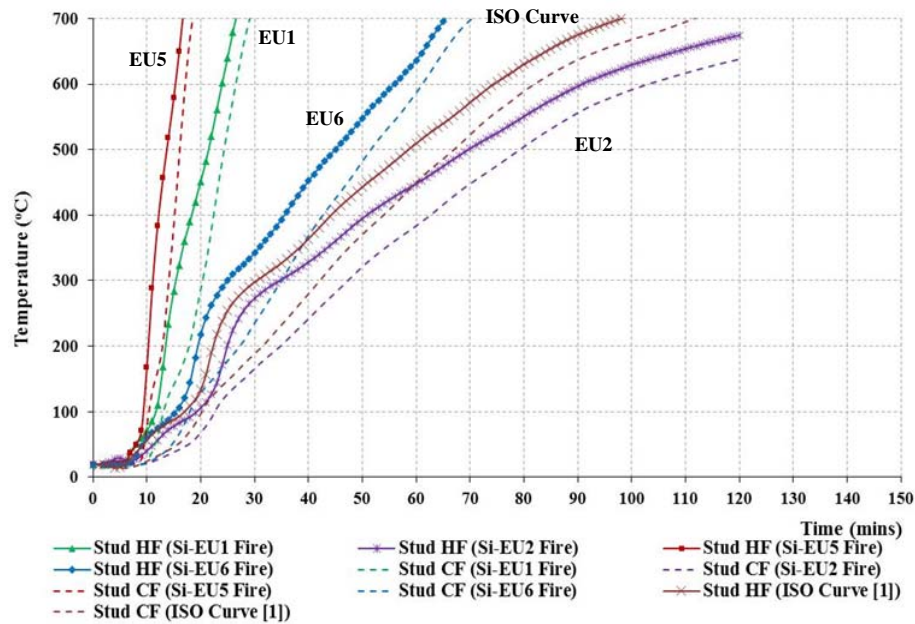
4.2

LSF Walls Lined with Single Layer of Gypsum Plasterboard

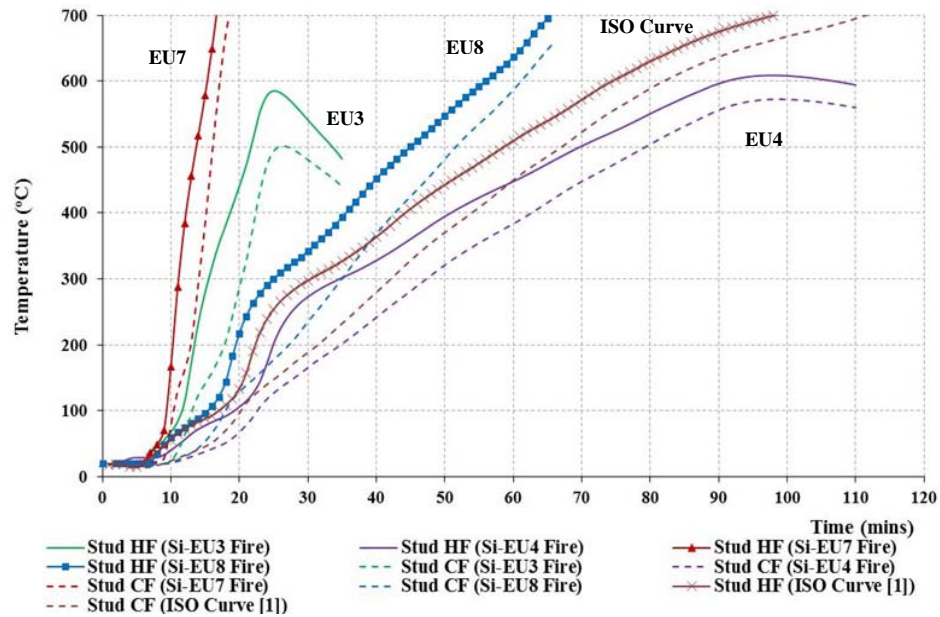
Table 3 presents the fire parameters used in developing the Eurocode parametric and ‘BFD’ fire curves, and the developed fire curves are shown in Figures 13(a) and 14(a). Fire curves Si-EU1, Si-EU3, Si-EU5 and Si-EU7 are considered rapid fires as their rates of temperature rise are higher than the standard fire [1] and reach a maximum temperature of nearly 1200°C in less than 40 minutes. Fire curves Si-EU2, Si-EU4, Si-EU6 and Si-EU8 are prolonged fires with fire durations of more than three hours. Fire curves Si-BFD1, Si-BFD3, Si-BFD5 and Si-BFD7 are considered severe fires and are rapid in temperature rise, where a maximum temperature of nearly 1200°C is reached in less than 40 minutes. Fire curves Si-BFD2, Si-BFD4, Si-BFD6 and Si-BFD8 are considered less severe fires compared to the standard fire curve [1], and are also prolonged fires. They only reach a maximum temperature of 850°C in 90 minutes or more.



(a) Eurocode parametric design fire curves

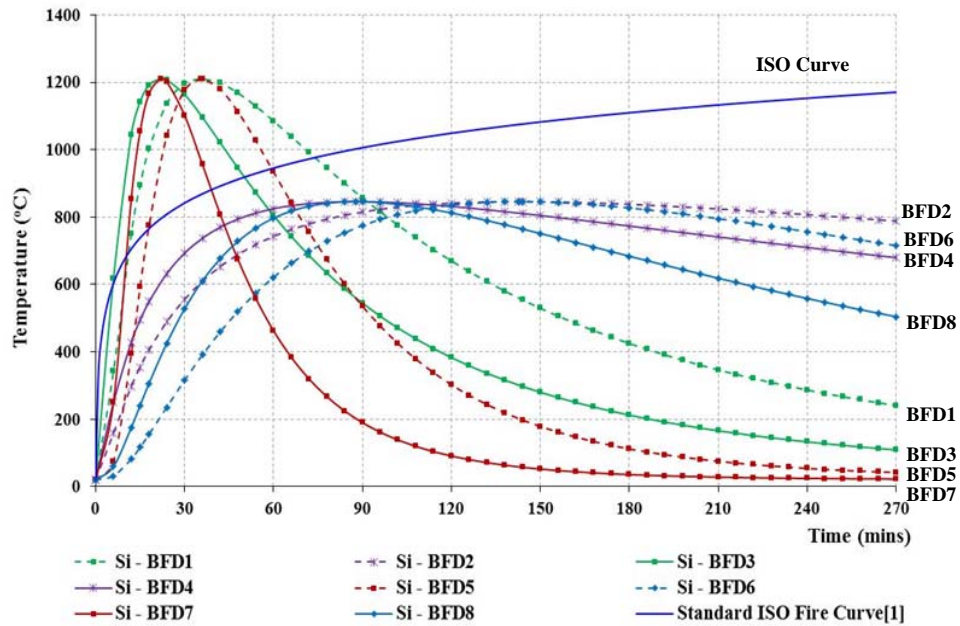


(b) Stud hot and cold flange temperatures for Fire Curves Si-EU1, Si-EU2, Si-EU5 and Si-EU6

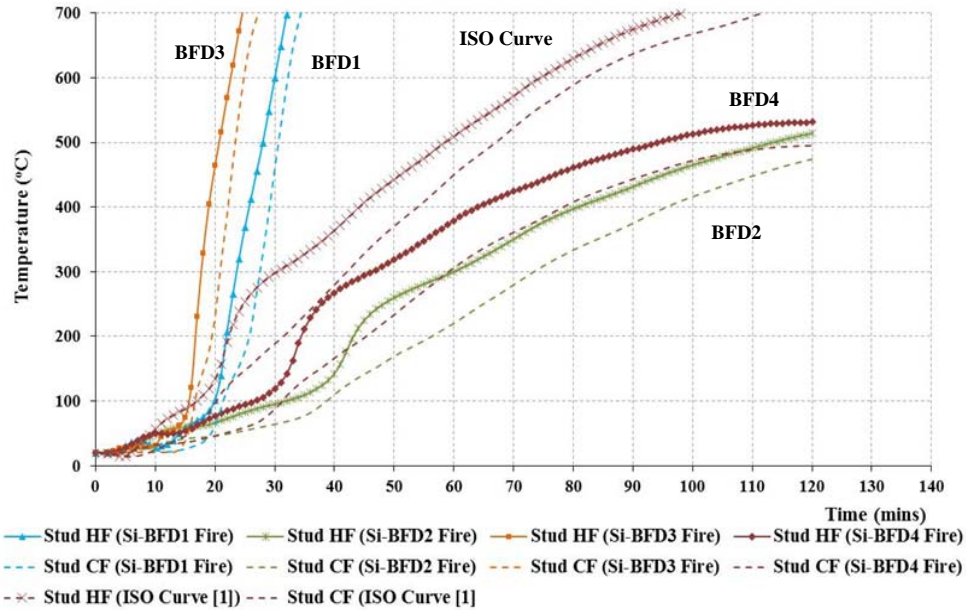


(c) Stud hot and cold flange temperatures for Fire Curves
Si-EU3, Si-EU4, Si-EU7 and Si-EU7

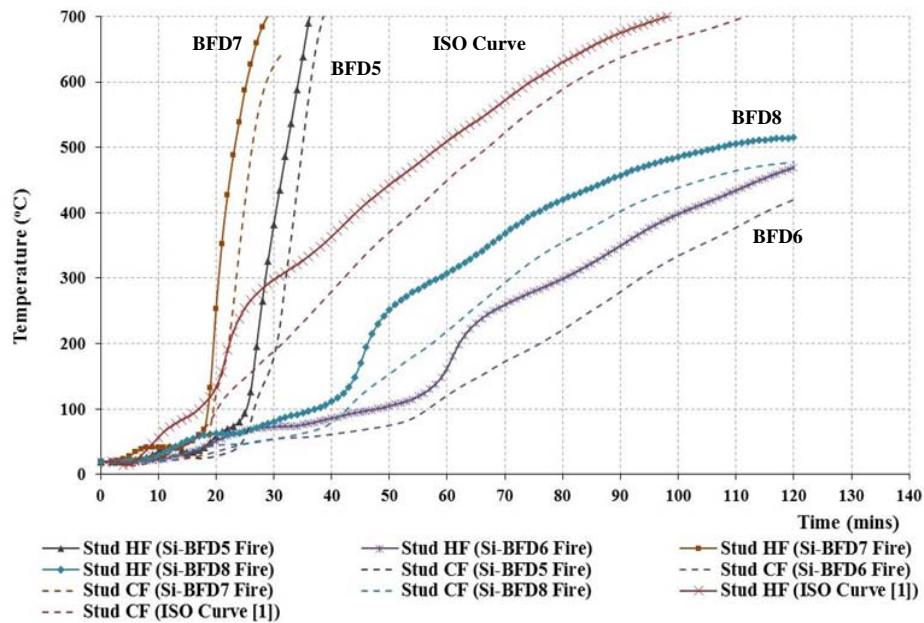
Figure 13. Stud Time-Temperature Curves Obtained from FEA for Single Layer of
Plasterboard Lined LSF Wall Exposed to Eurocode Parametric Fire Curves



(a) 'BFD' fire curves



(b) Stud hot and cold flange temperatures for Fire Curves Si-BFD1 to Si-BFD4



(c) Stud hot and cold flange temperatures for Fire Curves Si-BFD5 to Si-BFD8

Figure 14. Stud Time-Temperature Curves Obtained from FEA for Single Layer of Plasterboard Lined LSF Walls Exposed to 'BFD' Fire Curves

Figures 13(b) and 14(b) show the stud hot and cold flange time-temperature curves obtained from finite element thermal analyses. As seen in Figure 13(a) the rates of fire temperature rise are similar in the cases of Si-EU1 and Si-EU3, Si-EU2 and Si-EU4, Si-EU5 and Si-EU7, and Si-EU6 and Si-EU8, and thus stud temperatures are also the same as seen in Figures 13 (b) and (c). Eurocode parametric design Fire curves Si-EU1 and Si-EU2 were developed for the fuel load of 1268 MJ/m², compartment thermal inertia of 715.4 and 700.1 J/m²S^{1/2}K and for opening factors 0.08 and 0.02 m^{1/2}, respectively. Opening factors 0.08 and 0.02 m^{1/2} represent rapid and prolonged fires, respectively and the fire curves reached a maximum temperature of 1222°C in 36 minutes and 1018°C in 142 minutes. Also in another instance stud hot flange temperature is 602°C at 24 minutes for Fire curve Si-EU1 and it is only 171°C for Fire curve Si-EU2. Similar behaviour is also observed for Fire curves Si-EU3, Si-EU5 and Si-EU7 when compared with Fire curves Si-EU4, Si-EU6 and Si-EU8. Hence it can be concluded that stud temperature rise is influenced by the rate of temperature rise in the fire curve, and that the rapid fires will significantly reduce the fire resistance of single plasterboard lined LSF walls. The stud hot flange temperatures for the rapid fire curves (Si-BFD1, Si-BFD3, Si-BFD5 and Si-BFD7) are greater than 700°C in less than 40 minutes of fire exposure. The corresponding stud cold flange temperatures are also very high. The stud hot flange temperatures for prolonged fires are very much less than those of rapid fire curves and are about 500°C after 90 minutes of fire exposure.

Table 3. Fire Compartment Characteristics Used in the Development of Design Fire Curves for LSF Walls Lined with Single Layer of Plasterboard

(a) Eurocode parametric fire curves					
Eurocode Parametric Fire Curves [3]	Opening Factor (m ^{1/2})	Compartment Thermal Inertia (J/m ² S ^{1/2} K)	Fuel Load (MJ/m ²)		
Si - EU1	0.08	715.4	1268		
Si - EU2	0.02	700.1	1268		
Si - EU3	0.08	715.4	780		
Si - EU4	0.02	700.1	780		
Si - EU5	0.08	423.5	1268		
Si - EU6	0.02	423.2	1268		
Si - EU7	0.08	423.5	780		
Si - EU8	0.02	423.2	780		

(b) 'BFD' fire curves					
'BFD' Fire Curves [5]	Opening Factor (m ^{1/2})	Fuel Load (MJ/m ²)	Fire Maximum Temperature -T _m (°C)	Time to reach Maximum Temperature - t _m (mins)	Shape Constant-c
Si - BFD1	0.08	1268	1211	36	38
Si - BFD2	0.02	1268	845	143	38
Si - BFD3	0.08	780	1211	22	38
Si - BFD4	0.02	780	846	88	38
Si - BFD5	0.08	1268	1211	36	16
Si - BFD6	0.02	1268	845	143	16
Si - BFD7	0.08	780	1211	22	16
Si - BFD8	0.02	780	846	88	16

4.3 LSF Walls Externally Insulated with Rock Fibre Insulation

As for single and double plasterboard lined LSF walls, LSF walls externally insulated with rock fibre insulation were also analysed for both Eurocode parametric and 'BFD' fire curves. The fire parameters are given in Table 4 while Figures 15 and 16 show the corresponding fire curves and stud hot and cold flange temperatures obtained from thermal analyses. The rate of temperature rise in these eight fire curves (Fire curves Cp-EU1 to Cp-EU8) is much higher than the standard fire curve, and the maximum temperatures are also well above that of standard fire curve. The maximum fire temperatures of Fire curves Cp-EU5 and Cp-EU7 are well above 1300°C achieved in less than 50 and 30 minutes, respectively, whereas in Fire curves Cp-EU2 and Cp-EU4 they are about 1100°C in 60 and 90 minutes, respectively (Figure 15).

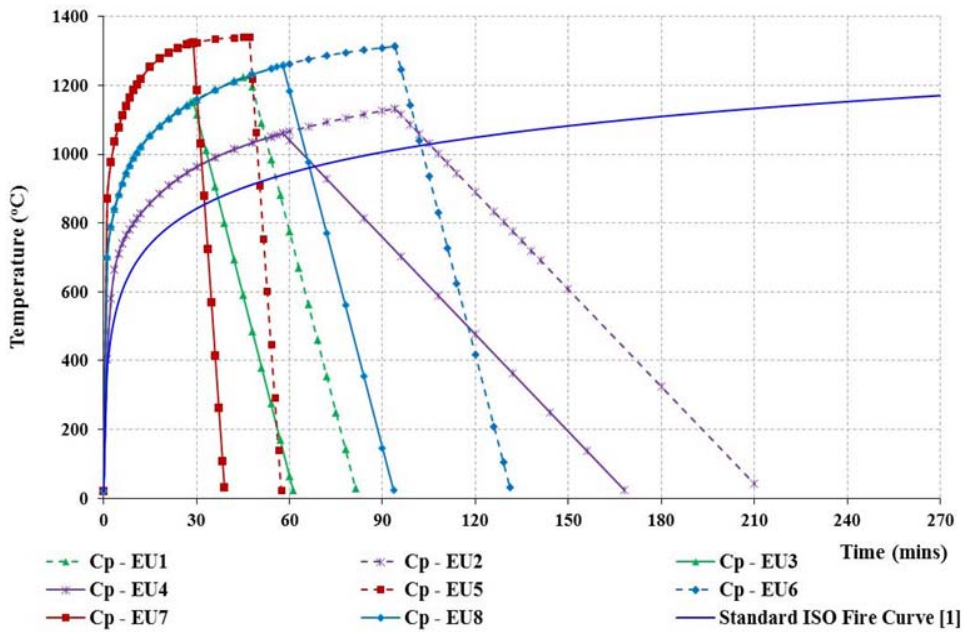
The stud hot flange temperatures for the Fire curves Cp-EU1, Cp-EU3, Cp-EU5 and Cp-EU7 started to decrease in less than 60 minutes of fire exposure. This is due to the decay phase in the fire time-temperature curve where fire temperatures started to decrease with time rapidly. Hence the stud temperatures also decreased with time. The highest stud hot flange temperature was obtained for Fire Curve Cp-EU6 and it was 740°C after 90 minutes of fire exposure. For rapid fires, stud temperatures increased much earlier than for prolonged fires. Also unlike in the Eurocode parametric fire curves, the stud hot flange temperatures are seen to increase for considerable time for 'BFD' fire curves even in the decay phase due to the slow rate of fire temperature decrease. For instance, Fire curve Cp-BFD1 reached the maximum temperature at 48 minutes, and the stud hot flange reached its maximum temperature at 132 minutes, which indicates that stud temperatures increased for nearly 80 minutes in the decay phase of the fire. At 48 minutes the stud hot flange temperature was 100°C while it was 534°C at 132 minutes. This was due to high fire temperatures and slow rate of fire temperature decrease. As for the previous LSF wall configurations, the stud time-temperature curves in this case also followed the fire time-temperature profiles. But the rate of temperature rise in studs is much slower than it is for single and double plasterboard lined LSF walls due to the use of rock fibre external insulation.

Table 4. Fire Compartment Characteristics Used in the Development of Design Fire Curves for LSF Walls Externally Insulated with Rock Fibre Insulation

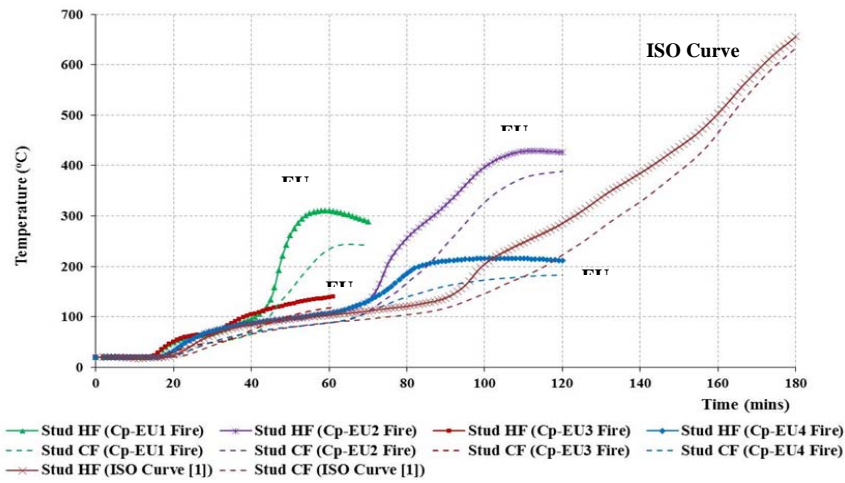
(a) Eurocode parametric fire curves			
Eurocode Parametric Fire Curves [3]	Opening Factor (m ^{1/2})	Compartment Thermal Inertia (J/m ² S ^{1/2} K)	Fuel Load (MJ/m ²)
Cp - EU1	0.06	606.3	1268
Cp - EU2	0.03	585.3	1268
Cp - EU3	0.06	606.3	780
Cp - EU4	0.03	585.3	780
Cp - EU5	0.06	316.9	1268
Cp - EU6	0.03	305.2	1268
Cp - EU7	0.06	316.9	780
Cp - EU8	0.03	305.2	780

(b) BFD' fire curves

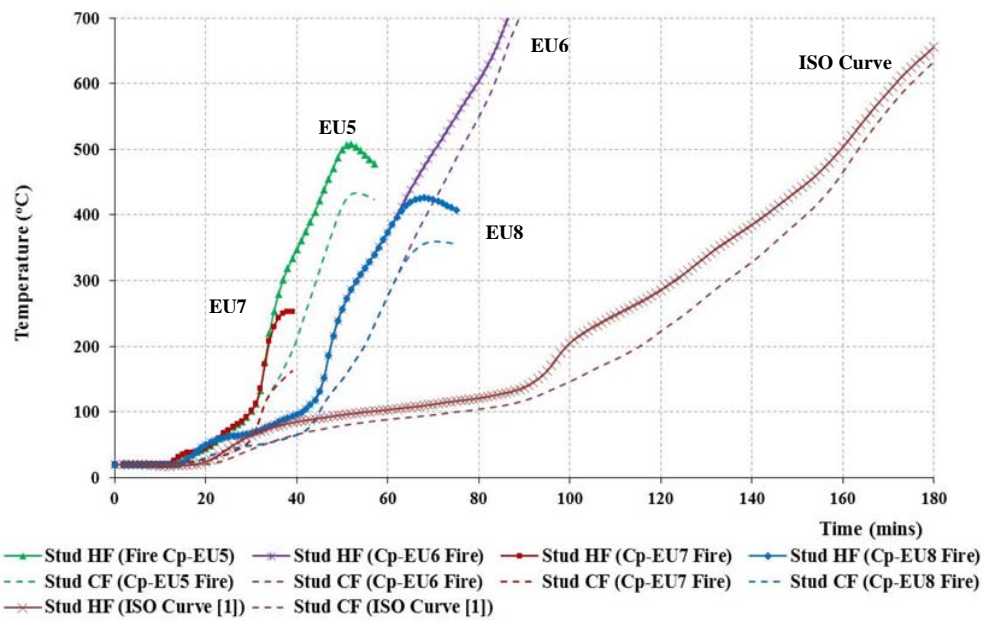
'BFD' Fire Curves [5]	Opening Factor (m ^{1/2})	Fuel Load (MJ/m ²)	Fire Maximum Temperature - T _m (°C)	Time to reach Maximum Temperature - t _m (mins)	Shape Constant- c
Cp - BFD1	0.06	1268	1193	48	38
Cp - BFD2	0.03	1268	1057	95	38
Cp - BFD3	0.06	780	1193	29	38
Cp - BFD4	0.03	780	1057	59	38
Cp - BFD5	0.06	1268	1193	48	16
Cp - BFD6	0.03	1268	1057	95	16
Cp - BFD7	0.06	780	1193	29	16
Cp - BFD8	0.03	780	1057	59	16



(a) Eurocode parametric design fire curves

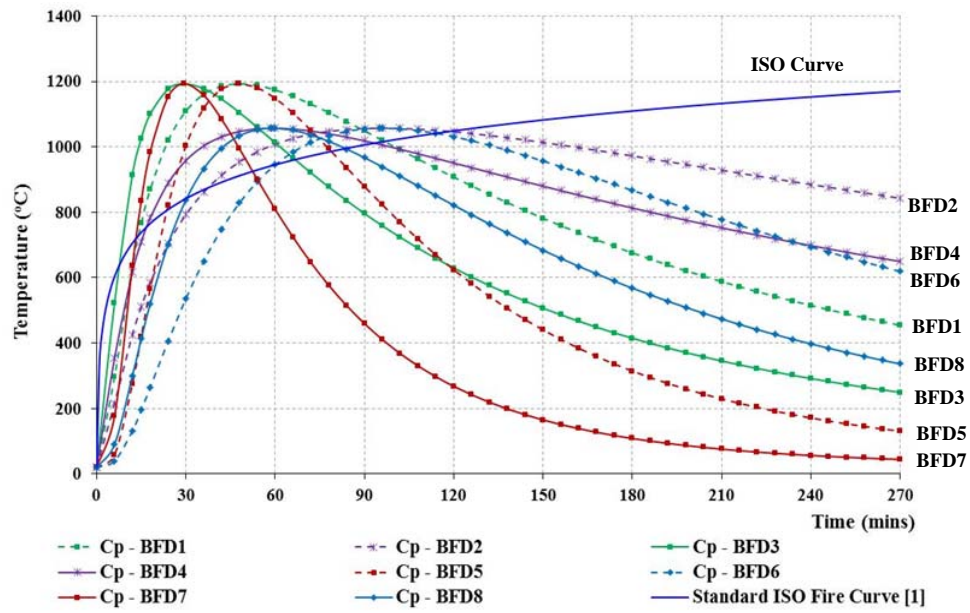


(b) Stud hot and cold flange temperatures for Fire Curves Cp-EU1 to Cp-EU4

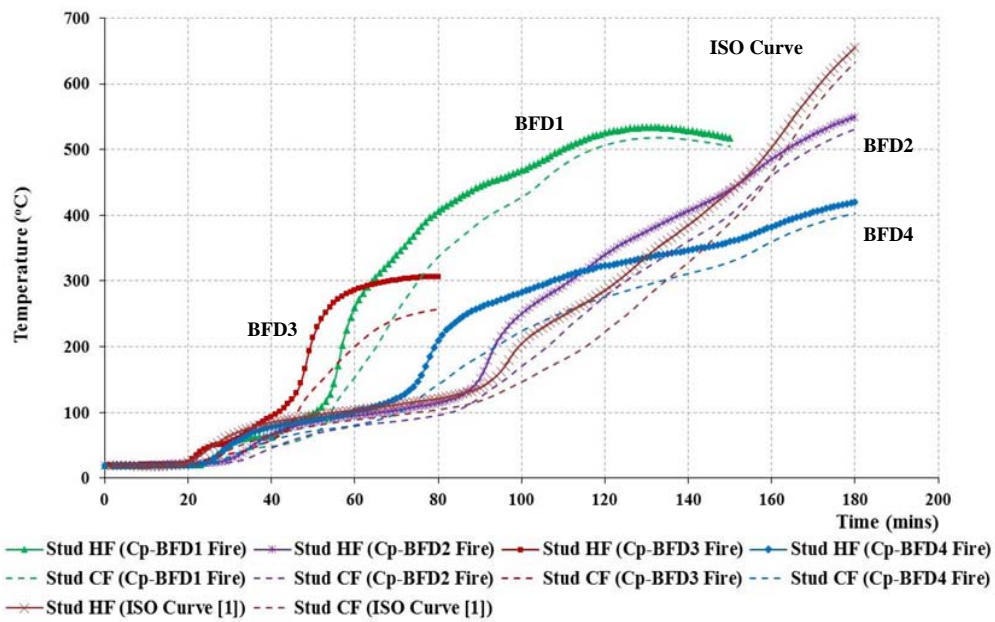


(c) Stud hot and cold flange temperatures for Fire Curves Cp-EU5 to Cp-EU8

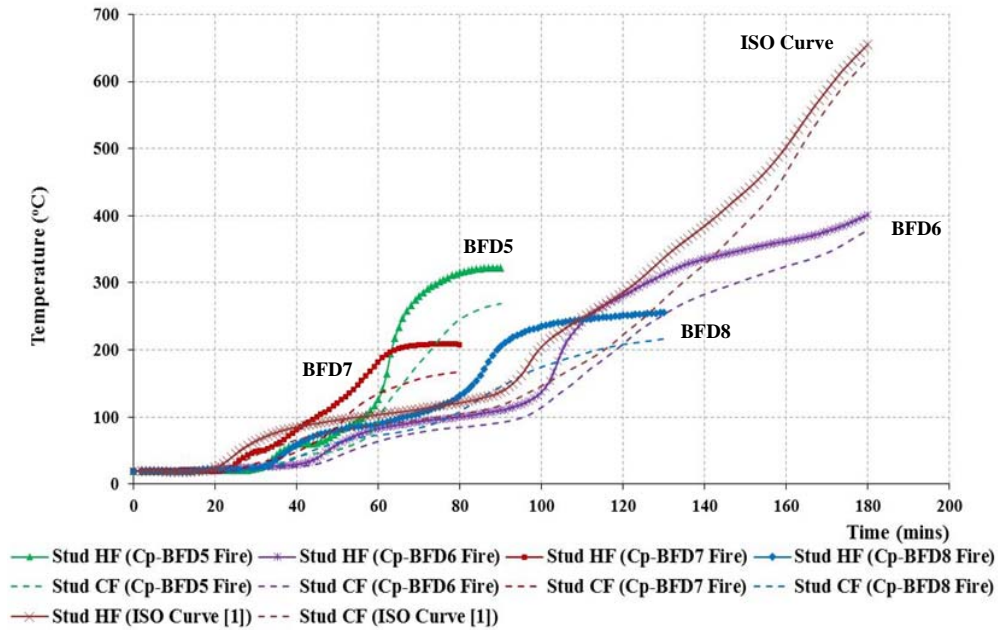
Figure 15. Stud Time–Temperature Curves Obtained from FEA for LSF Walls Externally Insulated with Rock Fibre Insulation Exposed to Eurocode Parametric Fire Curves



(a) 'BFD' fire curves



(b) Stud hot and cold flange temperatures for Fire Curves Cp-BFD1 to Cp-BFD4



(c) Stud hot and cold flange temperatures for Fire Curves Cp-BFD1 to Cp-BFD4

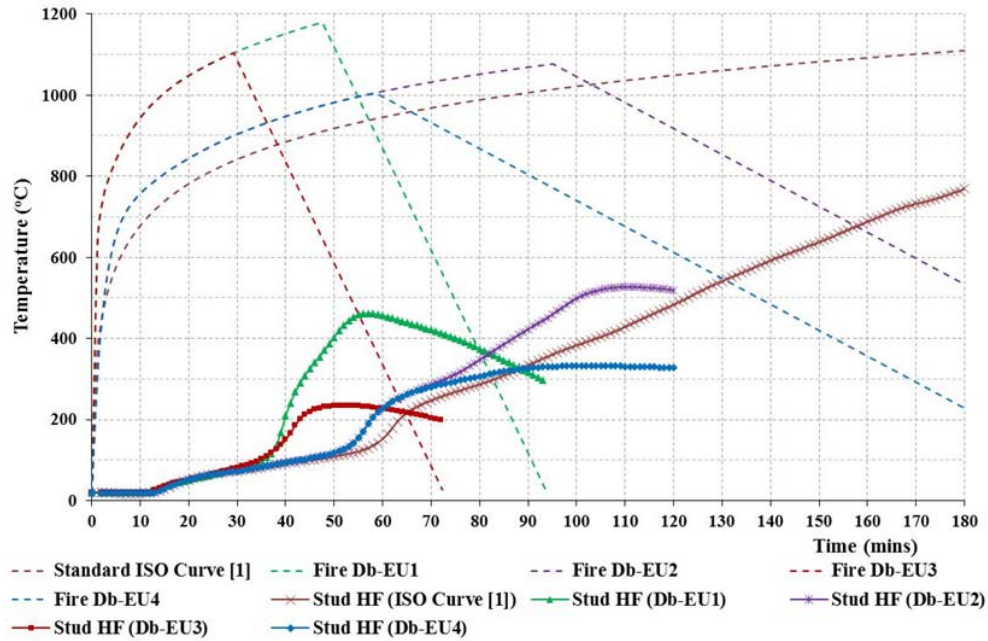
Figure 16. Stud Time-Temperature Curves Obtained from FEA for LSF Walls Externally Insulated with Rock Fibre Insulation and Exposed to 'BFD' Fire Curves

4.4 Final Comments and Development of a Simple Method to Estimate Fire Rating

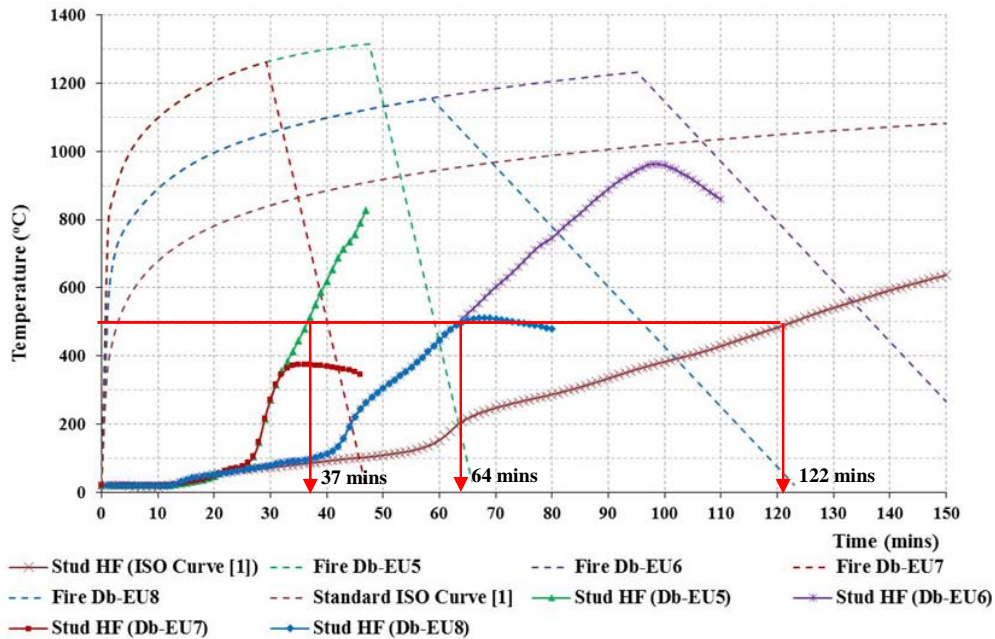
Based on the finite element analysis based parametric studies of LSF walls lined with single and double plasterboards and walls externally insulated with rock fibre insulation, the following observations can be made.

- The stud temperature rise is significantly influenced by the type of fire time-temperature curve. The maximum fire temperature and the time it occurs in the fire curve significantly influence the stud temperatures. This implies that fire resistance rating (FRR) of LSF wall will also be influenced by the type of fire time-temperature curve.
- Rapid fires cause the stud temperatures to increase rapidly than prolonged fires. Hence significant reductions of the stud capacity could be observed in the early stage of the fire.
- Temperature in the prolonged fire curves increases with time for a much longer duration than rapid fire curves. Hence stud temperatures also continue to increase with time.
- The decay rate of fire time-temperature curve has an effect on the stud time-temperature curve. A slow decay rate increases the stud temperatures for considerable time even in the decay phase of the fire whereas a rapid decay rate reduces the stud temperatures quickly.
- Stud temperatures increase even in the decay phase of the fire, and hence LSF wall studs can fail in the decay phase of the fire if the studs reach their critical failure temperature.
- Single plasterboard lined LSF walls are highly responsive to fires as the stud temperatures increase rapidly compared to other LSF wall configurations.

- LSF walls externally insulated with rock fibre insulation are able to protect the steel studs from temperature rise. The stud hot and cold flange temperatures are less than those of single and double plasterboard lined LSF wall studs.



(a) Stud hot flange temperatures for Fire Curves Db-EU1 to Db-EU4



(b) Stud hot flange temperatures for Fire Curves Db-EU5 to Db-EU8

Figure 17. Stud Time–Temperature Curves of Double Plasterboard Layers Lined LSF Walls Exposed to Realistic Design Fires

Fire tests of LSF walls under realistic fire conditions [4] have shown that LSF wall stud failure is mostly governed by its hot flange temperature for similar conditions. Hence using a limiting hot flange temperature method, LSF wall stud failure times can be computed for any realistic design fire curves provided the stud hot flange time-temperature curves are known. For instance, Figures 17 (a) and (b) show the FEA results of double plasterboard lined LSF walls exposed to different realistic design fire curves, and compare them with those under standard fire curve. If the critical limiting temperature of LSF wall studs is 500°C for a particular load ratio, then the stud failure times, ie. fire resistance ratings of LSF walls, can be calculated from Figure 17. For the following fire Curves: Standard ISO curve, Db-EU1 to Db-EU8 the stud hot flange failure times or FRR are 122 mins, NF, 100 mins, NF, NF, 37 mins, 64 mins, NF and 64 mins, respectively, where NF – No Failure. These results show that if the critical stud hot flange temperature is 500°C, the realistic design fires such as Db-EU2, Db-EU5, Db-EU6 and Db-EU8 can cause more severe damage to LSF walls than the standard ISO fire curve [1]. On the other hand LSF wall panels will not fail under realistic design fires such as Db-EU1, Db-EU3, Db-EU4 and Db-EU7. The limiting stud hot flange temperature varies as a function of load ratio for load bearing LSF wall panels [4]. Using the same method, FRR of LSF walls under realistic design fire curves can be determined for load bearing walls with varying load ratios by using the corresponding limiting stud hot flange temperatures. The same can be achieved for Barnett's BFD fire curves or any other type of fire curve provided the stud time-temperature curves and limiting (critical) stud hot flange temperatures are available. Finite element thermal models such as those developed in this research can be used to determine the stud time-temperature curves.

5. CONCLUSIONS

This paper has presented the details of a numerical study on the thermal performance of load bearing LSF wall panels under realistic design fire time-temperature curves. It includes the details of the developed finite element models of load bearing LSF wall panels, the thermal analysis results from SAFIR under realistic design fire curves and their comparisons with fire test results obtained by Ariyanayagam and Mahendran [4]. A reasonable agreement with fire test results showed that accurate finite element models can be developed and used to simulate the thermal behaviour of full scale load bearing LSF wall panels under realistic fire conditions. Finite element models were then used in detailed parametric studies to investigate the effects of different LSF wall configurations such as single and double layers of plasterboard lining and external rock fibre insulation and realistic design fire scenarios. The study shows that the type of fire time-temperature curve significantly influenced the stud time-temperature curves. The characteristics of real fire curves such as the maximum fire temperature, the time this occurs and the rate of decay significantly influenced the stud temperatures. The analysis results also show that finite element thermal models of LSF walls can be used to predict the fire performance including their fire resistance rating with reasonable accuracy for varying configurations of plasterboard lined LSF walls exposed to realistic design fire curves. Further, a simple method is also proposed in this paper to estimate the fire resistance rating of LSF walls under varying fire scenarios based on finite element thermal analysis predicted stud time-temperature curves and appropriate critical stud hot flange temperatures.

ACKNOWLEDGEMENTS

The authors would like to thank Australian Research Council for their financial support and Queensland University of Technology for providing the necessary facilities and support to conduct this research project.

REFERENCES

- [1] ISO 834-1, Fire Resistance Tests – Elements of Buildings Construction – Part-1 General Requirement, International Organization for Standardization, Switzerland, 1999.
- [2] Ariyanayagam, A.D. and Mahendran, M., “Development of Realistic Design Fire Time-Temperature Curves for the Testing of Cold-formed Steel Wall Systems”, *Journal of Frontiers of Structural and Civil Engineering*, 2014, Vol. 8, No. 4, pp. 427-447.
- [3] ENV 1991-1-2, Eurocode 1: Actions on Structures, Part 1.2: Actions on Structures Exposed to Fire, European Committee for Standardization, Brussels, Belgium, 2002.
- [4] Ariyanayagam, A.D. and Mahendran, M., “Experimental Study of Load Bearing Cold-formed Steel Walls Exposed to Realistic Design Fires”, *Journal of Structural Fire Engineering*, 2014, Vol. 5, No. 4, pp. 291-329.
- [5] Barnett, C.R., “BFD curve: A New Empirical Model for Fire Compartment Temperatures”, *Fire Safety Journal* 2002, Vol. 37, pp. 437-463.
- [6] Mehaffy, J.R., Cuerrier, P., and Carisse, G., “A Model for Predicting Heat Transfer through Gypsum-Board/ Wood-Stud Walls Exposed to Fire”, *Fire and Materials*, 1994, Vol. 18, No. 5, pp. 297-305.
- [7] Sultan, A.M., “A Model for Predicting Heat Transfer Through Non-insulated Unloaded Steel-Stud Gypsum Board Wall Assemblies Exposed to Fire”, *Fire Technology*, 1996, Vol. 32, No. 3, pp. 239-259.
- [8] Collier, P., “A Model for Predicting the Fire-Resisting Performance of Small-Scale Cavity Walls in Realistic Fires”, *Fire Technology*, 1996, Vol. 32, No. 2, pp. 120-136.
- [9] Takeda, H. and Mehaffy, J.R., “WALL2D: A Model for Predicting Heat Transfer through Wood-Stud Walls Exposed to Fire”, *Fire and Materials*, 1998, Vol. 22, No. 4, pp. 133-140.
- [10] Wakili, K.G., Hugi, E., Wullschlegel, L. and Frank, T.H., “Gypsum Board in Fire - Modelling and Experimental Validation”, *Journal of Fire Sciences*, 2007, Vol. 25, No. 3, pp. 267-282.
- [11] Franssen, J.M., “SAFIR. A Thermal/Structural Program for Modelling Structures under Fire”, *Engineering Journal AISC*, 2005, Vol. 42, No. 3, pp. 143-158.
- [12] Thomas, G., “Modelling Thermal Performance of Gypsum Plasterboards under Fire Conditions”, *Fire Safety Journal*, 2010, Vol. 53, pp. 105-119.
- [13] Keerthan, P. and Mahendran, M., “Numerical Modelling of Non-load Bearing Light Gauge Cold-formed Steel Frame Walls under Fire Conditions”, *Journal of Fire Sciences*, 2012, Vol. 30, pp. 375-403.
- [14] Feng, M., Wang, Y.C. and Davies, J.M., “Thermal Performance of Cold-formed Thin-walled Steel Panel Systems in Fire”, *Fire Safety Journal*, 2003, Vol. 38, No. 4, pp. 365-394.
- [15] Keerthan, P. and Mahendran, M., “Thermal Performance of Composite Panels Under Fire Conditions Using Numerical Studies: Plasterboards, Rockwool, Glass Fibre and Cellulose Insulations”, *Fire Technology*, 2012, Vol. 49, pp. 329-356.
- [16] Keerthan, P. and Mahendran, M., “Numerical Studies of Gypsum Plasterboard Panels Under Standard Fire Conditions”, *Fire Safety Journal*, 2012, Vol. 53, pp. 105-119.
- [17] Kolarkar, P. and Mahendran, M., “Experimental Studies of Gypsum Plasterboards and Composite Panels under Fire Conditions”, *Fire and Materials*, 2012, Vol. 38, No. 1, pp. 13-35.
- [18] EN 1993-1-2:2005, Eurocode 3: Design of Steel Structures – Part 1.2: General Rules – Structural Fire Design. European Committee for Standardization, Brussels, Belgium.
- [19] Keerthan, P. and Mahendran, M., “Thermal Performance of Load Bearing Cold-formed Steel Walls under Fire Conditions using Numerical Studies”, *Journal of Structural Fire Engineering*, 2014, Vol. 5, No. 3, pp. 261-289.
- [20] Buchanan, A.H., “Structural Design for Fire Safety”, 1st ed. New York: John Wiley and Sons, 2001.

- [21] Gunalan, S., Kolarkar, P.N. and Mahendran, M., “Experimental Study of Load Bearing Cold-formed Steel Wall Systems under Fire Conditions”, *Thin-Walled Structures*, 2013, Vol. 65, pp. 72–92.
- [22] Gunalan, S. and Mahendran, M., “Finite Element Modelling of Load Bearing Cold-formed Steel Wall Systems under Fire Conditions”, *Engineering Structures*, 2013, Vol. 56, pp. 1007-1027.
- [23] Paulik, F., Paulik, J. and Arnold, M., “Thermal Decomposition of Gypsum”, *Thermochimica Acta*, 1992, pp. 195-204.
- [24] Hopkin, D.J., Lennon, T., Rimawi, J.E. and Silberschmidt, V.V., “Numerical Study of Gypsum Plasterboard Behaviour under Standard and Natural Fire Conditions”, *Fire and Materials*, 2012, Vol. 36, No. 2, pp. 107-126.
- [25] Sergey, V. S., Wakili, K.G. and Hugi, E., “Investigation of Heat Transfer in Gypsum Plasterboard Exposed to Fire for Three Nominal Fire Scenarios”, *Journal of Fire Sciences*, 2012, Vol. 30, No. 3, pp. 240-255.
- [26] Ang, C.N. and Wang, Y.C., “Effect of Moisture Transfer on Specific Heat of Gypsum Plasterboard at High Temperatures”, *Construction and Building Materials*, 2009, Vol. 23, pp. 675-686.

**ORDER
FORM**

ISSN 1816-112X

**Advanced Steel Construction,
an international journal**Indexed by the Science Citation Index Expanded,
Materials Science Citation Index and ISI Alerting Services**From:****To:** Secretariat, Advanced Steel Construction, an international journal
Fax: (852) 2334-6389

I/ We would like to enter a subscription to the *International Journal of Advanced Steel Construction (IJASC)* published by The Hong Kong Institute of Steel Construction.

Please complete the form and send to:

International Journal of Advanced Steel Construction
c/o Department of Civil and Environmental Engineering
The Hong Kong Polytechnic University
Hungghom, Kowloon, Hong Kong

Fax: (852) 2334-6389 Email: ceslchan@polyu.edu.hk

Published by : The Hong Kong Institute of Steel Construction
Website: <http://www.hkisc.org/>

Please tick the appropriate box

- ☐ Please enter my hard-copy subscription (**4 issues per year**).
☐ Please send me a complimentary copy of the *Advanced Steel Construction, an International Journal (IJASC)*.

Please tick the appropriate box(es)

	<u>Print</u>	<u>On-line is free</u>
Personal	<input type="checkbox"/> US\$ 125	
Institutional	<input type="checkbox"/> US\$ 280	

Total Amount US\$ _____

Methods of payment ☐ Please invoice me
(please tick the appropriate box(es)) ☐ Cheque enclosed for US\$ _____ payable to
Hong Kong Institute of Steel Construction Limited
(No personal cheque accepted)

Ship to

Name (Prof./ Dr./ Mr./ Ms.) _____
Address _____

City/ State/ Postal Code _____
Country _____
Email _____ Fax _____